Engineering High Performance Electrodes for Energy Storage Devices from Low-cost, Sustainable and Naturally Abundant Biomaterials

by

Timothy Watson

B.Sc, The University of British Columbia, 2014

A THESIS SUBMITTED IN PARTIAL FULFILLMENT
OF THE REQUIREMENTS FOR THE DEGREE OF

Master of Applied Science

in

THE FACULTY OF GRADUATE AND POSTDOCTORAL STUDIES
(Biomedical Engineering)

The University of British Columbia
(Vancouver)

December 2016

Abstract

With the increased global push towards sustainable energy utilization, the need for advanced energy storage technologies has become increasingly important as countries seek to integrate rapidly advancing renewable energy technologies like wind and solar. At the same time, the burgeoning electric vehicle and wearable electronics industries are fuelling demand for lower-cost energy storage devices with high energy capacities and longer cycle lives. Currently, despite huge leaps in performance of Li-Ion batteries in recent years, the technology is approaching its predicted limits and new solutions will be needed to keep up with the demand of current and future electrical devices. At a time where scientific applications of nanomaterials and nanofabrication is on the rise, there exists an opportunity to take advantage of our increased understanding of nanotechnology to significantly improve existing energy storage devices and to unlock the potential of next-generation energy storage technologies.

In this work, binder-free and porous graphitic nanofibre electrodes produced from low-cost and sustainable softwood kraft lignin are devised and proposed as a platform for the development of high-performance energy storage devices. Motivated by difficulties facing some key energy storage technologies, scalable electrospinning of lignin and polyethylene oxide (PEO) precursor materials, followed by a hydrothermal treatment and carbonization in an inert atmosphere yields free-standing interconnected nanofibre electrodes with tunable porosity, high conductivity and superior electrochemical performance. Electrical impedance spectroscopy measurements of the optimized porous nanofibre electrodes demonstrate a conductivity reaching $18.39\,\mathrm{S\,cm^{-1}}$, while Brunauer-Emmett-Teller specific surface area measurements yield a specific surface area as high as $1258.41\,\mathrm{m^2\,g^{-1}}$. Supercapacitor devices revealed highly symmetric cyclic voltammetry results which demonstrated a gravimetric capacitance approaching $112\,\mathrm{F\,g^{-1}}$ at a voltage scan rate of $5\,\mathrm{mV\,s^{-1}}$. Galvanostatic charge/discharge experiments show reversible supercapacitor behaviour, a high capacity even at elevated voltage scan rates up to $200\,\mathrm{mV\,s^{-1}}$ and exhibit excellent cyclic stability, retaining 91% of their initial ca-

pacity after 6000 cycles. This work demonstrates the use of sustainable and abundant softwood Kraft lignin as source for porosity-tunable electrodes with high capacitance and stability as a demonstration of nature sourced and high performance electronic devices.

Preface

The author was responsible for all major areas of concept formation and experiment design with the assistance and guidance of Dr. Saeid Soltanian from the Flexible Electronics and Energy Lab at UBC.

Results in Chapter 4 and 5 are based on work conducted by the author in UBC's Advanced Fibrous Materials Lab under the supervision of Dr. Frank Ko and in UBC's flexible Energy and Electronics Lab under the supervision of Dr. Peyman Servati. X-Ray Diffraction measurements were performed by Anita Lam from UBC's department of Chemistry. Raman Spectroscopy measurements were performed by Jiaxin Ke from the Department of Materials Engineering at UBC. All of the data analysis along with all other data collection was performed by the author.

Portions of Chapter 4 and Chapter 5 are contained in a submission for publication written by the author and co-authored by Dr. Frank Ko, Dr. Peyman Servati and Dr. Saeid Soltanian. The submission is currently under review.

Table of Contents

List of Tables

List of Figures

Acknowledgments

I want to express my gratitude to Dr. Frank Ko and to Dr. Peyman Servati for their continued support and mentorship throughout the completion of this work. I also would like to thank Dr. Saeid Soltanian for all of the advice and guidance that he provided me during this project, for his patience and willingness to answer my questions and for the work he did to ensure that all of the necessary materials and equipment needed for this work were available. This project would not have been possible without his support and the support of all of the students and staff in both the Advanced Fibrous Materials Lab and the Flexible Electronics Engineering Lab.

I would also like to thank Lynn Wan for her expertise surrounding lignin and electrospinning, Anita Lam for her help with XRD testing, Jiaxin Ke for his help performing Raman spectroscopy, Sally Finora for her expertise regarding BET testing, Mijung Cho for assisting me with TGA and Yuta Dobashi for his advice regarding supercapacitor testing.

Portions of this work were made possible through funding from a Strategic Research Grant from the Natural Sciences and Engineering Research Council of Canada along with funding from the Canada Foundation for Innovation.

Chapter 1

Introduction

Over the past decades, the importance of efficient electrical energy storage has grown exponentially following an explosion of devices that rely on electrical power and a significant push towards sustainable energy practices. As of 2012, the global production of electricity reached about 22,200 TWh annually, 70% of which was generated through the burning of fossil fuels including coal, oil and natural gas [1]. Today, international targets for reducing fossil fuel related emissions have motivated a push towards sustainable energy usage in both the public and private sectors. Problematically, renewable energy sources like wind and solar can be unreliable, a problem that has proven to be a great challenge for sustainable energy generation, reliability and power network efficiency and stability. Efficient, cheap and reliable energy storage has long been proposed as a solution to the problems of renewable power reliability and great efforts are currently underway to develop better energy storage devices to allow for continued progress towards the adoption of sustainable energy practices. At the same time, adoption of personal communication devices like cell phones, tablets and computers on a massive scale as well as the advent of wearable electronics continues to fuel demand for higher performing energy storage devices.

Recently, the conversation around energy storage has grown in volume follow-

ing the success of companies like Tesla and Solarcity that are seeking to change the way that society interacts with and makes choices about their energy consumption. For one, Tesla's electric vehicles have convinced many that electric vehicles (EVs), once thought to be far inferior to hydrocarbon fueled vehicles as a mode of transport, can indeed perform at least as well as, and in some cases better than traditional vehicles without many of the negative side-effects. This realization has seen almost all of the big car companies invest heavily in EV research and development and has contributed greatly to advances in electrical energy storage technologies. The transportation industry is expected to continue to contribute to the demand for electrical energy storage in a massive way in the upcoming decades. Electric vehicles are predicted to make up 35% of all new vehicle sales and consume 2,700 TWh of electricity by 2040, a figure that is equivalent to 11% of todays global energy use [2].

As well as being driven by the global sustainability movement, the success of EVs recently has been fueled by dramatic advances in energy storage technologies. The Li-Ion battery for example, which is the energy storage technology that underpins the majority of EVs has been the subject of rapid technological advance over the past decades and is currently experiencing a dramatic fall in the price per kWh of power, from over $1,200 per kWh in 2010 to under $400 per kWh in 2015 [3]. This fall in cost is further contributing to the demand for energy storage as lower costs facilitate the development of energy storage reliant industries like the EV industry. Despite the apparent success in recent times of the EV industry, EV technology has immense room for improvement. Many EVs today still have woefully low range with even the best EVs requiring recharging after only 300 or so miles [4]. The current industry target of 500 miles of range on a single charge

requires further development of advanced and drastically improved energy storage technologies with higher energy storage capacities, increased safety characteristics, lower cost and weight and using more sustainable materials.

Simultaneously and also on the energy front, the cost of production for renewable energy like solar and wind is falling dramatically as technological advancements appear in these sectors as well. As a result, the demand for PV cells has been increasing dramatically as the price per watt has fallen over recent years. Similar advancements are changing the economics and demand for wind power and demand is expected to continue increasing at dramatic rates for the foreseeable future. In the renewable energy sector, it is estimated that wind and solar power will add 8.6 TW of new power generating capacity worldwide in the next 25 years [2]. The success of wind and solar depends on the ability to store the electrical power produced so that it can distributed and used efficiently and the market for these technologies is expected to rise from 31.88 million in 2015 to 2.9 billion in 2024 [5]. Similarly to EV technology, the success of energy storage in the renewable energy industry depends on increasing storage capacities and lowering the cost and environmental impact of energy storage technologies.

A third driver of energy storage technologies, and perhaps one of the biggest drivers of demand for electrical energy storage today is the portable electronic devices industry. Without taking into account tablets, laptops and other portable electronic devices, the number of smartphones alone in circulation is expected to rise to 6.1 billion by 2020, further increasing the demand and importance of efficient electrical energy storage [6]. With 5 billion people expected to gain access to the internet between now and 2020, the demand for portable devices has never been greater [7]. Additionally, recent technological advances have opened the door for

an entirely new industry that will further contribute towards the demand for high performance energy storage devices: wearable electronics. This industry, much like the portable electronics industry, is demanding smaller batteries with high energy density and lower cost and weight and is expected to grow to a market size of over $35 billion USD in the next two years [8].

Outside of the renewable energy industry, the transportation industry, and the portable electronics industry, energy storage remains a crucial component of many of the world's other industries including manufacturing and telecommunications. In high tech manufacturing for example, some $80 billion USD is lost by American industry each year due to electrical power outages and interruptions due to unreliable power storage and transmission [9]. The progression of these industries, in conjunction with the key industries described above, is fuelling the demand for energy storage technologies with higher storage capacities, efficiencies and cycle lives like never before. The explosion of electrical devices has seen off grid electrical use expand from a niche market in the early 20th century to a booming present day industry. While there exists today a plethora of methods for storing energy, from low cost hydro storage systems to specialized fuel cells, two electrical energy storage devices dominate the portable electronics, transportation, manufacturing and renewable energy industries and will be the focus of this work: batteries and capacitors. Batteries and capacitors have significantly different attributes and applications but are similar in the way that they store energy electrochemically and can be scaled up or down for a wide range of applications. Both of these technologies are the subject of rapid technological advance and are slated to change the way that modern society uses electrical energy on a daily basis.

One factor that is facilitating the advance of these key energy storage technolo-

gies is the massive progress that has been seen in the field of nanomaterials over the past decade. When combined with advances in materials engineering and nanofabrication techniques, well engineered nanomaterials have the potential to contribute to the advancement of energy storage devices in a number of key ways including 1) improving energy storage capacity of devices, 2) enhancing cycle life and stability, 3) increasing charge and discharge rates and 4) improving safety characteristics. By carefully selecting precursor materials, significant improvements in sustainability and cost can also be achieved. The progression of nanomaterials engineering has allowed for significant improvements in existing energy storage technologies, such as the ubiquitous Li-Ion battery and may be the key to unlocking next-generation energy storage technologies that have, up to this point, remained commercially non-viable.

With the goals of high capacity, low cost and weight, stability and sustainability in mind, this study explores advances in nanomaterial engineering as it relates to energy storage device development and details the development of novel and sustainable electrodes for high-performance electrical energy storage devices. The proposed electrodes are developed from naturally abundant and sustainable biomaterials and take advantage of advanced nanofabrication techniques to create a highly-engineered 3D framework for electrodes in energy storage devices. The work is motivated by existing difficulties facing some of todays most promising next generation energy storage devices including the Lithium-Sulfur battery. The solutions presented in this work, while applicable to Lithium-Sulfur batteries, are more widely applicable to energy storage devices in general and are characterized by fabricating and testing supercapacitor devices.

Chapter 2

Objectives

As the market for energy storage devices continues to grow under the pressure of increasing demand from the renewable energy, electric vehicle, manufacturing and consumer electronics industries, technological breakthroughs will be required to keep up with industry targets. Today's Li-Ion technologies have improved so much in recent years that the performance of this technology is approaching its theoretical maximum (Fig 2.1). With benchmarks for energy device performance already set by governments and industry alike, research and development efforts have turned to the fields of nanomaterials and nanofabrication to look for ways of improving device performance and unlocking next generation storage technologies. Following an increasing world wide focus on sustainability, the issues of sustainable materials and fabrication techniques have become equally important to performance when designing the next generation of devices. In this work, advances in nanofabrication techniques are applied to development of high performance electrodes from sustainable materials for use in next generation energy storage technologies.

While incremental improvements to energy storage technologies continue to be a regular occurrence in academia, scaling up breakthroughs from the lab setting to the commercial setting requires more than just improvements in key performance

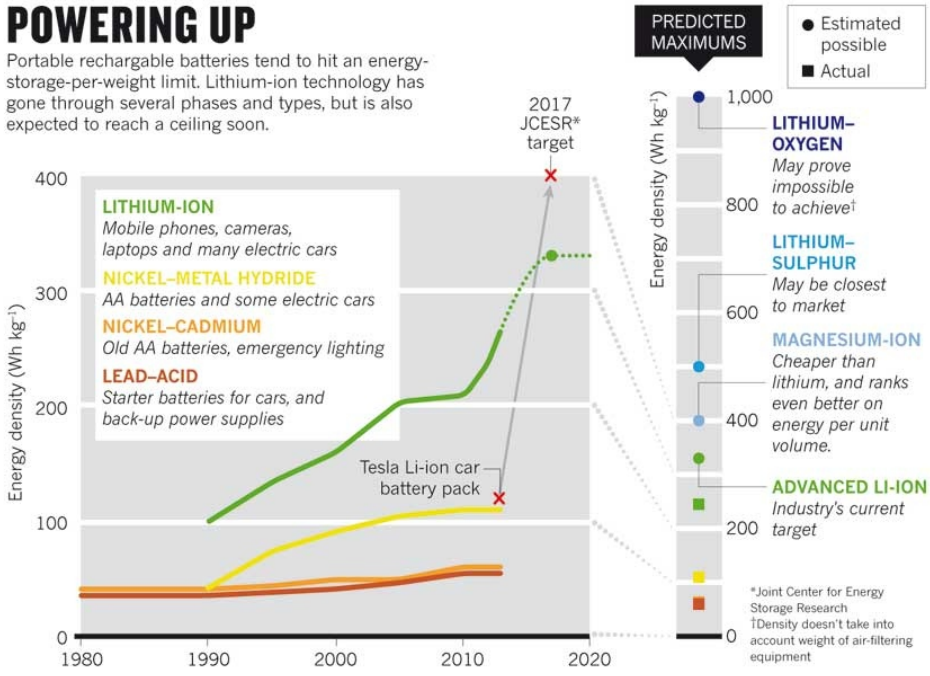

Figure 2.1: Schematic showing the current and expected energy densities for various battery technologies (reproduced with permission from [10]).

metrics. The commercial success of energy storage technologies depends on a number of factors. In addition to having exemplary electrochemical performance characteristics, next generation energy storage devices require excellent structural and physical properties, including low weight and high mechanical resilience and felexibility and should use primarily sustainable component materials. Also, cost of materials should be low and fabrication techniques should be inexpensive, relatively simple and should be highly scalable to allow for mass production. With these considerations in mind, this work will attempt to look at energy storage devices with their commercial feasibility in mind, which will propose carefully thought-out and holistic designs and materials for next generation storage devices.

Of the avenues through which the development of energy storage devices is progressing, electrode research and development is perhaps the most ready for the arrival of modern nanomaterial and nanofabrication science. Due to the complex nanoscale processes involved in storage device operation, the application of nanomaterials and nanofabrication to electrodes presents an opportunity to control and to optimize these processes like never before. With the push towards better storage technology arriving in tandem with increased understanding of nanoengineering techniques, there is an opportunity to use nanofabrication practices to push energy storage into the future by designing and fabricating intelligently engineered electrodes. With this in mind, the primary objective of this work is to develop a platform from which high performance electrodes for applications in commercial next generation energy storage devices can be based.

In order to achieve the objectives of this work, naturally abundant and sustainable biomaterials will be used to engineer intelligently designed electrodes with a specific goal of alleviating some of the concerns facing next generation battery technologies. Highly scalable fabrication techniques including electrospinning will be studied with an eye on the future commercial feasibility of the proposed devices and low cost precursor materials will be used whenever possible. A thorough study of performance considerations for energy storage devices electrodes will be conducted and the proposed electrodes will seek to meet and exceed the performance parameters of commonly used carbon based materials through intelligent nanoscale design. The proposed electrodes will be presented as a platform on which to base the development of future and even higher performing electrodes for next generation devices.

Chapter 3

Literature Review and Background

3.1 Batteries

The most ubiquitous and probably the more familiar of the two major electrochemical energy storage technologies is the battery. According to The Freedonia Group, the global market for batteries is expected to reach $120 USD billion by 2019, up from $83 billion in 2015 [11]. While today, many of us rely on batteries to power essential technologies on a daily basis, the history of the battery began in earnest in the 17th and 18th centuries. Despite evidence of early electrochemical cells as long ago as 2,000 years ago, the first semblance of a battery as we recognize it today appeared in 1800 with the invention of Alessandro Volta's "Voltaic Column". Earlier, Volta had discovered that specific liquids have the ability to initiate chemical reactions between dissimilar metals and instigate the flow of electrical current. By alternatingly stacking plates of copper and zinc and separating these plates with a thin sheet of cloth saturated in acid, Volta was able to generate sizeable electric current in a wire connected to the ends of the stack [12]. The result was a rudimentary battery, the first of its kind.

The Voltaic Column functioned by converting chemical energy into electrical energy through a series of electrochemical reactions. As with all other batteries

that would come after, during discharge, the electrolyte, in this case a strong acid, reacts with the metal anode and through oxidation, releases ions, which will then migrate across the cell. The free electrons, which are liberated from the anode can then travel through a wire to the cathode, where the electrons re-combine with the ions in the electrolyte in a reductive reaction. An electrical device can be powered by this flow of electrons. A thin separator, pieces of cloth or cardboard in the case of the Voltaic Column, is usually added to prevent contact of the two electrodes and electrical shorting of the cell. A simple schematic of a battery is provided in Fig 3.1.

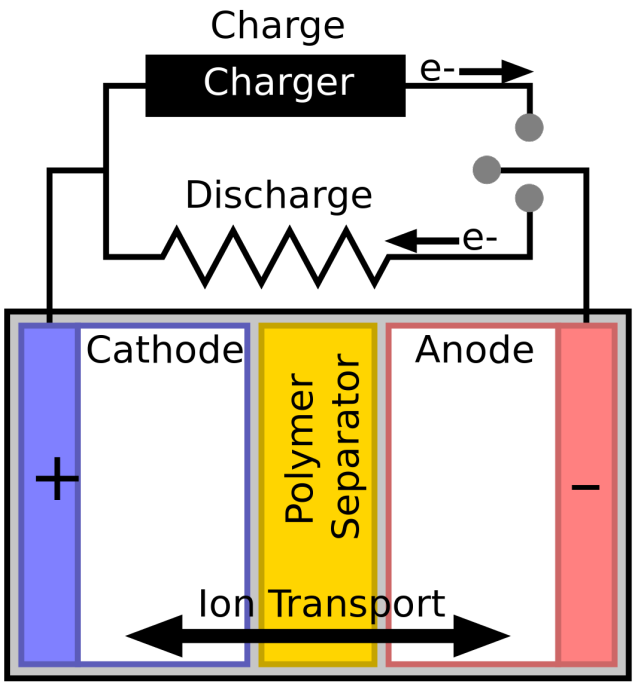

Figure 3.1: Schematic of a simple battery (reproduced with permission from [13]).

Volta's battery spurred a huge amount of technological innovation at the time

and lead, among other things, to the invention of electrolysis and to the discovery of the ability to isolate chemical elements. In 1802, William Cruickshank developed the first battery suitable for mass production which consisted of a voltaic column laid sideways and encased in concrete [12]. In 1836, a British chemist named John Daniell invented a new variant of the battery, known as the "Daniell Cell", which relied on a zinc electrode submersed in sulfuric acid and then placed in an earthenware pot which was then submerged in a copper pot filled with sulfuric acid. The resultant cell provided a longer and more reliable current while also being safer than the Voltaic Column. It soon became the standard battery in industries such as telecommunication [12].

Over the next decades, battery technology progressed rapidly and higher performing batteries where introduced to the market regularly. Up until 1859 however, all batteries where primary batteries, meaning that they could not be recharged and were usually disposed of after running out of usable charge. In 1859, a french physicist named Gaston Planté invented the first ever rechargeable battery that could be charged by passing current through the cell in the reverse direction. His lead-acid battery was made using a lead anode and a lead dioxide cathode with sulfuric acid as the electrolyte. During discharge, the electrolyte reacts with the lead anode and releases electrons. At the same time, electrons are absorbed by the lead dioxide cathode as it too reacts with the sulfuric acid. This produces a current, which, if reversed, causes the chemical reactions in the cell to proceed in the opposite direction [14]. Despite its size and bulk, Planté's lead-acid battery became very popular in applications requiring large currents and is still in use today in industries like the automobile industry.

In 1866, Georges Leclanché developed a battery relying on a zinc anode and a

manganese dioxide cathode dipped into a jar of ammonium chloride. At the time, the 1.4 volts that this cell could provide made it useful in applications from telegraphy to signalling [14]. Despite its commercial success, the Leclanché cell and those before it suffered from a major drawback: they relied on a liquid electrolyte which made the cells heavy, bulky and non-portable. In 1886, Carl Gassner invented the first dry cell that did not require the use of a liquid electrolyte. Instead, Gassner's cell used plaster of Paris, mixed with ammonium chloride as a solid electrolyte. This, combined with a manganese dioxide cathode and a zinc anode made a portable and maintenance free battery capable of a 1.5 volts output [14]. The convenience of this design allowed the battery to flourish and the Gassner cell became the first truly ubiquitous battery, allowing for the proliferation of portable electronic devices, such as the flashlight. In 1899, the first alkaline battery appeared after a Swede named Weldemar Jungner combined nickel and cadmium electrodes with a potassium hydroxide solution [14]. Nickel-cadmium batteries (Ni-Cd) had significantly better energy density compared to lead-acid batteries.

By 1903, Thomas Edison had patented the nickel-iron battery in hopes of commercializing a more light weight and durable alternative to lead-acid batteries for electric vehicles. Despite never catching on in the personal transportation industry, the design became very popular in other industries like the rail and mining industries. Until the 1950s, Gassner's zinc-carbon battery remained popular, despite its low battery life. In 1959, a researcher named Lewis Urry developed a longer lasting alkaline battery from manganese dioxide and powdered zinc. The new battery's longer life quickly made it popular with consumers. In 1989, nickel-metal hydride (Ni-MH) batteries appeared which promised even longer lifespans for smaller applications [14]. These batteries used a nickel oxide hydroxide cath-

ode like in Ni-Cd batteries but employed a hydrogen absorbing alloy as the anode. Ni-MH cells can have 3 times the capacity of an equivalent Ni-Cd cell and by 2006 had all but replaced Ni-Cd cells [15].

Meanwhile, much research was being done on an even more promising battery technology based on lithium batteries which had hit the market in 1970. Lithium had been identified in 1912 as being suitable for batteries due to its low density, and high electrochemical potential and energy-to-weight ratio. In 1985, a Japanese research team at Asahi Chemical built the first lithium-ion battery prototype, improving on the existing primary lithium battery technology by increasing stability and adding rechargeability [16]. In 1991, the first rechargeable lithium-ion battery was commercialized by Sony and utilized a lithium cobalt oxide cathode [17].

The introduction of the lithium-ion (Li-ion) battery revolutionized the rechargeable battery market with its portability, high energy density, low self-discharge rate and small memory effect. In a Li-ion cell, lithium ions travel travel back and forth between the positive and negative electrodes during charging and discharging. Typically, these cells employ an intercalated lithium compound as the anode, usually graphite, and a lithium oxide cathode. During charging, positively charged lithium ions flow from the cathode and intercalate into the graphite anode. Unlike some other battery types, this intercalation mechanism does not involve a chemical reaction. During discharge, the opposite process occurs and lithium ions are released from the anode and can travel freely back to the cathode. Over the ensuing years, Li-Ion battery technology saw continuous improvements as researchers developed and discovered new electrode and electrolyte materials, some of which are detailed in the following paragraphs.

LCO Batteries: Since Sony's introduction of their lithium cobalt oxide (LCO) lithium-ion battery in 1991, the popularity of this system has exploded and the LCO battery has quickly become the most popular battery for consumer and portable electronics. LCO batteries utilize a Cobalt-Oxide cathode and a graphitic carbon anode. Compared to nickel-based alkaline batteries, LCO cells are smaller, have a higher energy density, and can operate over a wider range of temperatures. Additionally LCO batteries lose a fraction of the charge per month compared to nickel-based cells: 5-10% compared to more than 30% [18]. LCO batteries do come with a downside however. More expensive to make than nickel-batteries, LCO cells are susceptible to thermal runaway if over charged and so require the addition of protective circuitry. This circuitry can accelerate self-discharge and limit discharge rate. Additionally, LCO cells accumulate internal resistance as they cycle and so have limited lifetimes.

LFP and LMO Batteries: In 1996, the group of John Goodenough at the University of Texas invented a new variation of the Li-ion battery relying on lithium iron phosphate (LFP) as the cathode. This material is much cheaper than lithium cobalt oxide as well as being inherently more stable. LFP batteries have a lower energy density than LCO cells but have longer cycle lives, a higher discharge rate and make for a battery that is 14% cheaper than an equivalent LCO cell [18]. A third popular Li-ion cell type is the lithium manganese oxide (LMO) cell which was also developed in 1996. This variation has very high thermal stability and low internal resistance, making it ideal for applications requiring fast recharging and high currents - they can output 20-30 amps safely. Problematically however, these cells have very low energy density and are only able to hold 1200 mAh of power in

a typical 18650 cell, about half of the capacity of LCO cells [18].

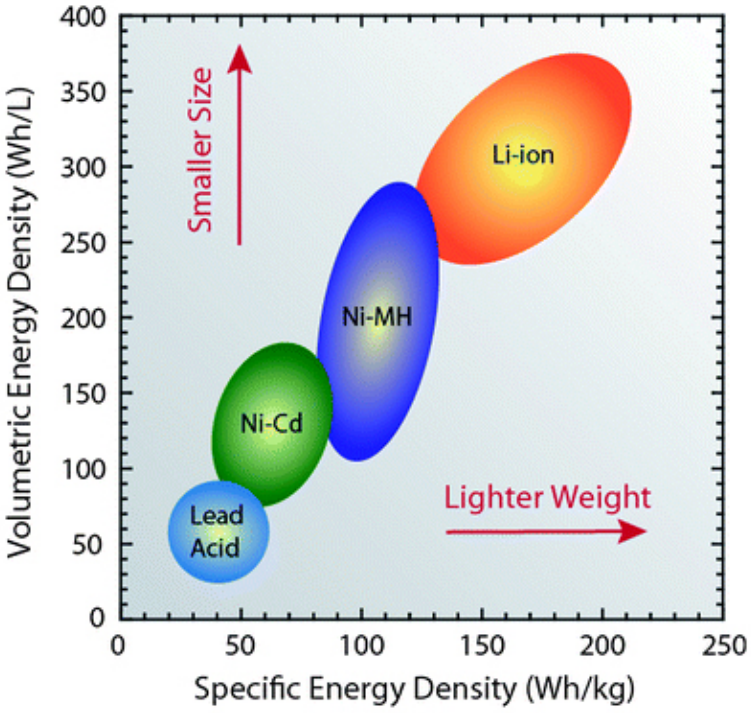

Figure 3.2: Specific and volumetric energy density of some of the established secondary battery types (reproduced with permission from [19]).

Li-Ion batteries drastically improved performance of many of the portable devices that we are familiar with today and represented a huge step forwards in the development of battery technology. Fig 3.2 presents a summary of the performances of some of the major secondary battery types developed in the last century. Despite the radical change brought about by the Li-ion battery, the technology is starting to approach its theoretical limits and the need for improvements in battery technology has become apparent (see Fig 2.1). The incredible progress of portable electronics, the rise in the use of electric vehicles and the advance of renewable energy technologies are all demanding increases in energy storage performance and

capabilities beyond what is commercially available today. In November 2013, the U.S. department of energy announced a $120M effort to develop next generation battery technology with a goal of extending battery life by 5 times that of 2012 batteries [20]. This effort, others like it, and pressure from key industries has lead to intensive research on next generation battery technologies, a few of which are highlighted in the following paragraphs.

Lithium-Silicon Cells: Lithium-Silicon cells employ a silicon anode which can, in theory, hold more than ten times the number of lithium ions than typical graphite anodes, leading to an extraordinarily high theoretical specific capacity of 4200 mAh/g compared to 372 mAh/g for graphite. This is because silicon atoms can bind up to 4.4 lithium ions compared with one ion per 6 carbon atoms in graphite. Problematically however, silicon anodes have been found to expand to over 3 times their original volume during anode lithiation. This expansion can lead to cracks and crumbling in the anode as well as detachment from the current collector. Research stage cells have been shown to lose almost all of their capacity in as few as 10 cycles. Additionally, lithium-silicon cells are plagued by the formation of a solid electrolyte interface layer (SEI), which, due to cracking caused by volume expansion, can continue to grow and eventually leads to very high internal cell resistance and low efficiency. Despite these drawbacks however, efforts to optimize lithium-silicon cell performance continue.

Lithium-Air Cells: Lithium-Air batteries are another highly promising next generation battery technology. In lithium air batteries, oxygen reacts with lithium ions dissolved in the electrolyte at the cathode to form lithium peroxide. In the reverse

reaction, lithium peroxide disassociates to produce lithium ions and oxygen. This system is a precipitation-dissolution system and is very unlike the intercalation reaction that typical Li-ion batteries rely on. The major advantage of the lithium-air battery is that, because oxygen is found abundantly in air, it does not have to be stored on board the battery and instead, can be supplied to the battery by flowing air into the cell. This means that theoretically, cells can achieve an energy density of 11,140 $\mathrm{Wh\,kg^{-1}}$ [21]. There are significant challenges associated with this battery design however. Moisture and contamination has to be filtered out of the air in order to prevent impurities from entering the cell and degrading battery performance. Even more problematically, the precipitation-dissolution can be slow and so lithium-air batteries are known to have low discharge and charge rates. Additionally, there is a mismatch in the charge vs. discharge voltages in these cells meaning that lithium-air batteries can be very inefficient.

Lithium-sulfur Cells: Lithium-sulfur (Li-S) batteries have been the subject of increasing research recently and are thought to be the next generation battery technology that is closest to commercialization. This increase in activity has been fuelled by the progression of the electric vehicle industry, an industry that is demanding the progress of battery technology to allow for electric vehicles with ranges of around 500 miles+ per charge. This type of range requires a battery with a cell level specific energy of 350-400 $\mathrm{Wh\,kg^{-1}}$ [22], a figure that is significantly higher than the 200 $\mathrm{Wh\,kg^{-1}}$ that current Li-ion cells can provide. In order to meet the energy density target of 400 $\mathrm{Wh\,kg^{-1}}$ by 2017, a target set officially by the US Department of Energy [10], new battery technologies must be explored and Li-S batteries are a prime candidate for meeting such a target because of their high theoretical ca-

pacities and other highly desirable characteristics. As indicated in Table 3.1, Li-S batteries have a high theoretical specific energy of 2,567 $\mathrm{Wh\,kg^{-1}}$, almost 5 times that of Li-Ion cells. In practice, the predicted possible energy density is likely to be closer to 500 $\mathrm{Wh\,kg^{-1}}$. Additionally, the active ingredient in Li-S cells is sulfur, a naturally abundant, widely available and low cost material, making Li-S cells relatively cheap to produce and more environmentally sustainable than other battery chemistries. The combination of high energy density, low-cost and sustainability of component materials makes Li-S cells worth exploring further.

Battery	**Cell Voltage (V)**	**Theoretical Specific Energy ($\mathbf{Wh\,kg^{-1}}$)**
Li-ion	3.8	387
Li-S	2.2	2,567
Li-Air (non-aqueous)	3.0	3,505
Li-Air (aqueous)	3.2	3,582

Table 3.1: Voltage and theoretical specific energy of lithium based energy-storage devices (adapted from ref [10].)

Li-S batteries are commonly constructed using a lithium metal anode and a sulfur cathode. During discharge, lithium metal is oxidized, freeing up lithium ions and electrons at the anode. The lithium ions then travel through the electrolyte and reacts chemically with sulfur and with the free electrons, which have by then passed through the external circuit. The reaction is a reduction reaction and produces either lithium sulfide (Li_2S) or lithium disulfide (Li_2S_2). The overall reaction is as follows:

$$\mathrm{Li} \longrightarrow \mathrm{Li^+} + \mathrm{e^-}$$

$$\mathrm{S_8} + 16\,\mathrm{Li^+} + 16\,\mathrm{e^-} \longrightarrow 8\,\mathrm{Li_2S}$$

$$16\,\mathrm{Li} + \mathrm{S_8} \longrightarrow 8\,\mathrm{Li_2S}$$

Li-S cathodes usually contain sulfur in its most stable form, S_8. As previously mentioned, during charge, lithium ions interact with stable sulfur to form one of two solid products in the cathode: Li_2S_2 and Li_2S [23]. This reaction is far from simple however and is still being fully understood. One of the challenges of Li-S batteries arises from this reaction and is known as the polysulfide shuttling effect which arises because, when S_8 is reduced by lithium ions, it goes through a series of reduction reactions before it reaches its final solid form. In between, it passes through various polysulfide forms, beginning with long chain polysulfides, Li_2S_8 and Li_2S_6, before passing through shorter chain forms like Li_2S_4, Li_2S_2 and Li_2S [24]. Problematically, some of these polysulfides are highly soluble in typical organic electrolytes, meaning that they can dissolve into the electrolyte and migrate around the cell. It has been found that higher order polysulfides tend to migrate to the anode, where they are reduced to lower order polysulfides that migrate back to the cathode before being oxidized to high order polysulfides again. This process is referred to as the polysulfide shuttling effect.

The shuttling effect, shown schematically in Fig 3.3, can repeat itself endlessly and can lead to loss of active material in the cell, dramatically decreasing efficiency and cycle life [24]. Additionally, dissolved polysulfides have a tendency to plate themselves onto the surface of the anode, forming insoluble products in the process. This too can significantly hinder the free flow of ions to and from the anode and drastically and negatively impact the performance of the battery [25]. Finally, the insulating nature of sulfur poses an additional problem for Li-S cells. Because electrons can not flow freely from reaction sites within the cathode, Li-S cathodes need to incorporate conductive additives so that the flow of electrical current can be established. this can have a negative impact on the overall specific capacity and

volumetric capacity of Li-S cells.

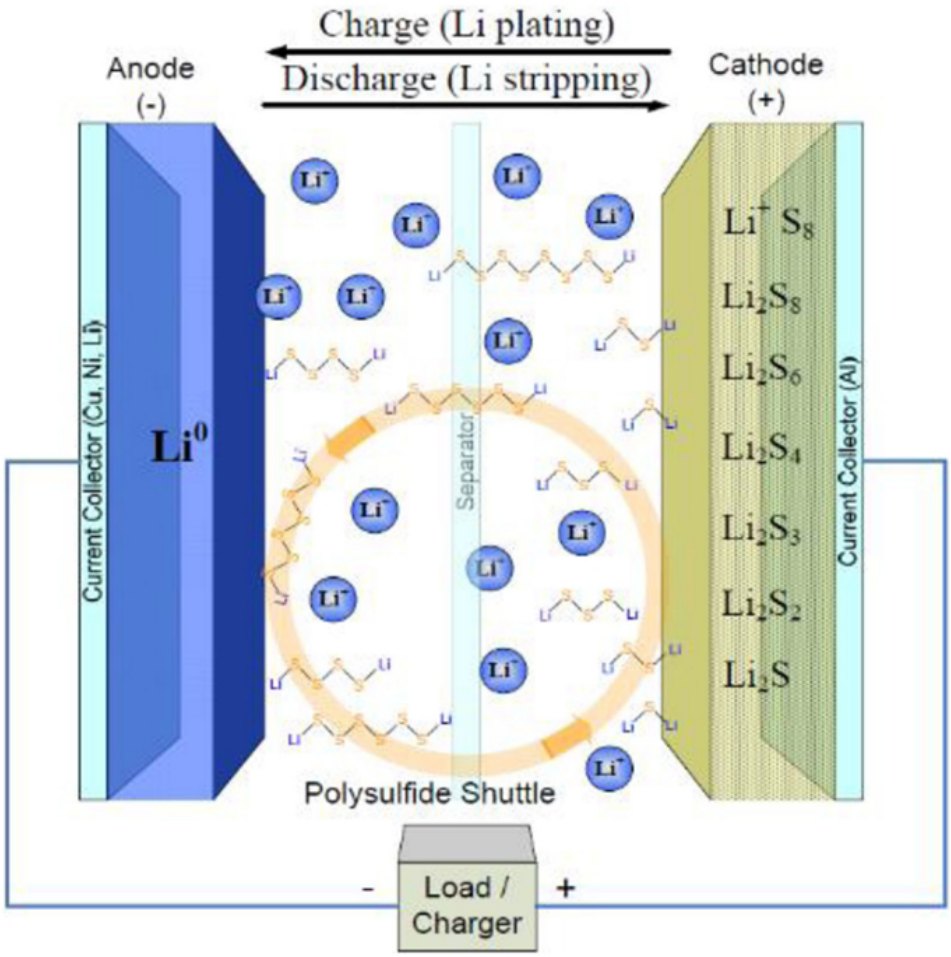

Figure 3.3: Schematic of the polysulfide shuttling effect in Li-S batteries (reproduced with permission from [26]).

In order to combat these limitations, groups around the world have adopted a wide variety of approaches. One popular avenue of research is to develop new electrolyte chemistries with the goal of decreasing polysulfide solubility within the electrolyte. This approach has lead to experimentation with non-aqueous, ionic, solid polymer and glass-ceramic electrolytes among others [27]. Other groups are

focusing on novel separator designs to help limit the flow of polysulfides and have even begun introducing what is known as an "interlayer" [28]. This additional conductive layer between the sulfur cathode and the separator is designed to help block the diffusion of polysulfides and increase the electrical contact to the sulfur cathode. While this strategy can provide benefits in terms of cycle life, it can drastically decrease the specific and volumetric capacities of the cell. Still other groups are looking at ways of altering the chemistries at the electrodes to improve performance and safety. For example, there is much research into the idea of using a Li_2S based cathode instead of one relying on elemental sulfur [29]. This strategy allows for the use of non-lithium anodes which may be safer than conventional lithium-based anodes. Finally, and perhaps one of the more popular research directions is the search for new and novel cathode materials and structural designs that might help Li-S cells circumnavigate some of the problems that they currently face.

Within the battery market, we are starting to see the appearance of commercial Li-S batteries with Oxis Energy appearing to lead the way. The UK company recently announced a Li-S cell that they claim achieves over $400\,\mathrm{Wh\,kg^{-1}}$. Even within the context of this apparent success, cyclability problems caused by the shuttle effect continue to plague even the best experimental Li-S cells. There remains much improvement to be done in the field before Li-S batteries can achieve commercial success on a wider scale and further investigation and experimentation on electrode materials and geometries is necessary. Despite these difficulties, the sentiment within the research community is that, with the progression of advanced nanofabrication techniques and an ever increasing understanding of materials used in battery research coupled with drastically increased interest in the field of rechargeable batteries, we may be getting closer to solving the problems asso-

ciated with the technology. For these reasons, the development of new materials and intelligently engineered cathode structures is hugely exciting. Fig 3.4 presents a summary of the characteristics and development trajectory of recent battery technologies.

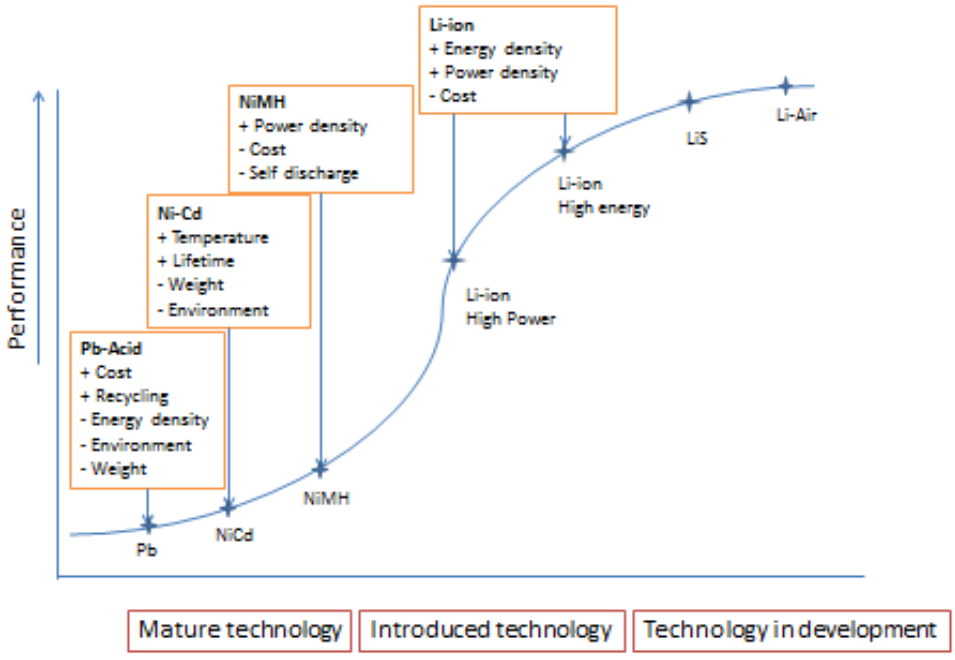

Figure 3.4: Battery technology roadmap and characteristics (reproduced with permission from [30]).

3.2 Supercapacitors

Like batteries, research on supercapacitors has seen huge growth over the last decade as teams continue to push for better ways of storing and using electrical energy. Indeed, there are many parallels between high performance supercapacitors and batteries, and in particular, in the design of the electrodes for both systems. Electrochemical capacitors (EC), otherwise known as supercapacitors or ul-

tracapacitors, have been the subject of rapid technological advancement since their appearance in 1957 in the labs of General Electric (GE). In 1962 and improving on GE's experimental designs, the Standard Oil Company of Ohio (SOHIO) developed the first supercapacitor in the format that we are familiar with today. SOHIO had high hopes for the newly developed technology and sought to develop it for applications in power rectification. By 1971, these efforts had failed and the company had accumulated too much debt from building the Alaska Pipeline to continue with development of their supercapacitors. In 1975, SOHIO licensed their EC technology to the Nippon Electric Company (NEC) of Japan, who, in 1978, began the first commercial production of their NEC SuperCapacitor, which was marketed as a back-up device for clock chips and computer memories [31]. Since then, supercapacitors have progressed rapidly through many generations of designs and have found applications in a huge variety of industries, from wireless communication to transportation.

The best of the early commercial devices had voltage ratings of a few volts and low capacitance values ranging from fractions of farads up to a few farads. In contrast, today's supercapacitors can achieve performance ratings of hundreds of thousands of farads and operate at voltages of thousands of volts, demonstrating the level of progress that the field has seen over the past 40 years [31]. Shortly after the release of the first commercial supercapacitor, Panasonic entered the market with its "Goldcaps" brand, followed shortly by ELNA's "Dynacap" supercapacitors [32]. Because of the high internal resistance in these early supercapacitors, they were limited to low current applications like powering computer chips and backing up data. In 1982, the Pinnacle Research Institute (PRI) introduced its ultracapacitor, the first such double-layer capacitor capable of being used in high power ap-

plications. Designed for military applications, the PRI ultracapacitor incorporated electrodes made from metal-oxide and its release triggered renewed interest in the technology by the US Department of Energy. This lead to the formation of the Ultracapacitor Development Program at Maxwell Laboratories in 1992 [33].

Supercapacitors are double-layer capacitors with low voltage limits and with high capacitance values. In a supercapacitor, two electrodes are immersed in an electrolyte containing both positive and negative ions. Upon application of a voltage across the two electrodes, the positive and negative ions migrate across the electrolyte in different directions and gather at the surface of the electrodes, creating an electric double layer at each of the electrodes as shown in Fig 3.5. Supercapacitors can be classified as either electrical double-layer capacitors (EDLCs), which rely purely of the accumulation of electrostatic charge at the electrode/electrolyte interface, or as pseudocapacitors, which produce electricity via fast and reversible redox reactions at active sites on the electrode [34]. In practice, many supercapacitors display characteristics of both types.

Supercapacitors have numerous applications and have a variety of advantages compared to other energy storage devices. For one, supercapacitors have very long cycle lives, often operating for 10 to 20 years without losing significant amounts of capacity. Additionally, supercapacitors can function well in extreme environments and are able to provide energy at temperatures reaching -40°C. The primary advantage to using supercapacitors however is their ability to provide high load currents meaning they can charge in mere seconds. Supercapacitors have very high power density when compared to batteries. On the other hand, supercapacitors have relatively low energy density and so can not provide power continuously for long periods of time. A typical supercapacitor has a cell voltage of around 2.7 V and

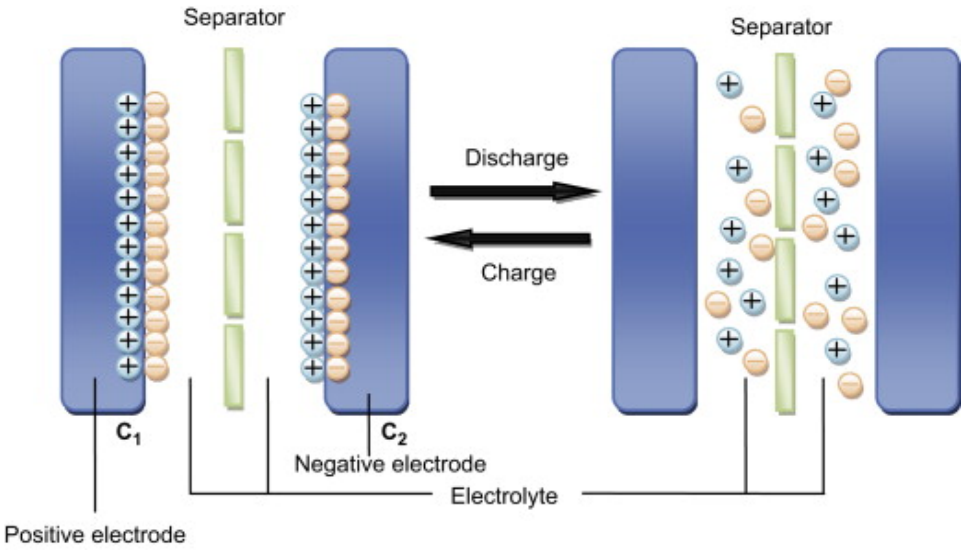

Figure 3.5: Schematic of a supercapacitor during charge and during discharge (reproduced with permission from [35]).

can easily be connected in series to boost voltage. Supercapacitors are in use today in a huge variety of industries, from consumer electronics to medical devices and and the market for supercapacitors is expected to grow quickly in the next decade.

Since the conception of the Ultracapacitor Development Program, there has been vast improvements in supercapacitor performance in all performance metrics. While there has been some work in the research community focused on improving the break-down characteristics of electrolytes in order to raise the operating voltage of supercapacitors, the lion's share of efforts have been dedicated to improving materials and material properties of supercapacitor electrodes. The energy storage capability of a supercapacitor is referred to as *capacitance* (C) and is often measured in Farads per gram. Capacitance is a function of the surface area (A), the permittivity (ε) and the distance between plates of the cell (d) (Eqn3.1).

$$C = \varepsilon * (A/d) \tag{3.1}$$

Following along with this relationship, high performance supercapacitors usually include electrodes with very high specific surfaces areas which helps to increase the amount of charge that a cell can hold. High surface area is often achieved through developing highly porous electrode materials. Additionally, supercapacitor performance can be linked to the electrical conductivity of the electrodes, meaning that highly conductive materials are preferable for high performance supercapacitors. For these reason, modern supercapacitors are generally constructed using activated carbons and other carbon derivatives like carbon-fibre cloth and carbon aerogels. By far the most widespread source of carbon for commercial supercapacitors today is activated carbon, which is usually derived from coconut husk.

The materials currently being used for supercapacitors have high surface area but continue to suffer from low mesoporosity, meaning that electrolyte accessibility is still weak within the electrode. This can lead to low energy density in the device, which, when considered in parallel with the poor electrical conductivity of many carbon materials and therefore high internal resistance, means today's supercapacitors continue to deliver much lower power density then theoretically possible. Additionally, typical supercapacitor electrodes require the addition of binding agents and conductive agents as well. A typical commercial supercapacitor is made up of around 85% activated carbon, 10% conductive additive (carbon black for example) and 5% binding agent (PTFE for example) [36]. The addition of these agents further decreased volumetric power and energy density while contributing to increased electrode weight and cost. Currently available supercapacitors based

on activated carbons can provided power densities in the range of 1-2 $\mathrm{kW\,kg^{-1}}$ and energy densities of between 4 and 5 $\mathrm{kWh\,kg^{-1}}$ with specific capacitances of 25-30 F per gram of activated carbon [37][38].

With a view on developing commercially viable solutions to improving supercapacitor performance, it is important to understand the costs typically involved with such devices. A typical mid size commercial supercapacitor can provide about 350 Farads [38]. Assuming a performance of $30\,\mathrm{F\,g^{-1}}$, this means that a mid size commercial device contains about 11.66 g of activated carbon, 0.69 g of binding agent and 1.37 g of conductive additive. At a rough price of \$15 USD/kg for activated carbon from coconut husk [39], \$15 USD/kg for PTFE binding agent [40] and \$0.08 USD/kg for carbon black [41], this equates to an electrode material cost of approximately \$0.19 USD per device with additives making up about 5.5% of the cost.

The limitations in supercapacitor performance indicate that special attention needs to be paid to increasing porosity and conductivity in supercapacitor electrodes. It is noteworthy that the characteristics that make for a high performance supercapacitor, namely high surface area, high porosity, high conductivity and good structural resilience and integrity, are also characteristics that research teams are looking for in high performance battery electrodes and in particular, high performance Li-S batteries. With these comparisons drawn, it should be clear then that the search for intelligently engineered, sustainable and high performance materials and geometries for electrodes applies equally to the development of supercapacitors as it does for next generation Li-S batteries. It follows that the performance of supercapacitor devices developed with these electrodes should give a good idea of the potential performance of these electrodes in applications in Li-S batteries.

3.3 Carbon Nanofibre Composites

Within the umbrella of electrode material research and structure design, there is a wide variety of strategies aimed at developing high performance and intelligently designed electrodes for batteries and for supercapacitors. In the next few pages, strategies for developing structures and materials for high performance electrodes for both Li-S batteries and supercapacitor electrodes will be discussed. In the case of Li-S batteries, proper electrode design should seek to contain polysulfide formation and migration while increasing electrode conductivity and while seeking to accommodate the most active material possible in order to optimize cell capacity. This can be achieved by designing highly conductive materials with high porosity and high surface area. Because carbon is naturally abundant and widely available, a wide variety of intelligently designed 3D and free-standing carbon frameworks have been proposed to achieve high sulfur loading and facilitate charge transport. For example, microporous carbon spheres were used to trap elemental sulfur within the pores and achieved a loading of 42% and stable cycling up to 500 cycles [42]. Mesoporous carbon with tuneable porosities have been used in a similar fashion and have achieved sulfur loading up to 50% and a capacity of 1390 mA h per gram of sulfur [43]. Other carbon materials like multi-walled carbon nanotubes have been used to create composite cathodes with similar capacities of 1352 $\mathrm{mA\,h\,g^{-1}}$[44], and graphene has been employed to wrap and encapsulate sulfur particles, leading to a stable specific capacities of 600 $\mathrm{mA\,h\,g^{-1}}$ over 100 cycles [45]. Other strategies include the use of conductive polymers, carbon-foams, carbon blacks, hollow carbon, carbon nanofibres, carbon cloth and hierarchical porous frameworks. The different strategies used to encapsulate sulfur into high-

performance Li-S cathodes are summarized in Fig 3.6.

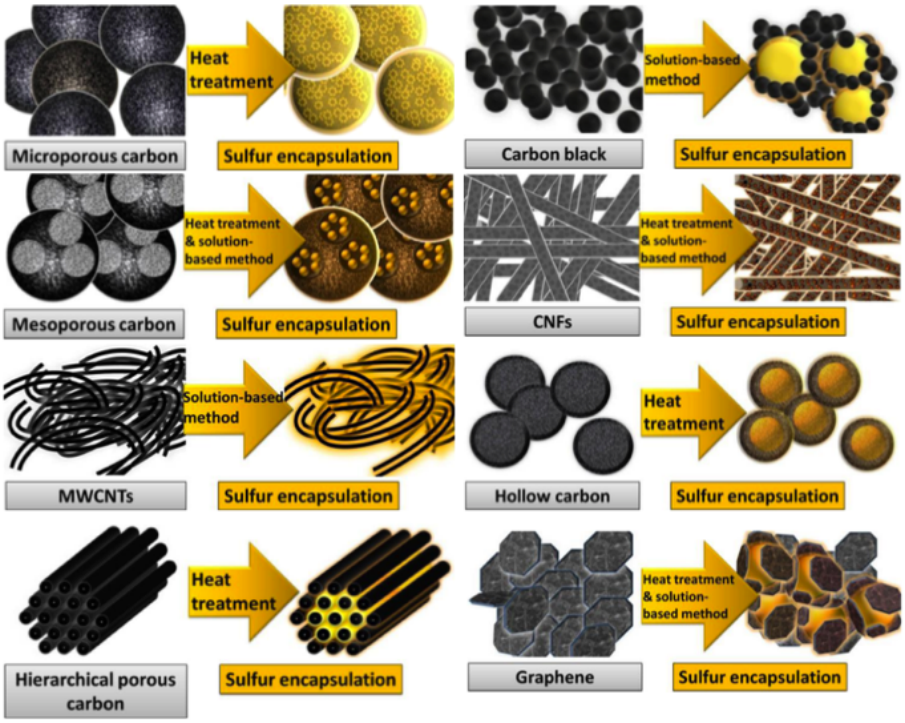

Figure 3.6: Different strategies for encapsulating sulfur in 3D frameworks (adapted with permission from [46]).

Because supercapacitor performance is tied to some of the same characteristics as Li-S electrode performance, it is not surprising that many of the same strategies for developing high performance Li-S electrodes have been applied to supercapacitors. In particular, 3D architectures with high specific surface areas are regularly employed for supercapacitor electrodes. Typically, a carbon material with a surface area of $1000\,\mathrm{m^2\,g^{-1}}$ could achieve a theoretical specific capacitance of between 200-500 $\mathrm{F\,g^{-1}}$. For example, Zhu et al. developed supercapacitor electrodes from activated graphene and achieved a gravimetric capacity of $150\,\mathrm{F\,g^{-1}}$ [47]. In another work, electrodes were prepared from carbon nanotubes and achieved high

capacitances of 170 F g^{-1} [48]. Like for batteries, functioning research stage supercapacitors have been prepared from a variety of other materials including carbon blacks, carbon aerogels and carbon/polymer composites.

Of the myriad of strategies for developing intelligently engineered 3D electrode architectures for Li-S batteries and for supercapacitors, the use of carbon nanofibres (CNFs) stands out as one of the more promising. CNFs are well suited for use in electrodes because of their structural integrity and high conductivity. Additionally, they can be prepared in interconnected mats with varying degrees of connectivity, which, when used in Li-S electrodes, have the ability to contain large amounts of sulfur while maintaining interconnected and conductive pathways within the cathode. On top of its contribution to the conductivity properties of the electrodes, this interconnectivity is attractive because it contributes to the structural integrity of the electrode and can mean that electrodes can be prepared binder free and without a current collector. Because of this interconnectivity, structural robustness and high conductivity, carbon nanofibres are suitable for many different types of energy storage electrodes including for supercapacitors and not just for Li-S specific applications. The use of carbon nanofibres as an electrode material is a popular strategy and high performance electrodes have been demonstrated for lithium-air batteries [49]. To date, this approach has been used sparingly for applications in Li-S batteries but there does exist examples of successful applications in the literature. For example, hollow carbon nanofibres were used to encapsulate sulfur and deliver a discharge capacity of 1170 mA h g^{-1} and retained good performance even after 200 cycles [50]. In another example, a nano-carbon/sulfur composite used carbon nanofibres as the electrical conductor and achieved a similar initial discharge capacity of 1200 mA h g^{-1} and good stability after 50 cycles

[51]. In supercapacitor applications, the use of carbon nanofibres is already quite popular with many devices being demonstrated to date [52].

While generally structurally strong and highly conductive, ECNFs suffer from a specific surface area that is typically lower than those of carbon nanotubes or graphene ($240\,m^2\,g^{-1}$ vs 1315 and $909\,m^2\,g^{-1}$ respectively)[53–55]. In the case of Li-S composite cathodes, high specific surface area of the supporting carbon matrix can benefit performance by providing additional interfaces between sulfur and the conductive framework. Additionally, it has been demonstrated that high porosity in carbon composite cathodes can help to capture the various polysulfide species present during cycling and can facilitate the passage of ions in the cathode [56]. These benefits can lead to increased long-term cycling stability and to reduced internal cell resistance. In supercapacitor applications, both electrical double layer capacitance and pseudocapacitance rely on surface effects at the electrode and so high surface area is necessary for supercapacitors requiring high charge capacity. The low specific surface area and low porosity of traditional carbon nanofibres has hampered carbon-nanofibre based electrodes in the past.

To solve this problem of low surface area and porosity, porous CNFs have been developed using a variety of different methods. Recently, porosity in nanofibres has been achieved through chemical treatment after electrospinning. Wang et al. demonstrated porous fibres made using this method with specific surface areas reaching $699\,m^2\,g^{-1}$ and developed supercapacitor devices with capacitances of $170\,F\,g^{-1}$ [57]. Another popular method is to electrospin blends of immiscible polymers followed by selective removal of one of the polymers during the heat treatment step [58, 59]. Abeykoon et al. prepared fibres in this way from PAN and PMMA, and achieved a very high specific surface area of $2419\,m^2\,g^{-1}$ with a

capacitance of $140\,\mathrm{F\,g^{-1}}$ for their supercapacitor devices [60]. Similarly, Tran and Kalra used PAN and Nafion to produce fibres with surface areas of $1600\,\mathrm{m^2\,g^{-1}}$ [61]. Finally, highly porous ECNFs have been created by electrospinning combined with a template method in which sacrificial polymers are dissolved from the fibres after electrospinning. Using this method, Wang et al. dissolved PVA from PAN fibres and obtained nanofibres with specific surface areas of $1232\,\mathrm{m^2\,g^{-1}}$ and a capacitance of $202\,\mathrm{F\,g^{-1}}$ at low scan rates of $2\,\mathrm{mV\,s^{-1}}$ [62].

Examples of porous carbon nanofibres for Li-S specific applications are few and far between. In one example, Ji et al. synthesized porous carbon nanofibres for use in Li-S cathodes using the PAN/PMMA template method and loaded the prepared fibres with sulfur via a solution-based chemical reaction-deposition method [63]. The resulting cathodes achieved a sulfur loading of 42% and a discharge capacity of $1400\,\mathrm{mA\,h\,g^{-1}}$ with promising signs of cycling stability after 30 cycles. In another work, Zhou et al. doped microporous polypyrrole based nanofibres with nitrogen to achieve Li-S cathodes with a sulfur loading of 60% and a discharge capacity of $1532\,\mathrm{mA\,h\,g^{-1}}$ [64]. While these works remain promising, the issues of cost and sustainability remain to be considered in these works. There remains significant opportunity for developing high performance Li-S batteries from porous carbon nanofibre based electrodes.

3.4 Electrospinning

Carbon nanofibres can be made in the research setting in a number of highly effective ways, including by phase separation methods, by synthesis by template and by polymer drawing [65, 66]. Despite the success of these methods, there remains great challenges in adapting these research-scale methods to the industrial scale

[67]. Of the ways of fabricating nanofibres, electrospinning stands out as a fabrication method that suits large-scale production well. In the emerging field of nanofabrication, electrospinning has become a popular and widely used method to obtain large quantities of carbon nanofibres with a high degree of control during fabrication. Electrospun carbon nanofibres (ECNFs) have a high surface area to volume ratio and have been used in a variety of applications, from energy storage to clothing. Significantly, ECNFs can be spun from a diverse set of materials including polymers, semiconductors, ceramics and polymers and are made as very long continuous fibres making them ideal for applications in electronics where conductivity is of high importance [68].

The beginnings of modern day electrospinning technology first appeared in the 19^{th} century, but it wasn't until the early 20^{th}, with the advent of high voltage power sources and soluble polymers, that patents relating to electrospinning first began to appear. In the early 90's electrospinning saw a huge rise in popularity after Doshi and Reneker demonstrated its use in the preparation of nanofibres [69]. The method that they proposed and that is still in use today is extremely attractive for nanofibre production in experimental settings because of the simplicity in its design. Specifically, electrospinning in its most basic form requires only a high voltage power supply, a collector and a syringe with a flat tip. As the 90's progressed, the research community experimented with this new method of nanofibre fabrication and much work was published on the topics of characterization of electrospun materials and analysis of optimal electrospinning conditions. Today, electrospinning as a process is relatively well understood and groups are moving towards the fabrication of devices using electrospun materials.

The electrospinning process relies on charge repulsion in an electroactive poly-

mer induced by an external magnetic field. In a modern electrospinning apparatus, a small droplet of viscoelastic solution is held at the end of a spinneret, usually a flat-tipped needle on a syringe. In its rest state, the droplet is affixed to the tip of the syringe by its own surface tension. When the device is switched on and an electric field is applied, charge is induced at the surface of the droplet. As the magnitude of the electric field is increased, additional charge is induced, creating mutual charge repulsion which causes a force directly opposite to that of the surface tension. With further increase in the intensity of the external field, the drop elongates along a uniaxial axis creating what is referred to as the "Taylor Cone" [69]. At a certain critical field intensity, the force due to the surface tension is overcome by that of the repulsive electric force, causing the charged jet of solution to be ejected from the tip of the needle towards a collector. As the jet of solution travels through the space between the syringe and the collector, the solvents present in the solution have the opportunity to evaporate providing they are volatile enough. By the time the jet reaches the collector, what remains is a long continuous charged polymer fibre which collects in a random pattern on the collector, thus producing a non-woven and highly interconnected mesh.

The process, while conceptually relatively easy to understand, is effected by a number of different electrospinning parameters. In particular, the properties of the resulting nanofibres are influenced by the viscosity, the conductivity, the surface tension, the magnitude of the electric field, the atmospheric humidity, the hydrostatic pressure in the needle, the temperature, and the air velocity in the chamber among other things. Electrospinning can be tailored to produce a variety of fibre sizes ranging from less than 0.05 microns to above 5 microns in diameter and over 100 different types of electrospun nanofibres have been reported [71]. Addition-

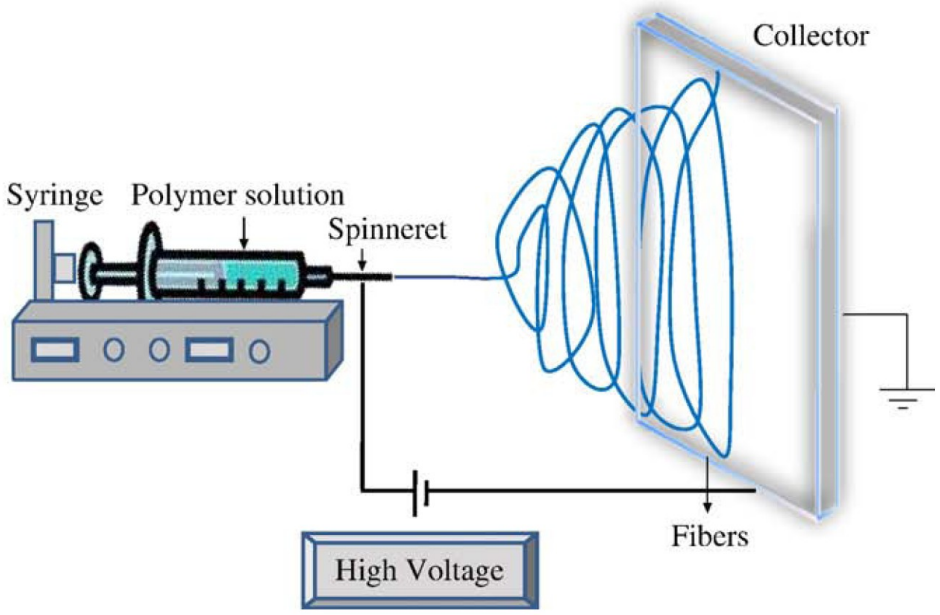

Figure 3.7: Typical electrospinning setup (reproduced with permission from [70]).

ally, modern applications of electrospinning have yielded fibres with tuneable cross sectional shapes and have even provided the ability to spin composite fibres with more than one polymer. A typical electrospinning set-up is shown in Fig 3.7.

The jet produced from the tip of the spinneret can be divided into three main portions during electrospinning which are visualized in Fig 3.8. In the cone jet, or the Taylor cone, which is the cone jet portion of the stream directly connected to the spinneret tip, the viscoelastic solution begins to pick up velocity as it exits the spinneret and is pulled by the electrostatic force. Once the critical voltage has been reached, the solution can break free of the cone jet and is pulled out into a stable jet region. In this jet, the electrostatic forces continue to stretch the material and the mass density of the jet remains constant along the stable jet region. As

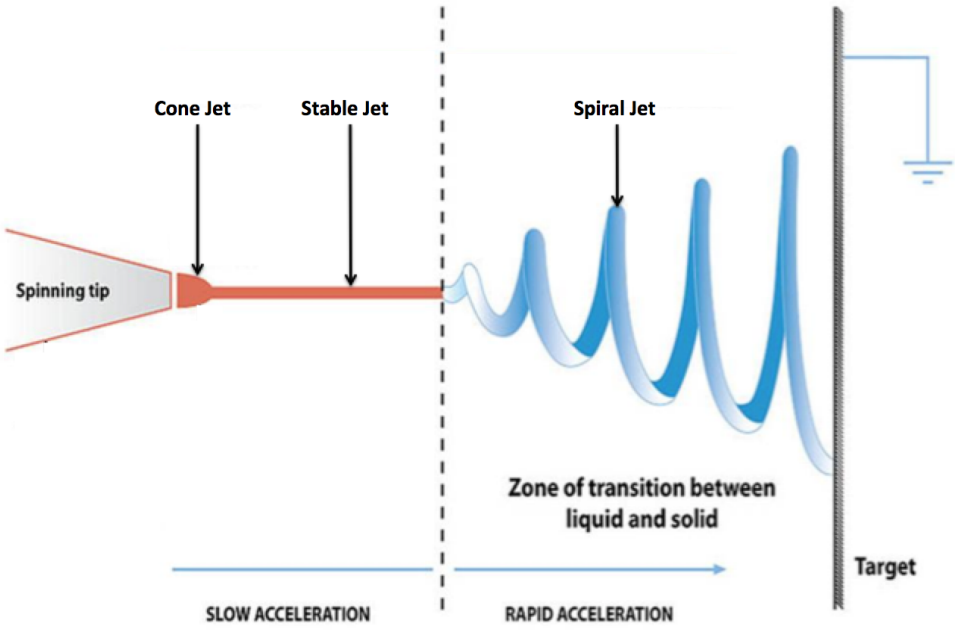

Figure 3.8: Close-up of the structure of the electrospinning jet (adapted with permission from ref [72]).

the electrostatic forces pull the charged particle in the jet towards the collector, the elongational velocity in the jet resists the motion, causing the jet to elongate as the solvent evaporates from the jet. The elongation and the evaporation of the solvent dynamically alter the viscoelastic parameters in the jet until eventually the radial forces caused by the electric charges in the jet become larger than the forces causing the jet to maintain its cohesion and uniaxial direction. Once this occurs, a spiral jet is formed. The forces present during this stage cause the spiral jet to move in a very haphazard and whipping motion. It is during this whipping motion that the fibres are stretched into their final nanometer scale diameter as they are deposited randomly on the collector [73]. By the time the fibres have deposited onto the collector, the solvent has, for the most part, evaporated and what is left is

a continuous non-woven mat of polymer.

One of the most important parameters to consider during the electrospinning process is the surface tension associated with the solution being spun. It is this tension that causes a liquid to resist forces that try to pull against it and is a function of the level of cohesion of molecules at the surface that face the external atmosphere. Within the bulk of the liquid, individual molecules are pulled equally in all directions by the forces associated with the molecules that surround them. At the surface however, the molecules there are subject to bulk forces in only one direction, causing a them to be pulled towards the bulk liquid and form a surface. The surface molecules contract towards the bulk of the liquid which in turn, causes a certain amount of pressure to build up in the liquid. During electrospinning, internal repulsive forces are created and when these forces exceed the surface tension forces, the liquid is expelled in a jet. The surface tension of a liquid therefor plays a big role in determining the shape of the jet and, if not balanced correctly, can lead to formation of beads on the jet. If the surface tension is too low, as is often the case if the concentration of polymer in solution is too low, then the solution can agglomerate and result in beads on the fibres. Higher concentrations of polymers in the spinning solution tend to decrease the chance of bead formation. Bead formation can sometimes be rectified by lowering the voltage or by increasing the distance between the spinneret and collector [74].

As well as surface tension, viscosity plays a key role in the eventual shape of the electrospun fibres. Since viscous forces tend to resist the pull from the electrostatic forces, solutions with higher viscosities have been shown to result in fibres with larger diameters while low viscosity solutions lead to thinner fibres. Additionally, if the viscosity is too low, fibre formation can be inhibited all-together leading

to the development of a spray rather than a jet [75]. Along with viscosity, solution conductivity and the dielectric properties of the solvent used can greatly effect the final diameter of the electrospun nanofibres. With a highly conductive solution comes a greater amount of charge accumulation in the jet, leading to higher repulsive forces and therefore a lower critical voltage. This can lead to more uniform fibres which can be further made uniform by increasing the number of ions in solution [68]. Adding to this effect, high solution dielectric properties can further increase the repulsive forces within the jet which in turn will increase the speed of the jet as it leaves from the spinneret. This has been shown to reduce bead formation [76].

Finally, two more factors that can effect the final dimensions of the prepared nanofibres are applied voltage and the feed rate of the electrospinning solution. A higher applied voltage leads to higher accumulation of electric charge inside the jet. As previously mentioned, it is when the repulsive forces inside the jet exceed the forces due to the surface tension that the jet is expelled from the spinneret. A higher applied voltage means that the jet is released sooner, leading to a shorter Taylor cone. Additionally, the increased repulsive forces means there are higher elongational forces within the jet. This leads to faster solution movement and in turn, smaller fibre diameters [77]. On the other hand, the increased forces means that the jet reaches the collector sooner and it has been demonstrated that, for certain high voltages, this can result in less time for elongation and so thicker fibres [78]. Beyond this, high voltages can lead to splitting of the jet, which again, may lead to thinner fibres [79]. Solution feed rate can also lead to changes in the final diameter of the prepares nanofibres with higher feed rates resulting in increased fibre diameters and lower feed rates leading to thinner fibres.

Due to its ability to continuously output high amounts of high quality nanofibres, electrospinning has been identified as an ideal candidate for scaling up the production of research quality nanofibres for industrial and commercial applications. With the progress in electrospinning research, a number of high output devices featuring high controllability of the parameters discussed above have been developed. One example of such a device, is the Katotech Nanofibre Electrospinning Unit. These devices, while still designed for use in the research setting, are demonstrating the scalability of the technique and have allowed for further understanding of the effect of the electrospinning parameters on the final nanofibres. With the development of devices relying on electrospun nanofibres, we can expect further development of industrial and commercial scale electrospinning units. Indeed, companies like Donaldson Torit DCE are already operating commercial scale electrospinning units.

In the research setting, electrospinning has been used successfully for applications in sensors, biomedical devices, filtration, textiles, magnetic devices and energy storage among many others [80]. For energy storage applications, electrospinning is particularly appealing as an electrode fabrication technique due to its ability to create highly interconnected and conductive mats of carbon nanofibres with highly tuneable properties and from many different precursor materials. The use of ECNFs in energy storage has extended from fuel cells, to battery anodes and cathodes, to supercapacitors, to electrolytes and even to separators. Additionally, these applications have taken advantage of the simplicity of the technique to engineer highly tuneable components from a wide variety of materials, from Polyacrylontrile (PAN), to polyvinylpyrrolidone (PVP) to Nafion. The versatility of electrospinning, the advantages associated with the technique and the nanofibres

that it can produce make it highly suitable for nanofabrication in the field of energy storage and the search for the right combination of parameters and materials continues to be important for developing revolutionary energy storage devices.

3.5 Lignin

To date, the large majority of research on ECNFs has focused on PAN derived fibres due to the ease of electrospinnability and favourable electrical and structural properties provided by the organic polymer. Despite its chemical and physical suitability, PAN is expensive and, because it is a derivative of petroleum, is non sustainable. Recently, increased efforts have been dedicated to searching for inexpensive, naturally abundant and environmentally sustainable sources of precursor carbon for ECNFs. This is particularly important for applications in energy storage which, as a field is moving towards more environmentally friendly and sustainable practices. While some groups have had success producing CNFs from highly sustainable precursors such as fungi [81], seaweed [82], eucalyptus and potatoes [83], one of the more promising materials is a material called lignin. As a major component in the cell walls of many plants, lignin is, after cellulose, the second most abundant renewable carbon source on earth and comprises around 30% of the weight of dry wood [84]. lignin is a byproduct of the pulp and paper industry and close to 50 million tons of lignin are generated as waste worldwide each year [85].

Despite traditionally being viewed as a waste product, developing environmental waste regulations are advancing the appeal of the use of lignin in commercial products in industries ranging from energy production to agriculture. For example, Volkswagen is considering using lignin based carbon nanofibres in the production of automotive components and can achieve a 50% reduction in the cost of manu-

facturing relative to the use of PAN [86]. There are a number of different varieties of lignin, each a byproduct of different pulping processes. While each lignin variety differs in terms of its chemical and structural properties, Lignosulfonates have long been the dominant lignin variety in the commercial sector, often being used in the construction and bitumen industries and to develop food and feed ingredients.

A second popular type of lignin is called Kraft lignin which is used for a variety of commercial applications. Kraft pulping is the most common form of chemical pulping in use today in the pulp industry and relies on a strong sodium sulfide catalyst to remove the lignin from the surround cellulose fibres in which it is found. Once the pulping stage is complete, the cellulose is bleached to further remove any remaining lignin. Often, the lignin that is removed from the cellulose is burned at the mill to supply energy for the functioning of the mill but just as often, it is discarded as waste. Kraft lignin is distinct from lignosulfonates and does not contain the sulfonate groups present in lignosulfonates. Kraft lignin is used primarily in applications such as dyes and pesticides and currently, is only used commercially to a very limited degree [87].

In addition to environmental waste regulations, the use of lignin in commercial applications is being pushed forwards by a number of drivers including high crude oil prices, booming bioeconomies around the world, and rapidly increasing interest in sustainability across all industries. These drivers are being fuelled by rapidly advancing production/treatment processes, increased collaboration between industries and the advent of modern biorefineries. Despite these seemingly favourable conditions, widespread adoption of lignin as a material for commercial products requires new business models, further technological advancement and better supply chain networks.

As a potential source of carbon for battery electrodes, lignin is an attractive precursor material for a global battery industry that is demanding cheap and sustainable component materials. If lignin can be incorporated into high performance next generation batteries, the energy storage industry may be the catalyst required to help the lignin industry realize its long-awaited potential. Interestingly, due to the high aromatics content in the macromolecules of lignin, the biopolymer is well suited as a precursor for the synthesis of carbon materials that are being considered for next generation battery applications. Recently, lignin has been used successfully in energy storage applications in a number of studies. For example, lignin derivatives were used in polypyrrole composites to create renewable cathodes with high specific capacitance values [88]. Even more recently, groups have taken advantage of the ability of lignin to form into nanofibres to explore the use of lignin derived carbon nanofibres for energy storage applications.

Depending on the type of lignin, a lignin molecule is composed of various combinations and ratios of three basic phenyl propane monomeric sub-units: Coumaryl Alcohol (H), Coniferyl Alcohol (G) and Syringyl Alcohol (S). Typically, hardwood lignin has a S/G ratio of 2:1 while softwood lignins have a ratio of around 1:2 or 1:3 [89]. The production of lignin-based carbon nanofibres from lignin can be divided into three basic steps: i) spinning of lignin solution; ii) thermal stabilization of as-spun lignin nanofibres at temperatures around 250°C in air and iii) carbonization of stabilized fibres at temperatures upwards of 800°C in an inert environment (Fig 3.9). After spinning is complete, a thermal stabilization process is essential to the production of carbon nanofibres because it prevents melting of fibres during the carbonization step. During thermal stabilization, molecules become crosslinked, weak intermolecular bonds become broken, ketones and car-

bonic acids form and autoxidation of aldehydes occurs [90]. These processes increase the glass transition temperature of the lignin, which allows the fibres to remain intact during carbonization[89]. During the carbonization at high temperatures, functional groups are eliminated from the lignin molecules leaving behind a conductive carbon backbone and graphitic structures. Additionally, during carbonization, macroscopic fusions between fibres are created, resulting in a highly interconnected structure that is ideal for energy storage electrodes because it eliminates the need for binders or current collectors [89].

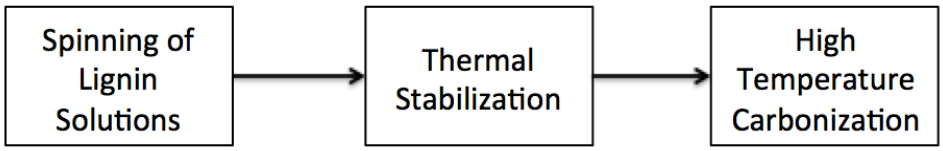

Figure 3.9: 3 Step process for lignin-based carbon nanofibre preparation.

Lignin can easily be formed into carbon nanofibres, a strategy that has been pursued for applications in supercapacitors and in both anodes and cathodes for batteries. Successful integration of lignin into energy storage technologies will represent a significant step in the search for sustainable storage devices. A variety of different methods can be used to prepare carbon nanofibres from lignin precursors. For example, Chatterjee et al. used a melt spinning processing to prepare carbon fibres with graphitic nanoscale domains [91]. In recent years and because of its scalability, electrospinning has been proposed as a method for producing lignin based carbon nanofibres. Non porous CNFs have been successfully fabricated using this method [92, 93]. By adding porosity to these fibres to increase the surface area, electrospun lignin-based carbon nanofibres may constitute an ideal electrode material for Li-S batteries and energy storage devices in general. Porous lignin

nanofibres have been prepared successfully ([94, 95]), but despite these works, there have been few reported studies of porous lignin based ECNF electrodes for energy storage applications and fewer examples of porous lignin based ECNF electrodes with tuneable fibre porosity and high surface area.

Chapter 4

Lignin-based Porous Carbon Nanofibre Electrodes

With the vast amounts of waste lignin being produced by the pulp and paper industry, and because of the suitability for this material for carbon nanofibre preparation, there exists a significant opportunity for development of high performance energy storage device electrodes from this material. In reviewing the literature, it is clear that optimal energy storage electrodes should be highly conductive, should have good mechanical resilience and flexibility, ideally should be free-standing and light weight, should have high porosity and surface area, should be low-cost and easy to produce from highly scalable fabrication techniques and should be sustainable. In this work, the electrospinning process was selected as a highly scalable and simple method of fabricating highly conductive and interconnected carbon nanofibres to be used as a conductive matrix for free-standing electrodes. Because high surface area and porosity has been demonstrated as a characteristic of high performance electrodes in both supercapacitor and battery applications, ECNFs require further modification.

In order to develop porosity in ECNFs, a template method was selected in which lignin is co-electrospun with small amounts of polytheylene oxide (PEO).

The PEO is then selectively removed from the fibres prior to carbonization via a facile hydrothermal treatment step. This step will be shown to be effective at removing PEO from the surface of the fibres to create high levels of porosity and to increase the specific surface area of the fibres significantly. The resultant matrix is highly conductive and consists of a web of highly porous ECNFs with fused junctions.

4.1 Materials & Methods

4.1.1 Materials

Powder of softwood kraft lignin was obtained from FP-Innovations and was dried in a vacuum oven for 24hrs at 50°C before use. PEO powder with a molecular weight of 900,000 was obtained from Sigma-Aldrich and was used as-is with no additional treatment. Spectroanalyzed N,N-Dimethylformamide (DMF) was obtained from Fisher Scientific.

4.1.2 Electrospinning

Spin dopes with mass ratios of lignin to PEO of 99/1, 98/2 and 97/3 were prepared by first dissolving PEO in DMF and stirring at 80°C for 1 hour. PEO served as a plasticizer to aid in electrospinning. It was found that spinning solutions with higher or lower proportions of PEO resulted in fibres containing high amounts of beads or in a lack of fibre formation all together. Lignin was simultaneously and separately dissolved in DMF and stirred by magnetic stirrer at 80°C for 30 minutes with intermittent periods of heavy agitation using a vortex mixer, followed by ultrasonication with a Sonics Vibracell tip sonicator for 30 minutes with a repeated pattern of 5 seconds of sonication followed by 5 seconds of rest to ensure full

dispersion. Next, the lignin solution was combined with the PEO solution in the appropriate amounts and the resultant solution was stirred for an additional 1 hour at 80°C, again with intermittent periods of heavy agitation with a vortex mixer. To ensure spinnability of the solutions, the ratios of lignin to DMF for each of the three solutions were as follows: 35% for ECNF(99/1), 32% for ECNF(98/2) and 29% for ECNF(97/3). It was found that attempting to electrospin solutions with higher amounts of PEO lead to poor to no fibre formation during electrospinning, and that attempting to spin without the addition of PEO lead to no fibre formation due to too little fibre viscosity.

The electrospinning setup consisted of a KatoTech Co. Ltd. NEU Nanofibre Electrospinning Unit with an electrically grounded and aluminum foil covered stainless steel rotating drum of diameter 10 cm as the fibre collector. Solutions were loaded into a 10 ml syringe with a Luer-Lok tip and a 20 guage blunt-tip stainless-steel needle and a built-in syringe pump was employed to dispense the solution and maintain a distance of 17 cms between the syringe and the drum. Electrospinning was completed using a positive voltage bias of 17 kV and a flow rate of $4.3\,\mathrm{ml\,hr^{-1}}$. The solution was stirred continuously during electrospinning with a home-made magnetic stirring apparatus. Atmospheric humidity was kept between 28% and 32%. Electrospinning in a non controlled, high humidity atmosphere lead to fibres containing moisture beads.

4.1.3 Removal of Sacrificial Polymer

Porous Lignin/PEO fibres were prepared by submerging as-spun fibre mats in deionized water and gently agitating for at least 12 hours at a temperature of 80°C in order to dissolve the sacrificial PEO polymer from the fibres. It was found that

a soaking time of 12 hours was necessary to remove the all of the PEO from the surface of the fibres and that soaking for longer than this did not contribute to additional mass loss from the fibres in a significant way. The fibre mats were then removed from the water and dried on a stainless steel rack in a vacuum oven at 50°C for 12 hours.

4.1.4 Stabilization and Carbonization

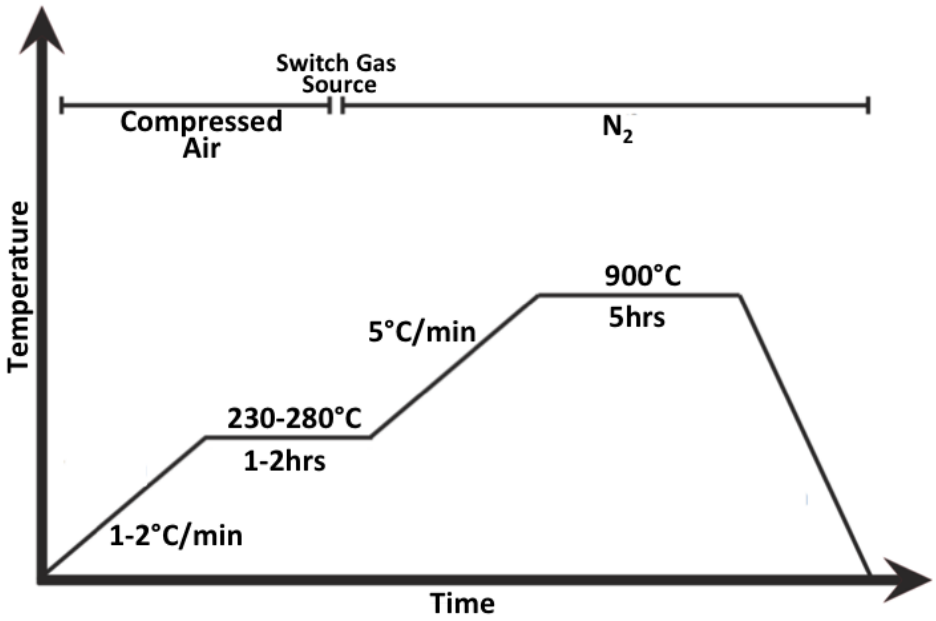

Figure 4.1: Graphical representation of the stabilization and carbonization process.

In order to convert the electrospun fibres into conductive carbon nanofibres, fibre mats were placed on stainless steel racks in a Thermo Scientific F21135 furnace, with a controllable gas input and a mineral oil bubbler to regulate positive

pressure. Stabilization was done by heating the fibres in air to the stabilization temperature of 230-280°C from room temperature at a rate of 1-2°C min^{-1} and holding for 1-2 hours. Next, the fibres were carbonized by heating the fibres from the stabilization temperature to a carbonization temperature of 900°C at a rate of 5°C min^{-1} and holding for 5 hours followed by natural cooling to room temperature. A constant flow of nitrogen was maintained during carbonization. A graphical representation of the stabilization and carbonization process is shown in Fig 4.1. The fabrication process for graphitic nanofibre mat electrodes is summarized in Fig 4.2.

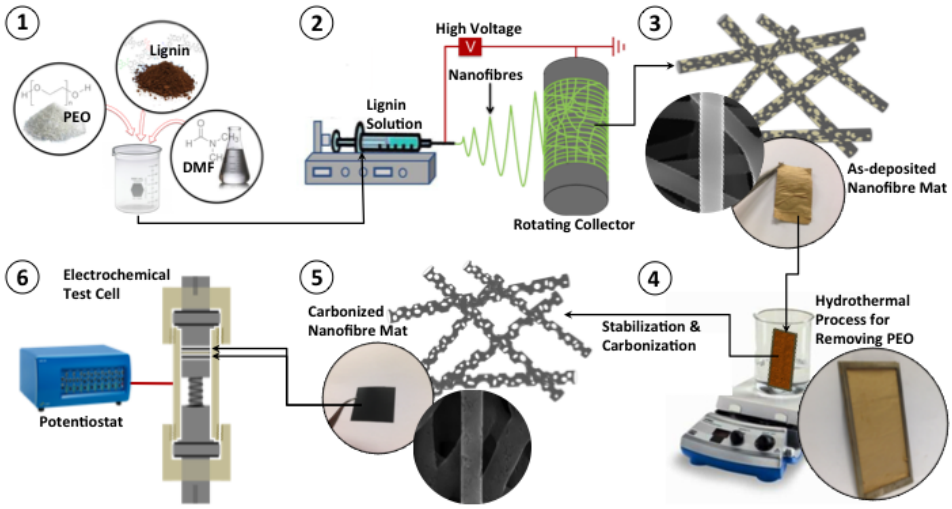

Figure 4.2: Fabrication process for porous lignin-based nanofibre mat electrodes: (1) preparation of spin dope from PEO, lignin and DMF, (2) electrospinning of lignin nanofibres, (3) appearance of as-spun lignin nanofibres, (4) hydrothermal treatment step, (5) appearance of carbonized and porous nanofibres and (6) test cell schematic for electrochemical testing.

4.2 Characterization and evaluation

Fibre morphology was evaluated with a Zeiss Sigma Scanning Electron Microscope. Fibre diameters were determined using the SmartSEM software and by sampling at least 10 different fibres for each sample. Conductivity measurements were taken via a two probe method using a Tektronix Precision Multimeter with fast drying silver paint being used to ensure good electrical contact between the fibres and the probe and to secure the sample to a glass slide. For this measurement, the fibres were cut into 3 mm wide and 20 mm long strips and the resistance of the fibres was measured for at least 10 different samples. X-Ray diffraction patterns were acquired with a Bruker D8-Advance X-Ray diffractometer in the Bragg-Brentano configuration operated at 40 kV and 40 mA with Copper Kα_1 & Kα_2 radiation and a Nickel filter to filter the CuKβ radiation. For these XRD measurement, ECNFs were milled in a mortar and pestle to create a fine powder which was then dropped onto a glass slide. Raman Spectroscopy was performed with a Horiba Jobin Yvon HR-800 spectrometer with a laser wavelength of 633 nm. Pore sizes were measured using Quantachrome Autosorb 1-MP gas sorption analyser. TGA curves were acquired with a Q500 thermogravimetric analyzer from TA Instruments. In a typical run, the temperature was increased from room temperature to 800°C in an air atmosphere at a rate of 10°C min^{-1}. The sample was purged by flowing air at a rate of 60 ml min^{-1}.

4.3 Results and Analysis

4.3.1 Carbonization Parameter Optimization

To demonstrate the viability of electrospun lignin/PEO nanofibres and to search for optimal carbonization conditions, we prepared a solution of DMF containing 30% softwood lignin and 0.3% PEO by weight relative to the weight of solvent. This solution was successfully electrospun with fibres exhibiting a smooth and uniform morphology but it was noted beads appeared on the electrospun fibres if the atmospheric humidity reached above 35%. The fibres, which contain approximately 99% lignin and 1% PEO were then stabilized in air for two hours at 230°C after being heated from room temperature at a rate of $1^{\circ}\mathrm{C\,min^{-1}}$. Next, a high temperature carbonization step was employed. It is in this step that all non-carbon elements are eliminated and graphitic-like structures develop in the fibres which can influence the final conductivity of the CNFs [96]. For this reason, optimizing the conditions under which these structures form is important. In order to determine the optimal carbonization temperature to produce fibres with high conductivities, fibres were carbonized in nitrogen for 5 hours at various temperatures (550, 700, 800, 900 and 1000°C). The carbonization heating rate was set to $5^{\circ}\mathrm{C\,min^{-1}}$ in all cases. The electrical conductivity of the fibre mats was calculated from the following equation:

$$\sigma = \frac{L}{t\,w\,R} \tag{4.1}$$

where L is the length of the mat in cm, t is its thickness, w is its width and R is the electrical resistance in Ω. Here, R was obtained using the aforementioned

two probe method. The prepared fibres exhibit a conductivity of 2.16 S cm^{-1} for a carbonization temperature of 900°C and a falling conductivity for lower and higher carbonization temperatures as shown in table 4.1. These results were calculated from at least 5 samples of each type. Fibres carbonized at 900°C are smooth and have an average diameter of 443 nm (s.d. = 69 nm).

Carbonization Temperature	**Conductivity (S cm^{-1})**
550°C	1.9*10^{-7} (s.d. = 1.4*10^{-8})
700°C	0.26 (s.d. = 0.02)
800°C	1.57 (s.d. = 0.09)
900°C	**2.16 (s.d. = 0.16)**
1000°C	1.41 (s.d. = 0.13)

Table 4.1: Conductivities of lignin/PEO ECNFs(99/1) after stabilization at 230°C and carbonization at various temperatures.

It was found that further optimization could be achieved by varying the stabilization temperature. Many processes occur during this oxidative stabilization step including cross-linking, dehydrogenation, cyclization, aromatization and oxidation which lead to the formation of a thermally stable ladder-like structure. By optimizing the conditions under which these processes occur, nanofibres with improved performance characteristics can be created [97, 98]. Table 4.2 presents the measured conductivities of fibres prepared with stabilization temperatures from 230-280°C and with the carbonization temperature held constant at 900°C. Fibres stabilized at a temperature of 250°C had the highest conductivity of 2.71 S cm^{-1}. The remainder of fibres in this work were fabricated using the optimized stabilization temperature of 250°C and carbonization temperature of 900°C.

After optimizing the stabilization and carbonization temperatures, the effect of stabilization rate and time on the final fibre conductivities was explored. The prepared fibres were stabilized using four different combinations of commonly used

Stabilization Temperature	Conductivity (S cm^{-1})
230°C	2.16 (s.d. = 0.16)
250°C	**2.71 (s.d. = 0.13)**
280°C	1.68 (s.d. = 0.09)

Table 4.2: Conductivities of lignin/PEO ECNFs(99/1) after stabilization at various temperatures and carbonization at 900°C.

stabilization rates and stabilization times. The fibres were then carbonized as usual and conductivity of the fibres was measured. The results, presented in Table 4.3 indicate that a stabilization rate of 2°C min^{-1} and a stabilization time of 2 hours leads to the highest fibre conductivity. The remainder of the fibre mats presented in this work were prepared under the following optimized conditions: increase temperature to the stabilization temperature of 250°C in air at a rate of 2°C min^{-1} and hold for 2 hours and then increase temperature to the carbonization temperature of 900°C at a rate of 5°C min^{-1} and hold for 5 hours in a N_2 atmosphere.

Time \ Rate	1°C min^{-1}	2°C min^{-1}
1 hour	3.83 (s.d. = 0.28)	4.54 (s.d. = 0.17)
2 hour	2.71 (s.d. = 0.13)	**7.31 (s.d. = 0.65)**

Table 4.3: Effect of stabilization time and rate on the conductivities of lignin/PEO ECNFs(99/1). Conductivity values reported with units S cm^{-1}.

4.3.2 Microstructural Observations

With stabilization and carbonization conditions optimized, electrospun carbon nanofibres with lignin to PEO ratios of 99/1 (ECNF(99/1)), 98/1 (ECNF(98/2) and 97/3 (ECNF(97/3) were spun and submerged in water to remove the PEO before being subjected to the heat treatment regime described above. The resulting porous carbonized fibres (P-ECNFs) were then characterized. For comparison, charac-

terization of non porous ECNFs(99/1) was also completed. Fibre microstructures were observed through SEM images after carbonization and the fibre diameters were measured from the images by sampling at least ten different fibres from each image. SEM images for all fabricated ECNFs and P-ECNFs show consistent fibre formation with few to no beads. Fig 4.3 shows the SEM pictures of non porous ECNFs(99/1). Fibre formation is very regular and the fibres have a smooth appearance with little to no mesopores visible. Additionally, the fibres appear to have fused together at the junctions, a feature that does not appear to as great at extent in fibres that have had the PEO removed before carbonization.

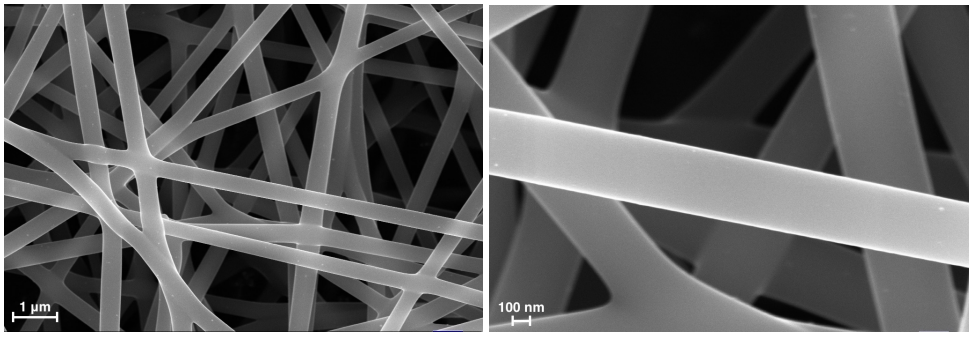

Figure 4.3: SEM images of ECNF(99/1) at magnifications of 10k and 40k.

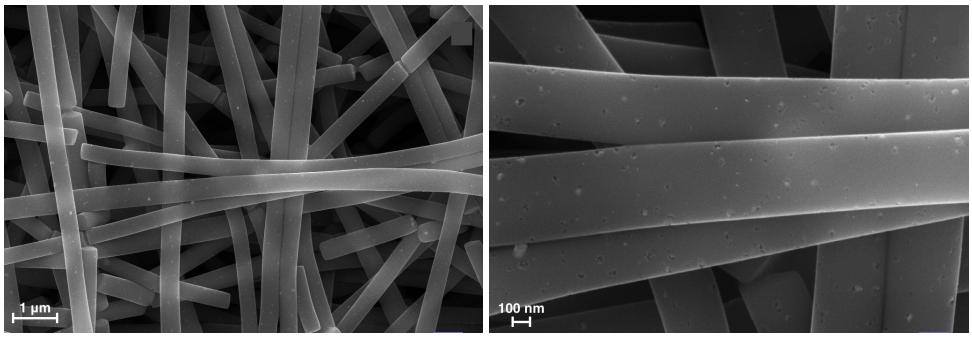

Figure 4.4: SEM images of P-ECNFs(99/1) at magnifications of 10k and 40k. Additional images can be found in Appendix C.1.

Fig 4.4 shows SEM images of porous P-ECNFs(99/1). These fibres are again well formed and of consistent diameter but differ from their non-porous counter parts in that there are numerous breaks in the fibres. These may indicate the presence of pockets of PEO in the fibres which, when dissolved, cause the remaining fibres to become disjointed. Alternatively, these breaks may be an indication of the increased brittleness of the fibres caused by the removal of the PEO prior to carbonization. The images also reveal the presence of obvious pores in the fibres, although these pores are relatively few and widely dispersed along the fibres. The presence of pores in the washed fibres indicates that PEO has been successfully removed from the fibres prior to heat treatment.

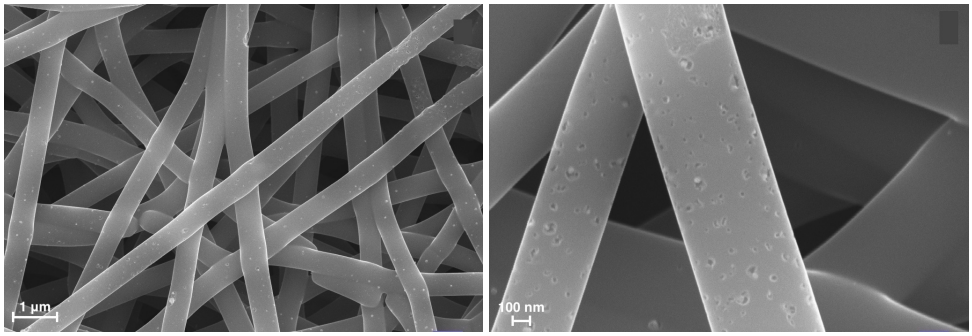

Figure 4.5: SEM images of P-ECNFs(98/2) at magnifications of 10k and 40k. Additional images can be found in Appendix C.2.

P-ECNFs(98/2), seen in Fig 4.5, are significantly more porous than P-ECNFs(99/1) and appear to fuse to each other to a greater extent than do the P-ECNFs(99/1). This is also a feature of the non washed fibres and so may indicate that some PEO remains in the fibres prior to carbonization. The P-ECNFs(98/2) appear well formed but give the appearance of a more fluid and less rigid overall structure, a feature that again may be explained by the presence of left-over PEO in the fibres prior to

carbonization. The presence of pores in these fibres is much more obvious than in P-ECNFs(99/1) and in the non washed fibres, again confirming that the hydrothermal treatment step was successful in removing bubbles of PEO that were present on the surface of the fibres.

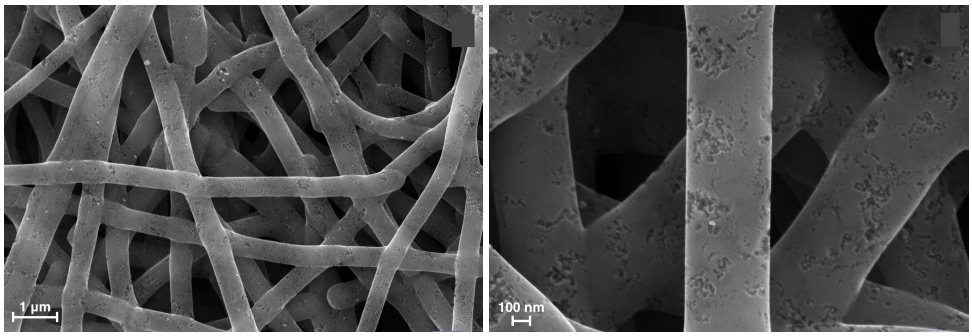

Figure 4.6: SEM images of P-ECNFs(97/3) at magnifications of 10k and 40k. Additional images can be found in Appendix C.3.

Finally, Fig 4.6 show P-ECNFs(97/3) which, compared to the other fibres, are heavily porous with a wide variety of pore sizes that are dispersed all over the fibres although not as regularly as the other porous fibres discussed above. The high level of porosity in these fibres suggests once again that hydrothermal treatment was successful in removing PEO agglomerations on the surface of the fibres. Fibres are bead free and well formed but with periodic breaks in the fibres. P-ECNFs(97/3) show a very fluid and "melted" appearance with crossing fibres fused together at their junctions which as before, may indicate that some amount of PEO remains in the fibres prior to carbonization and after the hydrothermal treatment step. The fused nature of the fibres may suggest high conductivity of the P-ECNFs(97/3) mats.

Fibre diameters were measured using the SmartSEM software and are pre-

Fibre Type	Fibre Diameter (nm)
ECNF(99/1)	$439.60(s.d. = 53.71)$
P-ECNF(99/1)	$464.40(s.d. = 52.22)$
P-ECNF(98/2)	$468.88(s.d. = 53.11)$
P-ECNF(97/3)	$428.12(s.d. = 55.87)$

Table 4.4: Average diameters of different ECNFs and P-ECNFs.

sented in Table 4.4. Differences in average fibre diametres between the four different types of fibres may be expected, despite the fibres being electrospun under the same conditions. For one, varying the ratio of PEO to lignin in the spin dope may effect both the surface tension and the viscosity of the solutions, two factors which, as discussed earlier, may affect electrospun fibre diameter. Additionally, increased amounts of PEO in the as-spun fibres may lead to smaller fibres after the hydrothermal treatment step is completed. Despite these two factors, fibre diameters remained relatively consistent across the different fibre types, falling between 428.12 nm and 468.88 nm. The differences in diameters for the different fibres is not significant however and does not reveal a clear trend. Additionally, the diameter of the porous fibres did not seem to deviate significantly from that of the non porous fibres with the same precursor ingredient ratios (439.60 nm and 464.40 nm for ECNFs(99/1) and P-ECNFs(99/1) respectively).

4.3.3 Surface Area and Porosity

Nitrogen adsorption porosimetry was used to measure the specific surface area, pore volume and pore size distribution of each of the fabricated fibre mats. In nitrogen porosimetry, nitrogen is introduced to the sample under cryogenic temperatures in tiny doses to saturation pressure. Then, the excess gas is removed and the relative pressure and quantity of adsorbed gas is measured to give an adsorption

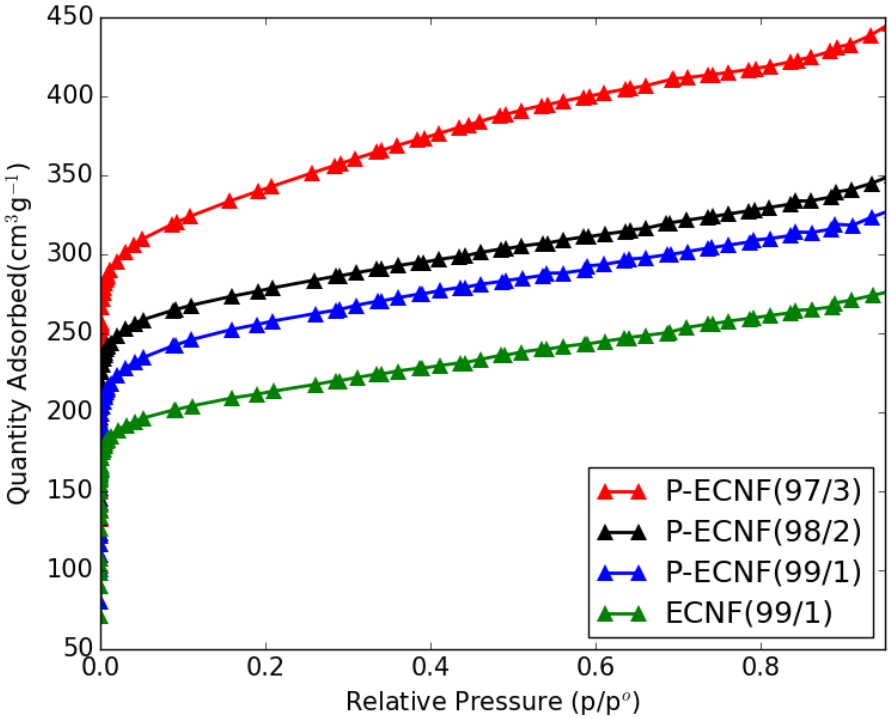

Figure 4.7: N_2 adsorption isotherms of the prepared P-ECNFs and ECNFs.

isotherm. The adsorption isotherms can be plotted as a straight line in the relative pressure range of 0.05 - 0.35, giving a BET plot. Specific surface area of the material can be calculated based on the slope (A) and the y-intercept (I) of this plot by way of the following equations:

$$v_m = \frac{1}{A+I} \tag{4.2}$$

$$S_{BET} = \frac{v_m N s}{V a} \tag{4.3}$$

where v_m represents the monolayer adsorbed gas quantity, N is Avogadro's number,

V is the molar volume of the adsorbate, a is the mass of the sample and s is the cross sectional area of the adsorbing species [99].

Fibre Type	SSA ($m^2\,g^{-1}$)	Pore Volume ($cm^3\,g^{-1}$)
ECNF(99/1)	816	0.42
P-ECNF(99/1)	974	0.49
P-ECNF(98/2)	1076	0.52
P-ECNF(97/3)	1258	0.65

Table 4.5: BET specific surface area and pore volume of different ECNFs and P-ECNFs acquired from N_2 adsorption isotherms.

The isotherms, presented in Fig 4.7 for each of the fibres, show an increasing level of adsorption in the low pressure region, followed by continued adsorption in the middle region and further continued adsorption in the high pressure region. This behaviour is characteristic of type 1 adsorption isotherms under the Brunauer classification system which is characteristic of materials with high amounts of micropores. The total quantity of adsorbed gas at each relative pressure was highest for P-ECNFs(97/3) and lowest for P-ECNFs(99/1) with the general trend indicating that those fibres with lower proportions of precursor PEO adsorbed less gas at each relative pressure. The BET method was used to evaluate the specific surface area of each of the fibres and the results are presented in Table 4.5. The results reveal that P-ECNFs(97/3) have a high specific surface area of $1258\,m^2\,g^{-1}$, a value that represents a 5-fold improvement over non porous PAN based CNFs [53] and a 54% increase compared to the non porous ECNFs(99/1), which have a specific surface area of $816\,m^2\,g^{-1}$.

The density functional theory (DFT) model was used to measure pore size distribution and the model used was the cylindrical pore non local DFT equilibrium model. The results, presented in Fig 4.8, reveal that all fibres contain a large volume

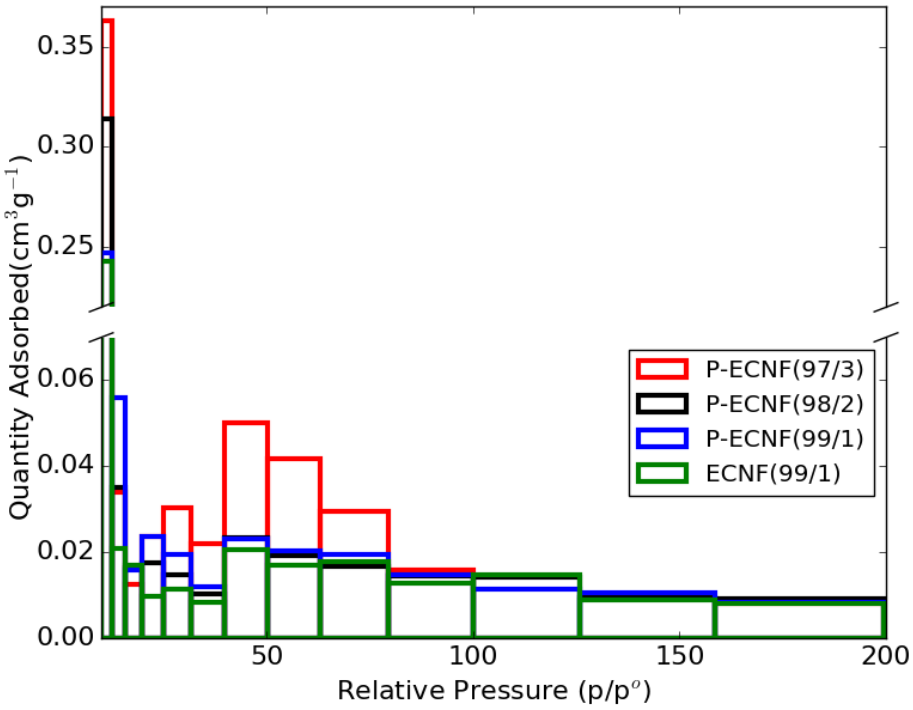

Figure 4.8: Pore size distribution histograms of the prepared P-ECNFs and ECNFs.

of micropores (<20Å) as predicted by the isotherm shape, with P-ECNFs(97/3) having the highest volume of micropores and with fibres with less precursor PEO having less micropore volume. Relative to micropores, all fibres have a smaller volume of mesopores (20-500Å) but are still significantly mesoporous. Again P-ECNFs(97/3) have a much higher volume of mesopores compared to the other fibres, particularly in the pore size range of 40 nm to 80 nm. The majority of the mesoporosity induced in the P-ECNFs(98/2) and P-ECNFs(99/1) appears to be in the 20-40 nm range.

The total pore volume of P-ECNFs(97/3) is a high 0.65 $cm^3\ g^{-1}$, again a significant improvement of 55% over the non porous ECNFs(99/1), which have pore

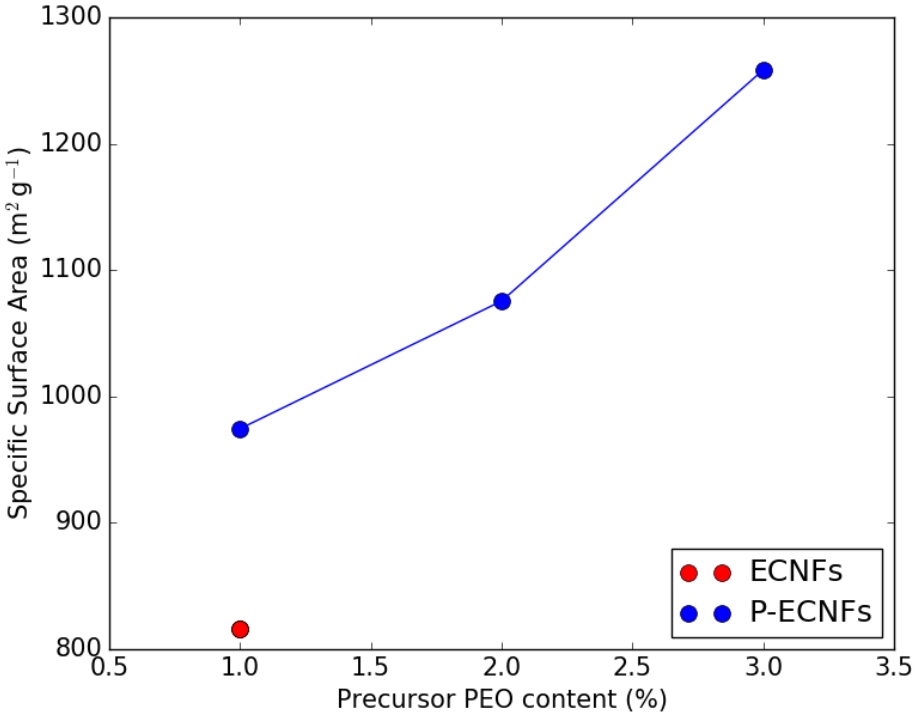

Figure 4.9: Specific surface area of ECNFs and P-ECNFs as a function of their precursor PEO content.

volume of 0.42 $cm^3\,g^{-1}$. The results indicate that removal of PEO from electrospun fibres prior to carbonization contributes to the formation of both micropores and mesopores in the fibres and that the volume of both micro and mesopores can be tuned by varying the amount of precursor PEO in the electrospinning solution. Specific surface area and total pore volume of the prepared fibres are visualized in Fig 4.9 and Fig 4.10 as a function of PEO content in the electrospun fibres.

4.3.4 X-Ray Diffraction Analysis

XRD analysis was performed on all ECNFs in order to further elucidate the microstructure of the porous fibres. In XRD, a concentrated beam of x-rays is directed

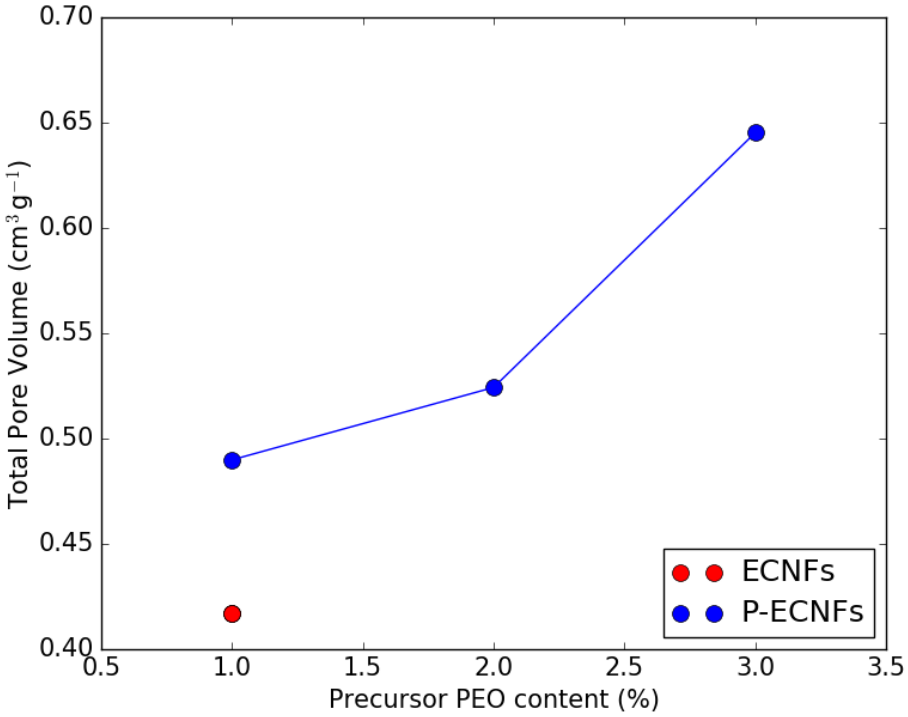

Figure 4.10: Total pore volume of ECNFs and P-ECNFs as a function of their precursor PEO content.

towards the sample using a cathode ray tube and a beam collimator. When incident x-rays have enough energy to dislodge electrons from the targets inner shells, a characteristic x-ray spectra is produced. When conditions satisfy Bragg's Law, that is when the following equation is satisfied:

$$n\lambda = 2d\sin\theta \tag{4.4}$$

where d is the interplanar distance of the crystal lattice, n is a positive integer, θ is the scattering of the x-rays and λ is the wavelength of the incident wave, the reflected x-rays will interfere constructively, producing a peak in x-ray intensity

when the diffracted x-rays are detected and counted. By scanning the x-ray beam through a range of 2θ angles, all possible diffraction directions of the lattice should be scanned resulting in a characteristic diffraction pattern. This pattern can then be compared to known patterns to better understand the composition of the material [100].

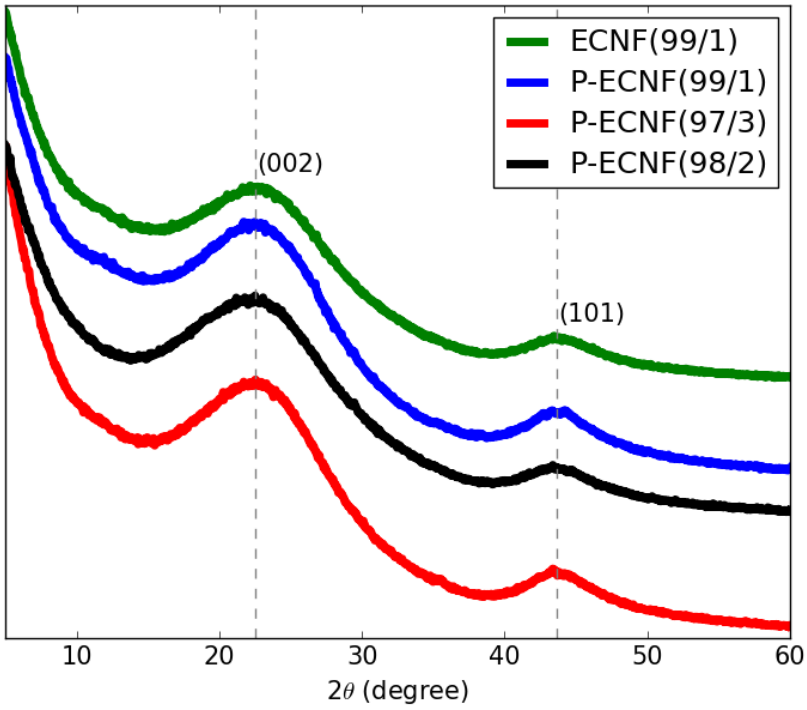

Figure 4.11: XRD patterns for different ECNF and P-ECNFs.

Fig. 4.11 presents the results of this analysis and reveals a broad diffraction peak for all P-ECNFs centred around 22-23. This peak is attributed to the (002) crystallographic plane of graphitic structures. A second weaker peak was also observed corresponding to the (101) plane of graphite at around 44 and the presence of which is a strong indication of graphite formation [101]. While these results do

point to the formation of graphitic structures within the fibres, the broad nature of the visible peaks indicate that the size of graphitic structures is small and the degree of crystallographic order is low [102]. Interestingly, the peaks for the porous fibres appear more pronounced than that of the non-porous fibres, indicating that graphitic order in the porous fibres may be higher than in the non porous fibres.

4.3.5 Lignin Fibre Conductivity

Fibre Type	**Conductivity (S cm^{-1})**
ECNF(99/1)	$7.31(s.d. = 0.65)$
P-ECNF(99/1)	$19.69(s.d. = 1.02)$
P-ECNF(98/2)	$18.91(s.d. = 0.62)$
P-ECNF(97/3)	$18.39(s.d. = 0.92)$

Table 4.6: Conductivity of prepared ECNFs and P-ECNFs.

Results of conductivity measurement show that P-ECNFs are highly conductive compared to non porous ECNFs with P-ECNFs(99/1) having a conductivity of 19.69 S cm^{-1} (s.d. = 1.02 S cm^{-1}) compared to ECNFs(99/1) which had a conductivity of 7.31 S cm^{-1} (s.d. = 0.65 S cm^{-1}). P-ECNFs(98/2) had a conductivity of 18.91 S cm^{-1} (s = 0.62 S cm^{-1}) while P-ECNFs(97/3) had a conductivity of 18.39 S cm^{-1} (s.d. = 0.92 S cm^{-1}). The results are summarized in Table 4.6 and Fig 4.12 and indicate that P-ECNFs are between three and four times more conductive than conventional PAN based ECNFs (4.90 S cm^{-1}) [103].

The differences in conductivities of the different fibres may be explained by the structural and morphological properties of the different fibres. XRD results revealed that differences in the heights of XRD peaks between the fibres with porous fibres having a much higher peak corresponding to the (002) plane of graphitic structures and a slightly more pronounced peak corresponding to the (101) plane.

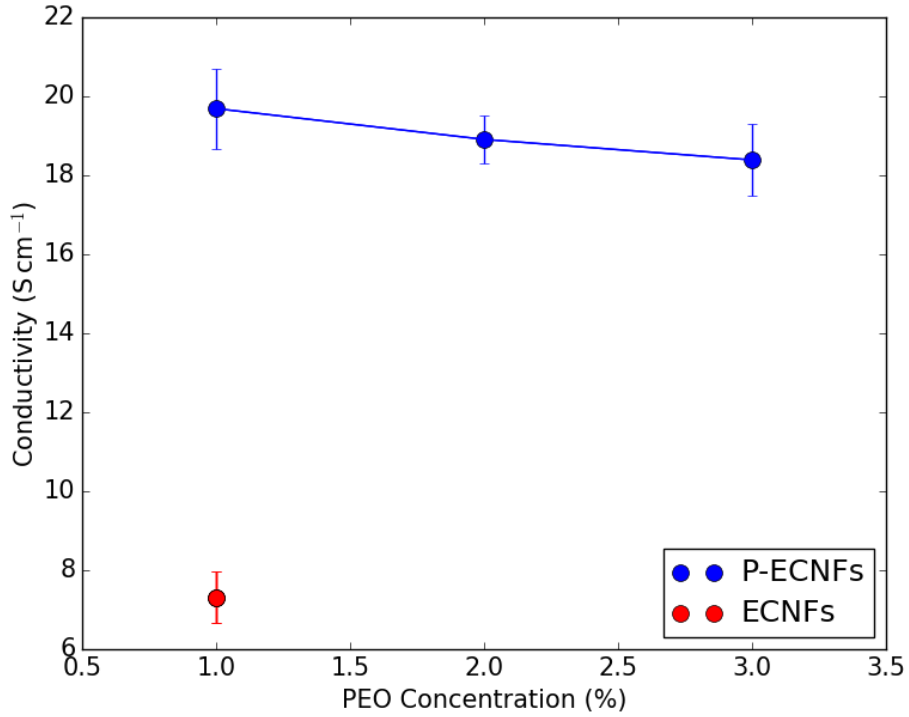

Figure 4.12: Conductivity of ECNFs and P-ECNFs as a function of their precursor PEO content.

This difference is consistent with the difference in conductivities between these groups of fibres indicating that indeed, the presence of graphitic structures in the fibres contributes to the conductivity of the fibre mat.

4.3.6 Raman Spectroscopy

Raman spectroscopy is another powerful technique with which one can identify the molecular composition of a material. Raman spectroscopy relies on scattering of monochromatic light directed onto the sample with the use of a laser. The reflected light experiences an energy shift caused by its interaction with the molecular vibrations present within the material. The Raman spectra is collected by a detector

and the resulting shift can be compared to the Raman spectra of known materials so identify the molecular make-up of the target material. The Raman shift can be calculated on the basis of the following equation:

$$\Delta w = (\frac{1}{\lambda_0} - \frac{1}{\lambda_1}) \times 10^{-7} \tag{4.5}$$

where Δw is the Raman shift in cm^{-1}, λ_0 is the excitation wavelength in *nm* and λ_1 is the Raman spectrum wavelength in *nm*.

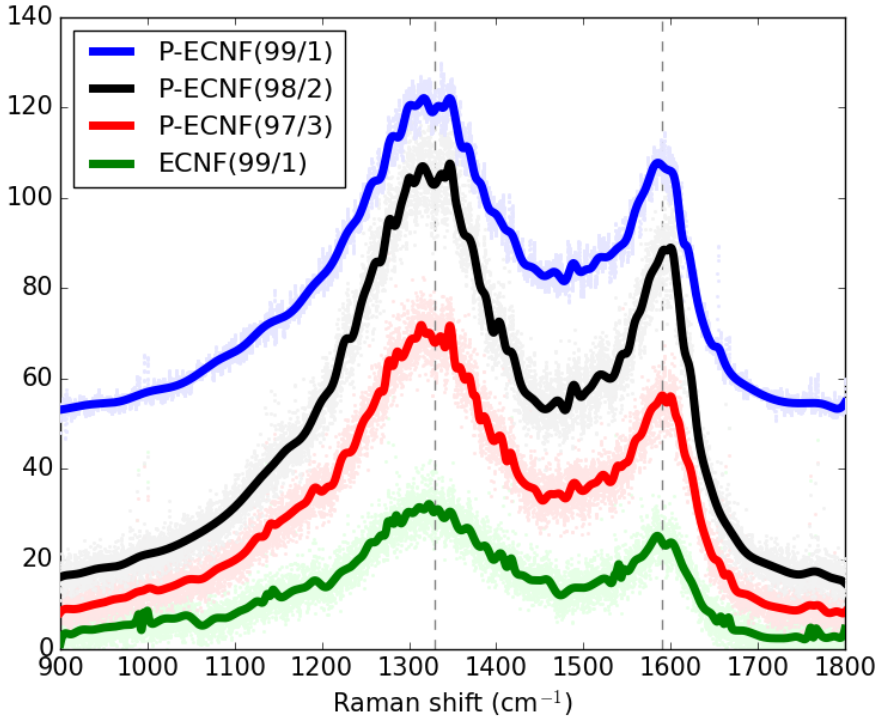

Figure 4.13: Raman spectra for different ECNF and P-ECNF.

Raman Spectra for all samples are presented in Fig 4.13 and reveal obvious peaks centred around 1330 and 1590 cm^{-1}. These peaks correspond to the D- and G-band peaks for carbons respectively. It is thought that the D-band is caused by

either defects in curved graphene sheets or is from the vibration of carbon atoms with dangling bonds in crystal lattice structures which may be due to plane terminations of disordered graphene [104]. The formation of the G-band on the other hand is from the vibration of sp^2-bonded carbon atoms in graphene sheets and other two-dimensional hexagonal structures [105]. By measuring the ratio of the intensity of the D-band (I_D) to that of the G-band (I_G), an approximate measure of the graphitic quality of fibres can be obtained with a lower ratio indicating fewer structural defects in the graphitized nanofibres. The I_D/I_G values were 1.48 for ECNFs(99/1) and 1.26, 1.29 and 1.35 for P-ECNFs(99/1), P-ECNFs(98/2) and P-ECNFs(97/3) respectively, indicating a slight decrease in graphitic quality of the fibres as the amount of PEO increased in the precursor electrospinning solution.

The results indicate that the formation of ordered graphitic structures during heat treatment may be disrupted by the addition and then removal of PEO from the fibres prior to the heat treatment step. As seen in Fig 4.12 and Fig 4.14, there is a strong inverse correlation between the I_D/I_G values of the fibres and their measured conductivities; fibres with lower I_D/I_G values (and therefore higher graphitic order) tended to have higher conductivities and vice versa. This correlation suggests once again that the graphitic order and quality within the fibres plays a significant role in determining the conductivity of the fibre mats. Additionally, the elevated I_D/I_G value for the non porous ECNFs(99/1) suggests that the presence of high amounts of PEO in the fibres during the heat treatment step may disrupt graphite formation and conductivity. Again, this result is consistent with the lower conductivity values observed for the non-porous ECNFs(99/1) and with the results of thermogravimetric analysis presented below.

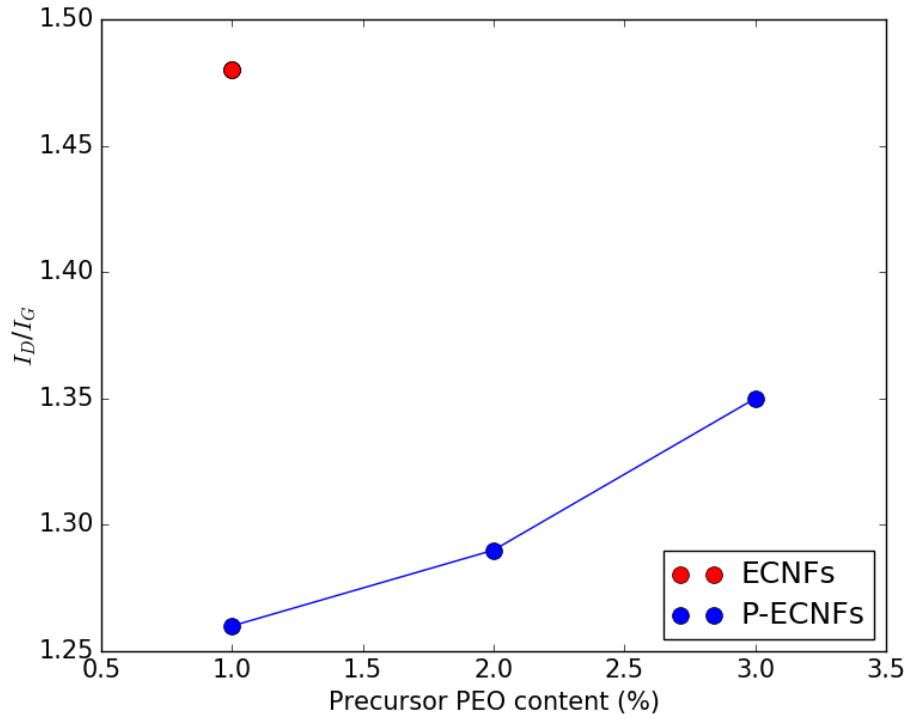

Figure 4.14: I_D/I_G values of ECNFs and P-ECNFs as a function of their precursor PEO content.

4.3.7 Thermogravimetric Analysis

Thermogravimetric analysis (TGA) is a powerful method that can be used to further understand and confirm the presence of different polymers in non carbonized nanofibres. In TGA, samples are heated to a specific temperature and at a constant heating rate. During heating, the weight of the sample is measured accurately resulting in a graph of percentage weight remaining as a function of temperature. In the case of PEO/Lignin fibres, TGA can be used to understand the composition of the fibres by taking advantage of the differences in decomposition profiles of the two polymers.

The significant surface area and porosity of the P-ECNFs suggests that the

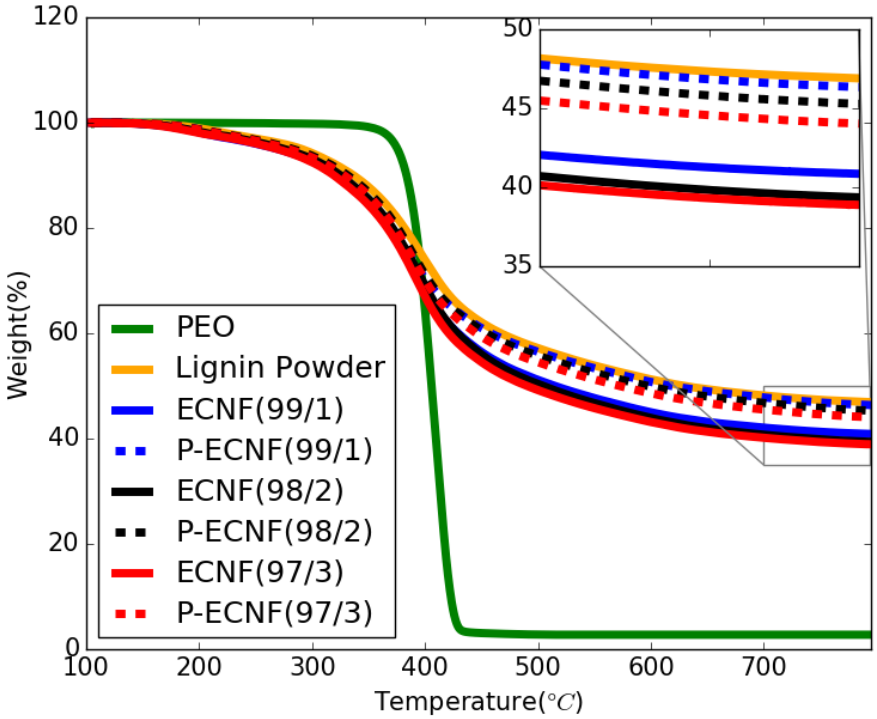

Figure 4.15: TGA profiles of P-ECNFs and ECNFs. The inset shows a magnification of the heating profile between 700°C and 800°C.

hydrothermal processing step presented in this work is effective at removing the sacrificial PEO from the lignin fibres to create micro and mesoporosity. TGA results can be further analysed to determine the true extent at which PEO removal was completed. Thermogravimetric analysis was conducted for all fibres prior to heat treatment to assess the components of the prepared P-ECNFs and ECNFs and to confirm the removal of the sacrificial PEO during the water treatment step. TGA curves in Fig 4.15 with solid lines show data collected from the prepared non porous ECNFs while dotted lines indicate measurements taken using the P-ECNFs. Additionally, TGA measurements were completed on both untreated lignin and PEO powders for comparison.

The results show that lignin powder begins to decompose at around 200°C and continues to decompose slowly until well over 700°C, eventually leaving over 47% weight as residue. This long thermal decomposition process may be due to the presence of numerous molecular weight fractions in the non fractionated lignin powder. On the other hand, the PEO powder, which is composed of a single molecular weight of PEO, begins to decompose at around 400°C and finishes decomposing almost completely at around 430°C. The fabricated non porous fibres follow a similar decomposition profile to that of the lignin powder. Despite the absence of a sharp drop in weight around 400-430°C as would be expected in fibres with a much higher proportion of PEO, even the small amounts of PEO cause the TGA profile to shift downwards compared with the lignin powder profile. This can be attributed to the additional loss of weight from the decomposition of the small amounts of PEO in the fibres with the profiles of those fibres containing the most PEO experiencing the most downward shift relative to that of lignin powder. As expected, the profiles for the porous fibres (P-ECNFs) are shifted up relative to the non porous fibres since these fibres have had most of their PEO removed during the hydrothermal treatment step and so should not expect as much material degradation during heating.

Interestingly however, the profiles of the three porous fibres are offset from each other slightly with P-ECNFs(99/1) and P-ECNFs(97/3) having the most and least final residue proportions respectively. This may suggest that not all of the PEO was removed from the fibres during the hydrothermal treatment step and that some PEO may remain in the fibres and particularly on the inside of the fibres which may not have been exposed to water. If all of the PEO contained in the fibre was removed, we should expect the TGA profile of that fibre to match the profile of

lignin powder. PEO remaining in the fibres may affect the morphology of the fibres and indeed, it appears that the fibres containing the most PEO before carbonization appear less straight and rigid in the SEM images. Instead, these fibres appear more fluid with rounded turns and more fusing of fibres.

Chapter 5

Supercapacitors From Porous Lignin-based ECNF Electrodes

As a demonstration of performance in electrical devices, supercapacitor devices will be used to test electrochemical performance of the prepared P-ECNF electrodes. Based on the results of electrochemical testing as well as the previously reported structural and morphological results, the prepared electrodes will be presented as a sustainable, low-cost and high performance platform framework on which the development of future high performance batteries and capacitors can be based.

5.1 Materials & Methods

5.1.1 Materials

P250-1 ACS Certified Potassium Hydroxide Pellets (KOH) with a molecular weight of 56.11 were obtained from Fisher Scientific. Celgard 2500 microporous membrane was purchased from Celgard Company for use as a separator.

5.1.2 Electrode Preparation

Circular electrodes were stamped from as-carbonized sheets of ECNFs using a gasket punch set purchased from General Tools Mfg. Co. and were 6mm in diameter. The mass of the circular ECNFs electrodes was measured with a Sartorius CPA225D semimicro balance. A Celgard 2500 microporous membrane was used as a separator and was stamped into circular pieces of 8 mm diameters. Electrodes and separators where then soaked in electrolyte for at least 6 hours prior to electrochemical testing. 6M KOH electrolyte was prepared by adding KOH Pellets to the appropriate amount of DI water and stirring for at least 1 hour.

5.1.3 Test Cell Fabrication

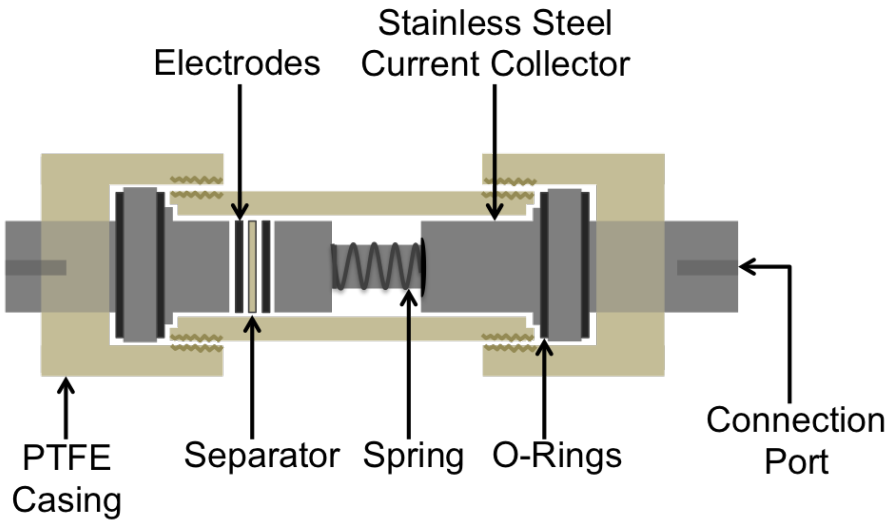

Figure 5.1: Schematic representation of the electrochemical testing cell.

Two-electrode cells were put together in a lab-designed testing cell (Fig 5.1) that included two stainless steel columns as current collectors surrounded in a PFA air-tight casing. Two electrodes were placed between the two current collectors

and separated by a Celgard separator and then the casing was filled with electrolyte using a syringe. O-rings were employed in strategic locations to prevent escape of electrolyte and to keep the cell closed to the atmosphere. An integrated spring system ensured that the testing cell applied the same pressure to the two electrodes across subsequent tests. The testing cell was connected to the testing equipment via a small connection port on either side of the test cell.

5.2 Characterization and Evaluation

Cyclic voltammetry (CV), galvanostatic charge/discharge at constant current (CC) and electrochemical impedance spectroscopy (EIS) of the two-electrode ECNF cell was completed using a Multipotentiostat VMP 300 from Bio-Logic and with a 6M KOH aqueous solution as the electrolyte. Scanning rates used for CV tests were 5, 10, 30 and 50 $\mathrm{mV\,s^{-1}}$ in the voltage window of 0 to 0.8 V. Constant current galvanostatic charge/discharge studies were performed at current densities of 400, 1000 and 2000 $\mathrm{mA\,g^{-1}}$ over the same voltage window. EIS measurements were performed over the frequency range from 0.1 Hz to 1 MHz.

5.3 Results and Analysis

5.3.1 Cyclic Voltammetry

Cyclic Voltammetry (CV) is an electrochemical analysis technique whereby a potential difference is applied across the electrodes of a supercapacitor cell and ramped at a continuous rate between two limit potentials. Once the upper limit potential has been reached, the voltage is then ramped back down to the lower limit potential to complete one cycle of the scan. By measuring the resultant current flow, a

CV trace can be produced which can yield information about the capacity of the electrodes, the voltage window of the supercapacitor and the cycle stability of the system. In an ideal capacitor, an applied voltage sweep creates a current according to the following equation:

$$I = \frac{dQ}{dt} = C\frac{dV}{dt} \tag{5.1}$$

where I is the current, Q is the charge and V is the voltage. Capacitance can therefore be estimated from CV curves by integrating the current over the voltage window and dividing by the voltage window and the scan rate as in the following equation:

$$C = \frac{\int_{E_1}^{E_2} i(E)dE}{2(E_2 - E_1)mv} \tag{5.2}$$

where C is the specific capacitance of the sample in Farads per gram ($\mathrm{F\,g^{-1}}$), E_1 and E_2 are the maximum and minimum voltages used in the scan in volts (V), i(E) is the current in amperes (A), m is the mass in grams (g) and v is the voltage scan rate in volts per second ($\mathrm{V\,s^{-1}}$). The result of this calculation multiplied by a factor of four is the capacitance value of an individual electrodes based on CV results for a two-electrode cell [106]. The CV trace of an ideal capacitor will appear as a rectangle with a constant current being produced as the voltage is swept across the voltage range. In practice and due to internal cell resistance and other effects, this is rarely the case but the degree of rectangularity of a CV curve can give an indication of the level of ideal supercapacitor behaviour being experience by the supercapacitor being tested.

Each of the porous fibres as well as the non porous ECNFs(99/1) were sub-

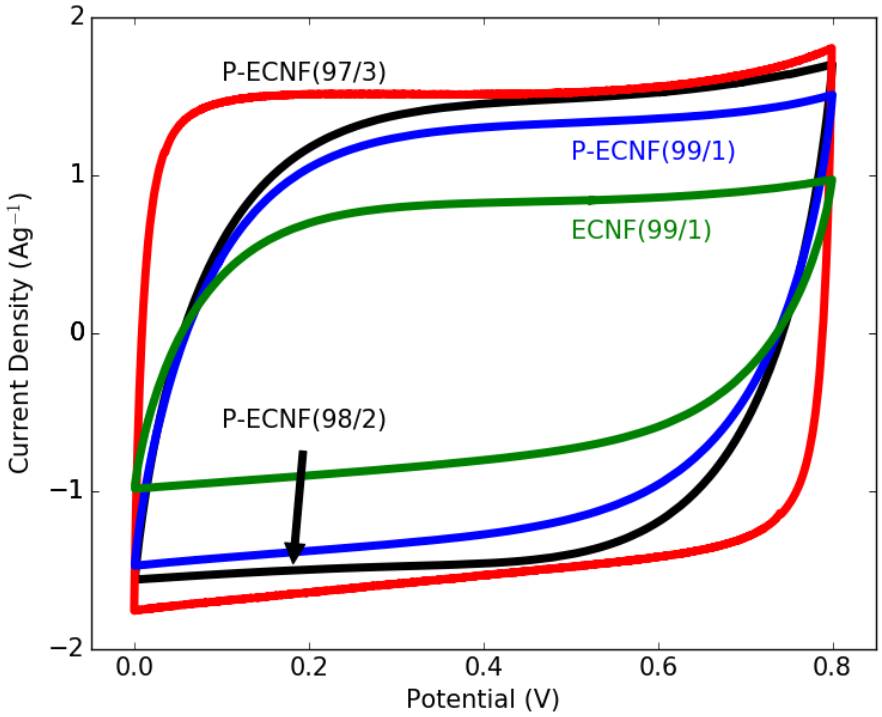

Figure 5.2: Cyclic voltammograms of different ECNFs at a scan rate of $30\,\mathrm{mV\,s^{-1}}$.

jected to CV testing. Scan rates used were 5, 10, 30 and $50\,\mathrm{mV\,s^{-1}}$. Of the four fibres tested and as seen in Fig 5.2 and 5.3, P-ECNFs(97/3) exhibited the most rectangular shaped curves with the largest areas at the high scan rates of 30 and $50\,\mathrm{mV\,s^{-1}}$. As the fibre porosity decreased, so too did the size and rectangular shape of the CV curves. Additional CV curves for scan rates of $10\,\mathrm{mV\,s^{-1}}$ and $5\,\mathrm{mV\,s^{-1}}$ can be found in Appendix A. The results indicate that P-ECNFs(97/3) would be the most suitable of the fibres tested for supercapacitor applications since they exhibit behaviour most closely approaching what would be expected from an ideal capacitor. Additionally, the shape and size of the CV curves for the different fibres indicates that P-ECNFs(97/3) may have the highest gravimetric capacitance.

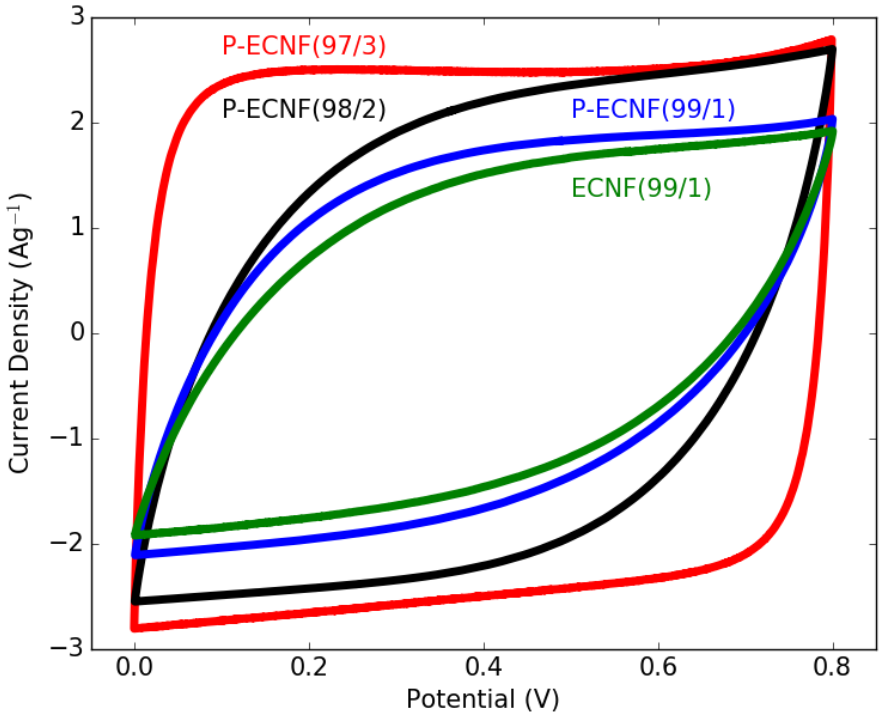

Figure 5.3: Cyclic voltammograms of different ECNFs at a scan rate of $50\,\mathrm{mV\,s^{-1}}$.

Specific capacitance of the electrodes was calculated from the CV curves based on Eqn 5.2 and are presented in Table 5.1. Results confirm that P-ECNFs(97/3) do indeed have the highest gravimetric capacitance of the fibres tested with a maximum measured capacitance of $112\,\mathrm{F\,g^{-1}}$. The demonstrated capacitance values show a clear trend of increasing specific capacitance as the ratio of precursor PEO to lignin increases in the fibres. Capacitance values of ECNF(99/1), P-ECNF(99/1), P-ECNF(98/2), P-ECNF(97/3) obtained at the scan rate of $5\,\mathrm{mV\,s^{-1}}$ where measured to be 78, 89, 105 and $112\,\mathrm{F\,g^{-1}}$ respectively. The increased specific capacitance of the more porous fibres can be attributed to the increased specific surface area of the P-ECNFs as the amount of precursor PEO in the fibres is

increased as well as the higher ionic accessibility of the more porous electrodes.

Fibre Type	5 mV s^{-1}	10 mV s^{-1}	30 mV s^{-1}	50 mV s^{-1}
ECNF(99/1)	78	70	55	43
P-ECNF(99/1)	89	81	61	51
P-ECNF(98/2)	102	94	71	54
P-ECNF(97/3)	112	105	98	95

Table 5.1: Gravimetric capacitance in F g^{-1} of ECNFs calculated from CV curves.

Next, volumetric capacitance was calculated for each of the prepared electrodes after carefully measuring the overall volume of the electrodes in the cell and multiplying the calculated gravimetric capacitance by the density of the electrode. The results, presented in Table 5.2 demonstrate a similar trend to the gravimetric capacitance results with the more porous fibres having a higher volumetric capacitance than the less porous fibres. P-ECNFs(97/3) had the highest gravimetric capacitance of 35 F cm^{-3} at a scan rate of 5 mV s^{-1}. Again, the results show that volumetric capacitance decreases as the scan rate is increased.

Fibre Type	5 mV s^{-1}	10 mV s^{-1}	30 mV s^{-1}	50 mV s^{-1}
ECNF(99/1)	18	16	13	10
P-ECNF(99/1)	23	21	16	13
P-ECNF(98/2)	31	29	24	21
P-ECNF(97/3)	35	33	31	30

Table 5.2: Volumetric capacitance in F cm^{-3} of ECNFs calculated from CV curves.

With the goal of examining the effects of increased sweep rates, P-ECNFs(97/3) were further scanned at sweep rates up to 200 mV s^{-1} with the resulting curves (Fig 5.4) revealing good rectangular profiles even at high sweep rates. The variation in capacitance at elevated sweep rates is an important factor to consider when designing supercapacitors for use at high rates. Capacitance values for P-

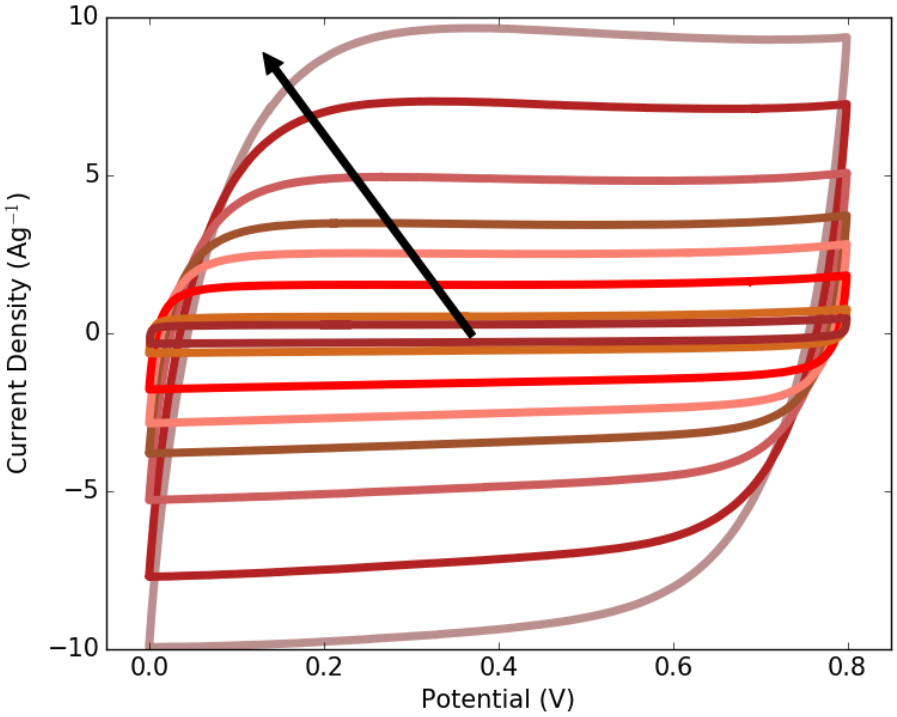

Figure 5.4: Cyclic voltammograms of P-ECNFs(97/3) at scan rates of (starting from the center and moving in the direction of the arrow) 5, 10, 30, 50, 70, 100, 150, and 200 mV s^{-1}.

ECNFs and ECNFs(99/1) at all sweep rates are displayed in Fig 5.5 and show that P-ECNFs(97/3) maintain high capacitance at elevated sweep rates. P-ECNFs(97/3) retained 84.4%, 78.8% and 71.1% capacitance at high rates of 50, 100 and 200 mV s^{-1} respectively compared to the measured capacitance at 5 mV s^{-1}, indicating excellent performance at high sweep rates.

This impressive performance at high sweep rates can be attributed to faster ionic transportation and shorter diffusion distances which occur in the more porous nanofibre structure [107]. This was a significant improvement on the P-ECNFs(98/2), P-ECNFs(99/1) and ECNFs(99/1) which could only maintain 65.2%, 57.0% and

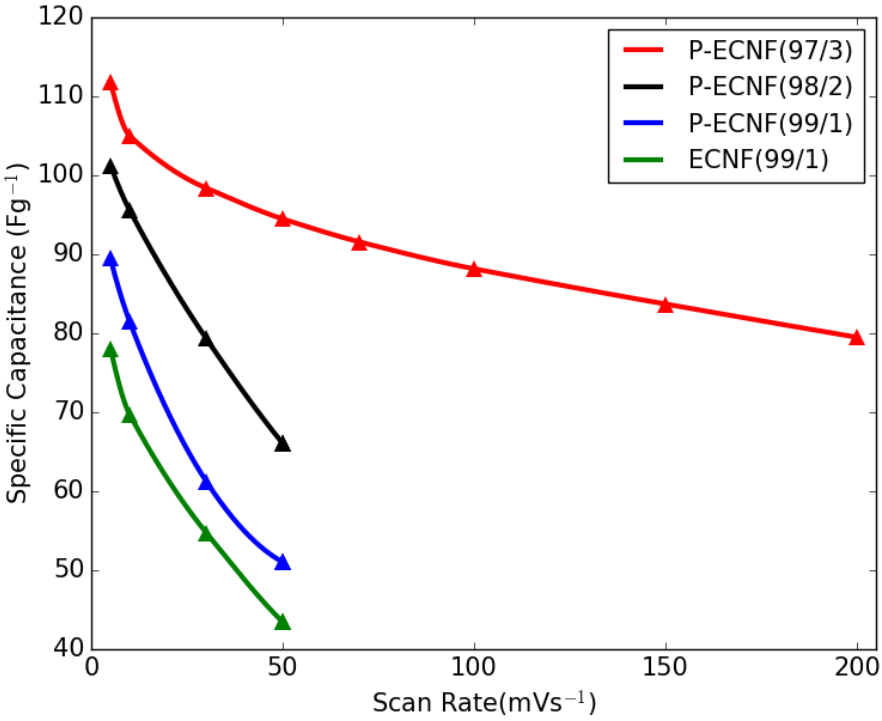

Figure 5.5: Specific capacitance of P-ECNFs calculated from CV curves at different sweep rates.

55.6% capacitance at a scan rate of 50 mV s^{-1} when compared to the measured capacitance at 5 mV s^{-1}. At sweep rates higher than 50 mV s^{-1}, the CV curves of P-ECNFs(98/2), P-ECNFs(99/1) and ECNFs(99/1) displayed poor rectangular shape, indicating a loss of reversible supercapacitor behaviour at high sweep rates. The less porous structures in these cases may contribute to increased diffusion resistance which would explain the loss of supercapacitor behaviour at higher rates.

5.3.2 Galvanostatic Charge/Discharge

To further analyze the electrochemical behaviour of the prepared electrodes, galvanostatic charge/discharge testing was conducted on all fibres at varying current

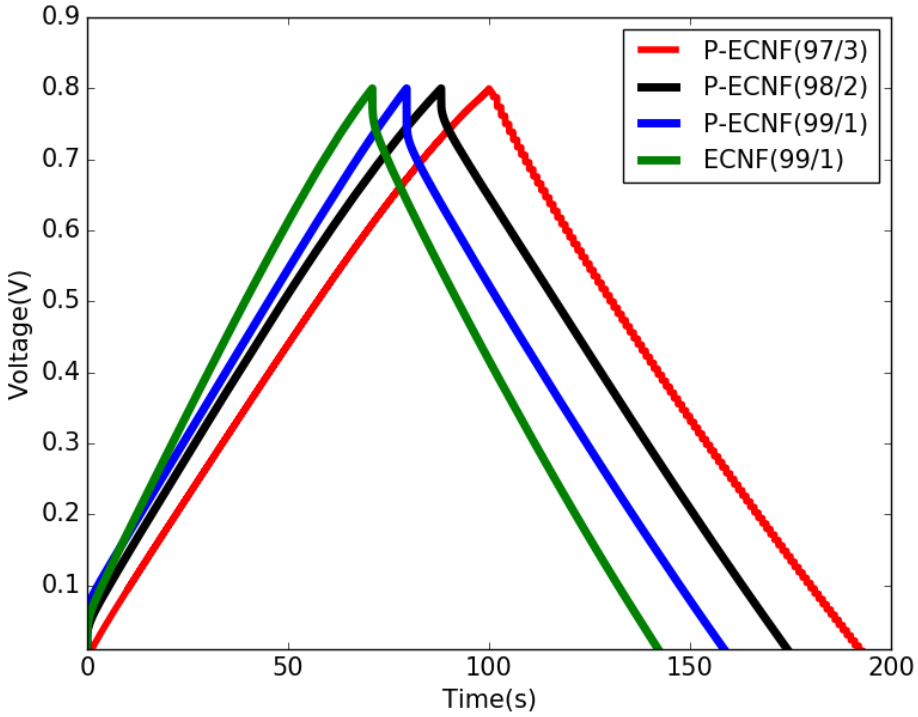

Figure 5.6: Galvanostatic charge/discharge curves of ECNFs and P-ECNFs at a current density of 400 mA g^{-1}.

densities. In galvanostatic charge/discharge testing, a constant current is applied across the electrodes of a supercapacitor and the resulting voltage is measured as a function of time. Once the voltage in the cell has reached a specific limit voltage, the current is reversed and the voltage diminishes until it reaches a lower limit voltage, at which point the cycle is repeated. The resulting curves for an ideal supercapacitor are perfectly triangular in shape with a lower discharge slope indicating better capacitance. In real capacitors, galvanostatic charge/discharge curves often exhibit a vertical drop in voltage at the moment the current direction is switched. This drop is referred to as an "IR drop" and is an indication of the level of internal resistance in the cell. Galvanostatic charge/discharge was performed at

current densities of 400, 1000 and 2000 mA g^{-1} for all fibres with typical results presented in Fig 5.6 for a scan rate of 400 mA g^{-1}. The results show good triangular shape with limited IR drop indicating promising reversible supercapacitor behaviour for all P-ECNFs, with the most triangular and elongated shape belonging to P-ECNFs(97/3). P-ECNFs(97/3) were further scanned at current densities up to 6000 mA g^{-1} with CC curves (Fig 5.7) continuing to maintain a good triangular shape with little IR drop even at high current densities. Additional galvanostatic charge/discharge results are presented in Appendix B.

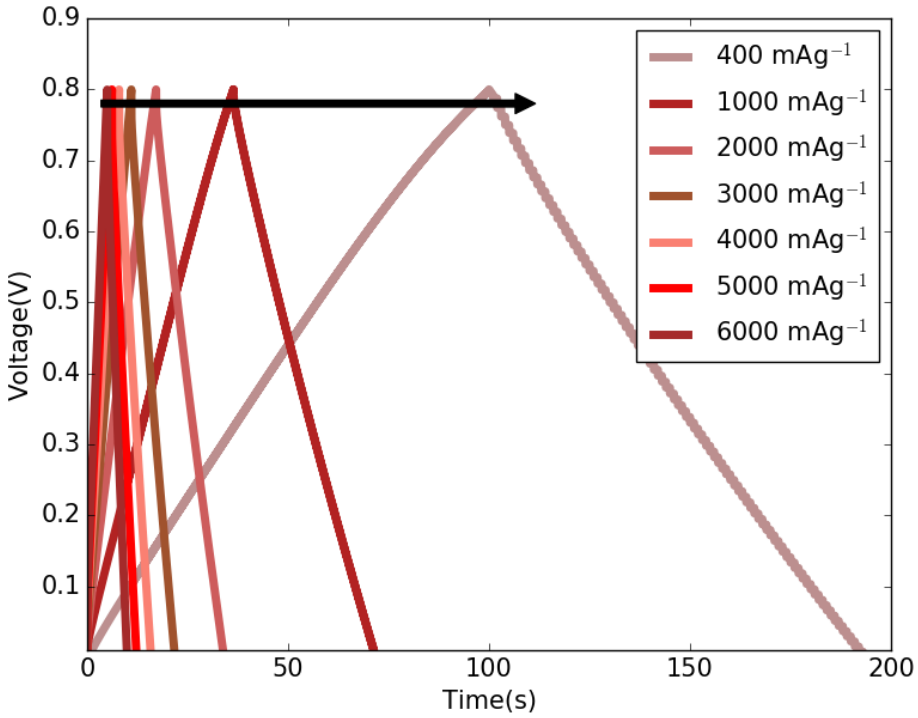

Figure 5.7: Galvanostatic charge/discharge curves of P-ECNFs(97/3) at current densities of (starting from the center and moving in the direction of the arrow) 6000, 5000, 4000, 3000, 2000, 1000, and 400 mA g^{-1}.

5.3.3 Cycle Life Testing

Cycle No.	ECNF(99/1)	P-ECNF(99/1)	P-ECNF(98/2)	P-ECNF(97/3)
1	100.0	100.0	100.0	100.0
100	101.3	100.3	101.0	100.6
1000	101.7	101.6	101.9	101.5
2000	100.3	100.3	100.2	100.2
3000	100.0	100.0	99.8	100.0
4000	99.4	99.4	98.5	98.2
5000	98.9	98.3	95.5	94.9
6000	98.7	97.4	93.5	91.1
7000	98.1	96.4	90.5	87.5
8000	97.8	95.7	87.1	83.0

Table 5.3: Capacitance of ECNF electrodes after cycling as a percentage of the capacitance measured on the first cycle.

Retention of high capacitance values over a long cycle life is an important property of supercapacitors. Galvanostatic discharge/charge from 0 to 0.8 V was performed on all fibres for 8000 cycles and, since capacitance is proportional to the slope of the trace during discharge, the capacitance at various cycles was measured relative to the capacitance calculated on the first cycle with results shown in Table 5.3. Fig 5.8 shows that all fibres maintain excellent cycling stability for the first 3000 cycles followed by a slow decrease in capacitance afterwards. P-ECNFs(97/3) retained 100% capacitance after 3000 cycles and 98.3%, 91.1% and 83.0% capacitance after 4000, 6000 and 8000 cycles respectively. The change in electrochemical performance of the fibres is apparent in the galvanostatic charge/discharge profiles at different cycle numbers with curves at higher cycle numbers appearing more horizontally compressed with a higher slope and showing a more pronounced IR drop (inset Fig 5.8). The less porous P-ECNFs(98/2) and P-ECNFs(99/1) maintained 87.1% and 95.7% capacitance after 8000 cycles respectively while the non porous ECNFs(99/1) maintained 97.8%. The decrease in specific capacitance

may be due to the loss of small amounts of electrode material which is a known occurrence in carbonaceous materials and may be exacerbated by nano and meso porosities which explains the larger capacitance decrease in the more porous fibres [102]. The small increase in specific capacitance on the 1000^{th} cycle may be due to the liquid electrolyte taking time to slowly penetrate into all of the pores of the fibres during the charge discharge process. This is otherwise known as the wetting effect.

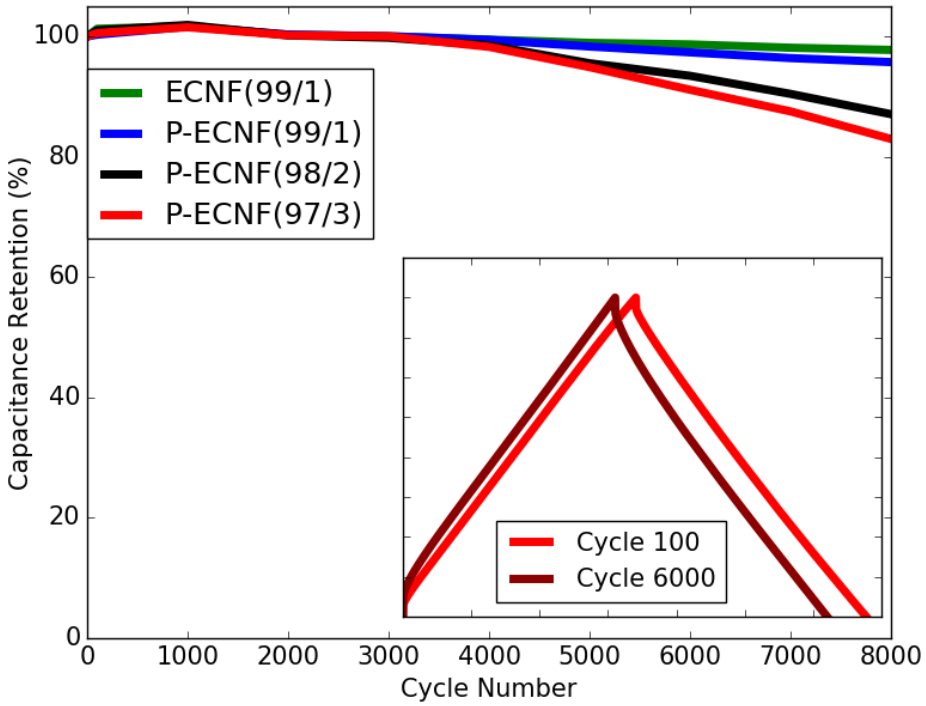

Figure 5.8: Cyclic stability of P-ECNFs and ECNFs(99/1) after 8000 cycles in 6M KOH. The inset shows the change in the galvanostatic charge/discharge profile of P-ECNFs(97/3) after 6000 cycles.

5.3.4 Electrical Impedance Spectroscopy

Electrical Impedance Spectroscopy (EIS) is a powerful analysis tool that be used to elucidate the charge transfer and resistance properties of electrode materials. In EIS, a sinusoidal AC current is applied to the capacitor and the resultant voltage is measured. From this, the frequency dependant impedance can be calculated based on the following equation:

$$Z_w = \frac{E_w}{I_w} \tag{5.3}$$

where E_w and I_w are the frequency dependant voltage and current respectively. In a supercapacitor, the measured voltage will be a function of both the resistive behaviour of the system and the capacitative behaviour of the system and will follow the following relationship:

$$E_w = IR - jX_c I \tag{5.4}$$

where R is the series resistance of the capacitor and X_c is the capacitative reactance of the system. It should be clear then that the impedance of the system can be broken into a real part (Z') which dominates at low frequencies and reflects the series resistance behaviour of the system, and imaginary part (Z"), which dominates at high frequencies and reflects the capacitative behaviour of the system. By measuring the potential as a function of current in a range of frequencies and by plotting the imaginary impedance as a function of the real impedance, a Nyquist plot can be prepared from which important information about the system can be inferred.

The Nyquist plots for the prepared nanofibres are presented in Fig 5.9. Each

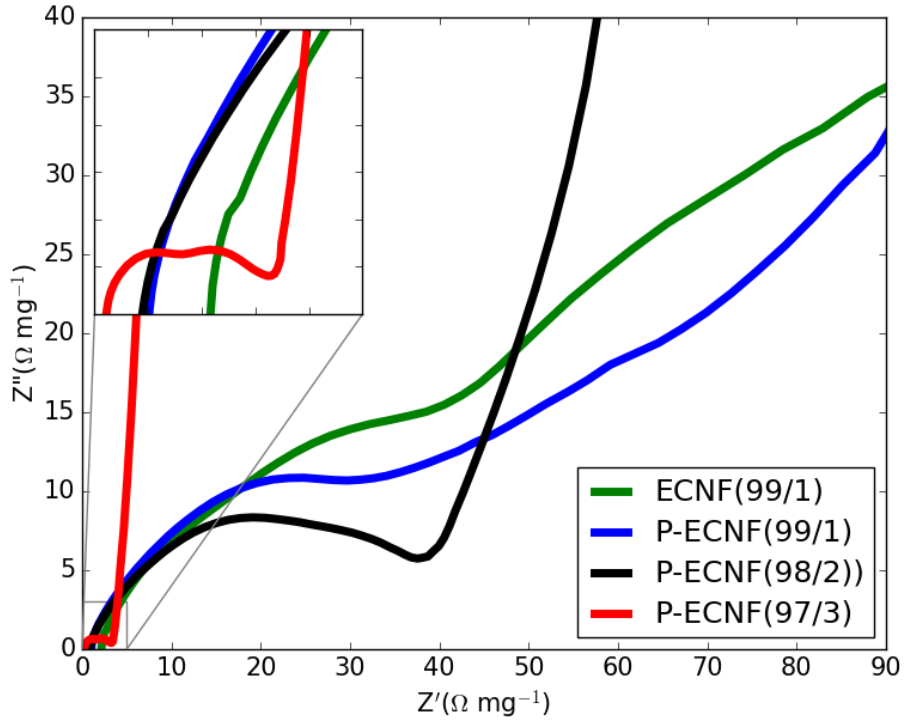

Figure 5.9: Nyquist plots from EIS analyses of ECNFs(99/1) and P-ECNFs.

of the curves show a distinct semicircle in the high frequency range followed by a linear portion in the low frequency range. The intersection of the curve with the x axis in the high frequency range gives an indication of the electrolyte resistance as well as the square of the resistance of the samples in the cell. All four samples cross the x-axis close to the origin with P-ECNFs(97/3) appearing to have the lowest sample and electrolyte resistance (having an x-intercept of 0.22) and with there being a trend of decreasing sample/electrolyte resistance as porosity increases. P-ECNFs(98/2), P-ECNFs(99/1) and ECNFs(99/1) had x-intercepts of 0.89, 1.02 and 2.17 respectively. The semicircular region of the plot corresponds to the charge transfer resistance, with smaller semicircle diameters indicating a

higher migration rate of ions at the electrolyte/electrode interface. The data reveals a trend of increasing semicircle diameter as the porosity of the fibres decreases with P-ECNFs(97/3) having a significantly smaller diameter and therefore, a much smaller charge transfer resistance than the other fibres. ECNFs(99/1) appear to exhibit the highest charge transfer resistance with the EIS curve displaying a large semi-circle diameter. In the lower frequency region, the finite slope of the samples gives an indication of the diffuse resistivity of the electrolyte within the electrode pores [108]. The more vertical slope of the P-ECNFs(97/3) line, which approaches the vertical line expected from an ideal capacitor, is an indication of the more desirable ion accessibility within the electrode compared to the other fibres.

The above electrochemical tests suggest that porous lignin-based carbon nanofibre electrodes are well suited to applications in supercapacitors and energy storage devices in general. P-ECNFs(97/3) in particular had high gravimetric capacitance, long cycle life and good cell resistance characteristics. These electrodes displayed strong reversible supercapacitor behaviour, with CV traces appearing rectangular and with limited IR drop apparent on the galvanostatic charge/discharge traces.

Chapter 6

Discussion

6.1 Structural Suitability of Porous Nanofibre Mats

The suitability of materials for applications in electrodes for energy storage devices is dependant on a number of factors. Among these factors, high performance electrodes for applications in devices like supercapacitors and lithium sulfur batteries require high surface area, high micro and mesoporosity, good electrical conductance and strong physical resilience. The prepared electrodes have demonstrated acceptable physical resilience and can be manipulated during supercapacitor fabrication without showing signs of breaking or cracking. They can be used as free-standing electrodes without the addition of binding agents which are often a necessity for many other carbon based electrode materials. This property is highly desirable because it contributes to a high specific capacity and simplifies the fabrication process. The free-standing nature of the prepared electrodes make them highly suitable for applications in energy storage devices.

In order to further analyze the suitability of lignin-based and porous carbon nanofibre mats for use in high performance energy storage devices, the conductivities of the prepared fibres are considered. As mentioned previously, it has been demonstrated that the performance of double layer capacitors is heavily influenced

by the conductivity of the materials with which the electrode is prepared [109]. Additionally, electrodes with high conductivities perform better in battery applications by reducing internal cell resistance. For these reasons, electrode materials with high conductivities are very attractive. After spending time optimizing the carbonization conditions, porous and non porous fibres were prepared that boasted impressive conductivities, with P-ECNFs having conductivities in the range of 18-20 S cm^{-1}.

Fibre Type	**Conductivity (S cm^{-1})**
ECNFs(99/1)	$7.31(s.d. = 0.65)$
P-ECNFs(99/1)	$19.69(s.d. = 1.02)$
P-ECNFs(98/2)	$18.91(s.d. = 0.62)$
P-ECNFs(97/3)	$18.39(s.d. = 0.92)$
PAN[109]	4.9
Porous Nafion:PAN 60:40[61]	0.13
Porous Fe_3O_4/PAN[110]	0.0004762
Lignin:PVA (85:15)[111]	16.03
30%F_4 Lignin[112]	5
30%F_4F_{1-3} Lignin (900°C)[112]	30
30%F_4F_{1-3} Lignin (1000°C)[112]	55
35%F_4SKL/PEO Lignin[93]	$2-5$

Table 6.1: Conductivity of different carbon nanofibres as reported in the literature.

The results of conductivity testing indicate that P-ECNFs are between three and four times more conductive than conventional non-porous PAN based ECNFs (4.9 S cm^{-1}) [103] and much more highly conductive than porous PAN based fibres. Table 6.1 presents the reported conductivities of a number of other comparable nanofibre-based electrodes as reported in the literature. It is interesting to note that in general, the reported conductivity values of porous PAN based nanofibres are much lower than that of non porous PAN based fibres. This is not the case for the fibres presented in this work. The high conductivity of the prepared fibres

relative to commonly used nanofibre materials indicates that lignin-based porous nanofibre mats are indeed a highly promising option for developing high performance electrodes for energy storage devices. It is more difficult to make a direct comparison to other lignin based carbon nanofibre electrodes presented in the literature due to the variability in types, purity and origins of different lignins. The prepared P-ECNFs did appear to have comparable conductivities to non porous lignin based nanofibrous electrodes and the conductivity of the fibre mats presented in this work fell in the mid range of reported values for lignin based nanofibre mats. A review of the literature did not find any reported conductivity values for porous and lignin-based carbon nanofibres. As a platform for the further development of energy storage electrodes, the proposed system has significant room for further increases in conductivity. The simplicity of the electrospinning process makes the addition of additional conductivity increasing nanoparticles and conductive agents possible. Commercial energy storage devices based on the proposed platform may take advantage of a wide range of additional doping agents.

As well as having a high conductivity, a high surface area can positively influence the capacitance of supercapacitor electrodes and can provide more conductive carbon to interface with the active materials in battery applications, thereby increasing active material loading. One of the goals of this research was to develop a method for introducing increased surface area into electrospun carbon nanofibre electrodes. This was achieved by creating porous nanofibres with tuneable porosity via a hydrothermal PEO removal step. Using this process, prepared P-ECNFs(97/3) achieved a specific surface area of $1258\,m^2\,g^{-1}$ and a total pore volume of $0.65\,cm^3\,g^{-1}$. A review of the literature reveals that the achieved specific surface area represents a 4-fold improvement over non porous PAN based CNFs

[53]. P-ECNFs(97/3) perform well when compared to other porous non-lignin based electrode materials despite falling short of the values of over 2000 $m^2\ g^{-1}$ for some PAN based electrode materials [60]. When compared to other Lignin-based nanofibrous electrodes, P-ECNFs have a high specific surface area (Table 6.2).

Fibre Type	**Specific Surface Area ($m^2\ g^{-1}$)**
ECNF(99/1)	816
P-ECNF(99/1)	974
P-ECNF(98/2)	1076
P-ECNF(97/3)	1258
PAN/PHMS[53]	302.50
PAN/PMMA/TEOS[57]	699
PAN/PVA[62]	1232
PAN/Nafion[61]	1600
PAN/PMMA[60]	2419
Lignin[113]	456
Lignin/PVA[102]	583
Alcell Lignin[114]	1195

Table 6.2: Specific surface area of different carbon nanofibres as reported in the literature.

Table 6.3 presents some specific surface areas typical of other common carbon materials for electrode applications that are not carbon nanofibres. P-ECNFs(97/3) have a specific surface area that falls in the midrange of these values, an impressive achievement for carbon nanofibre based electrodes which, traditionally have suffered from relatively low specific surface areas. High surface area of electrode components materials is important in as far as it contributes to the capacitance of the electrode. From this point of view, P-ECNFs(97/3) stand out from comparable electrode materials due to their high capacitance. Additionally, a high specific surface area may be attractive because it provides more interface for the addition of performance enhancing additives and active materials, particularly in battery applications. For this reason, the high specific surface area of P-ECNFs(97/3) make the

prepared electrodes suitable as a platform for enhanced future electrodes for both supercapacitors and batteries.

Fibre Type	**Specific Surface Area ($m^2\,g^{-1}$)**
Activated Carbon	1000 – 3500
Functionalized Porous Carbons	300 – 2200
Particulate Carbon from SiC/TiC	100 – 120
Carbon Nanotubes	150 – 500
Templated Porous Carbons	500 – 3000
Activated Carbon fibres	1000 – 3000
Carbon Cloth	2500
Carbon Aerogels	400 – 1000

Table 6.3: Specific surface area of different carbon materials as reported in the literature. Table adapted from ref [115].

Importantly, the prepared electrodes exhibit high porosity compared to non porous carbon nanofibre electrodes. One of the major contributions of this work is the development of a process by which both micro and mesoporosity can be introduced into electrospun fibres in a controllable fashion. Recently, high profile works have indicated that mesoporous carbons may be the most promising material for high performance Li-S batteries [116, 117]. The prepared mesoporous ECNFs have a total pore volume that compares favourably to values reported in the literature for other mesoporous carbon nanofibres (Table 6.4) and therefore, with their high conductivity in mind, may be suitable for applications in Li-S batteries.

The hydrothermal treatment process has been demonstrated as a simple method of producing micro and mesoporosities in lignin-based carbon nanofibres. Analysis of results from SEM imaging, conductivity testing, XRD and Raman analysis and TGA reveal electrode mats that are conducive to being used in both supercapacitor and battery applications. As discussed earlier, Kraft lignin is a strongly suitable material for energy storage applications due to its low cost, sustainabil-

Fibre Type	Pore Volume ($cm^3\,g^{-1}$)
ECNF(99/1)	0.42
P-ECNF(99/1)	0.49
P-ECNF(98/2)	0.52
P-ECNF(97/3)	0.65
PVP/TEOS[118]	$0.65 - 1.02$
PVA/Tin[119]	$0.37 - 0.60$
PAN/TiO_2[120]	0.095-0.225

Table 6.4: Pore Volume of different mesoporous carbon nanofibres as reported in the literature.

ity and natural abundance. Therefore, the ability to develop free standing, highly porous, highly conductive fibres with competitive surface area from this material for applications in energy storage devices is significant and could contribute to the next generation of high performance energy storage devices including supercapacitors and Li-S batteries.

6.2 Electrochemical Suitability of ECNF Mats for Supercapacitor Applications

While the structural and morphological properties of the prepared electrodes make them attractive for applications in energy storage devices, the electrochemical properties of this work should be discussed in the context of electrode material research in general in order to determine to merit of the method and materials presented. The electrochemical performance of the electrodes was tested by constructing supercapacitor devices and subjecting them to CV, galvanostatic charge/discharge and EIS testing. CV testing revealed a maximum specific capacitance of $112\,F\,g^{-1}$ for P-ECNFs(97/3) at a voltage scan rate of $5\,mV\,s^{-1}$. This is an improvement over other similar electrode materials such as activated lignin derived mesoporous carbon ($102.3\,F\,g^{-1}$) [121] and non porous lignin and polyvinyl alcohol based nanofi-

bres ($64\,\mathrm{F\,g^{-1}}$) [102]. Table 6.5 compares measured capacitance values with other electrode materials reported in the literature.

Material	**Capacitance ($\mathrm{F\,g^{-1}}$)**
ECNF(99/1)	78
P-ECNF(99/1)	89
P-ECNF(98/2)	102
P-ECNF(97/3)	112
Activated Carbon	< 100
Functionalized Porous Carbons	$100 - 150$
Particulate Carbon from SiC/TiC	$100 - 120$
Carbon Nanotubes	< 60
Templated Porous Carbons	$60 - 140$
Activated Carbon fibres	$80 - 200$
Carbon Cloth	$40 - 80$
Carbon Aerogels	< 80

Table 6.5: Specific capacitance of various carbon materials measured in aqueous electrolytes as reported in the literature. Table adapted from ref [115].

P-ECNFs(97/3) exhibit a good specific capacitance relative to other carbon based electrode materials at a voltage scan rate of $5\,\mathrm{mV\,s^{-1}}$ meaning porous lignin-based ECNFs are highly suitable for use in supercapacitors. Equally as important, P-ECNFs(97/3) have promising specific capacitance at high scan rates ($95\,\mathrm{F\,g^{-1}}$ at a scan rate of $50\,\mathrm{mV\,s^{-1}}$) and even maintain 71.1% capacitance at rates of $200\,\mathrm{mV\,s^{-1}}$. Even at this high scan rate, the measured capacitance exceeds that of many different carbon materials and highlights the suitability of this material for supercapacitors that demand high charge and discharge rates. On the other hand, the measured volumetric capacitance of the prepared fibres may not be as competitive. The best result of $35\,\mathrm{F\,cm^{-3}}$ again was achieved for P-ECNFs(97/3) at a scan rate of $5\,\mathrm{mV\,s^{-1}}$ which falls below the volumetric capacitance values reported for some other carbon based electrode materials (Table 6.6). The large spaces in be-

tween the fibres contribute to a low density which is common in carbon nanofibre electrodes and generally leads to a low volumetric capacitance in these types of electrode materials compared to more dense materials.

Material	**Capacitance (F cm^{-3})**
ECNF(99/1)	35
P-ECNF(99/1)	31
P-ECNF(98/2)	23
P-ECNF(97/3)	18
Activated Carbon	$19-611$
Mesoporous Carbons	<436
Graphene	$30-488$
Carbon Nanotubes	$11-132$
Carbide Derived Carbon	$75-180$

Table 6.6: Volumetric capacitance of various carbon materials measured in aqueous electrolytes as reported in the literature. Values taken from ref [122].

Despite the relatively low volumetric capacitance of the fibres, he rectangular profile of the CV trace for all scan rates indicates good reversible supercapacitor performance, especially for P-ECNFs(97/3). This behaviour is substantiated by the EIS results which suggest low sample and electrolyte resistance, low charge transfer resistance and good ion accessibility within the electrodes. In addition to improving the performance of these electrodes in supercapacitor applications, these properties are highly desirable for battery applications as well.

Finally, and in addition to high specific capacitance, the prepared P-ECNF electrodes exhibit very good cycle stability based on galvanostatic charge/discharge testing. In particular, ECNFs(99/1) retained 97.8% capacitance after 8000 cycles. Even P-ECNFs(97/3), which displayed the worse cycling stability of the four prepared fibre types retained 100% capacitance after 3000 cycles, 91.1% after 6000 cycles and 83% capacitance after 8000 cycles. This result is a significant improve-

ment on other lignin based carbon nanofibre electrode materials which maintained 90% capacitance after 6000 cycles [102], and on non lignin based porous carbon nanofibre electrode materials which maintained 94% capacitance but after only 2000 cycles [55]. The combination of high cycle life and excellent specific capacitance, coupled with the low charge transfer resistance and good ion accessibility in the electrodes make the prepared fibres, and especially P-ECNFs(97/3) highly suitable for use in supercapacitor applications and give a good indication of promising potential use in battery applications.

6.3 Commercial Considerations

With promising structural and electrochemical properties having been demonstrated, an analysis of the cost of the proposed system should be undertaken to help understand it's longer term commercial viability. As previously mentioned, today's commercial supercapacitor devices usually use activated carbons derived from coconut husks and can provide about 350 F for a mid-size device. Typical cost for the electrode material for such a device was calculated in section 3.2 to be around \$0.19 USD. With a capacitance of $112\,\mathrm{F\,g^{-1}}$, an equivalent mid-size commercial device would require about 1.56 g of ECNFs. For P-ECNFs(97/3), this translates to 1.51 g of lignin and 0.05g of PEO. A good estimate of the cost of producing lignin based carbon fibers is around \$6.3 USD/kg [123] and PEO costs approximately \$1.5 USD/kg. This equates to a total cost of electrode material of 1.92 cents for a typical device utilizing P-ECNFs(97/3) and a reduction in cost by a factor of about 10 compared to commercial supercapacitors. While the costs of assembling devices have not been considered in this analysis, it appears that the high electrochemical performance, low material cost and absence of additives in

the proposed electrodes may contribute to a significant reduction in cost for supercapacitors utilizing this system compared to commercial capacitors.

Chapter 7

Conclusions and Recommendations

7.1 Porous Lignin-based Nanofibrous Electrodes for Energy Storage Devices

In this study, high performance electrodes were prepared from porous carbon nanofibres for applications in energy storage devices. Porous carbon nanofibres were fabricated using a highly scalable process involving electrospinning of a low-cost, naturally abundant and sustainable Kraft lignin precursor followed by a facile hydrothermal treatment step and a heat treatment step including carbonization at high temperature. Four different fibre types where prepared, each containing different ratios of lignin to PEO in their precursor solutions. These fibre types were labeled as ECNFs(99/1), P-ECNFs(99/1), P-ECNFs(98/2) and P-ECNFs(97/3). The prepared electrodes were used to assemble supacapacitor devices in a lab designed testing cell with 6M KOH as the electrolyte. Supercapacitors utilizing electrodes prepared from precursor lignin solution containing 97% lignin and 3% PEO (P-ECNFs(97/3)) exhibited the highest gravimetric capacitance of $112\,\mathrm{F\,g^{-1}}$ at a scan rate of $5\,\mathrm{mV\,s^{-1}}$.

Initially, stabilization and carbonization parameters were optimized in order to maximize conductivity of carbon nanofibres. The optimized heat treatment condi-

tions were found to be 2 hours of stabilization at a temperature of 250°C followed by a ramping phase at $2°C\,min^{-1}$ to a carbonization temperature of 900°C for 2 hours. These parameters were used throughout the rest of this work. The morphology and structure of the prepared fibres was first observed from SEM images which revealed well-formed fibres featuring varying degrees of porosity depending on the ratio of lignin to PEO in the precursor solution which was used to make them. Porosity appeared well distributed in the fibres. Fibre diameter was relatively consistent, falling in the range of 428-469 nm for all fibre types, however fibre morphology differed slightly between the fibre types, with those fibres containing more precursor PEO having a more fluid and less rigid appearance and comprising more fusion points between adjacent fibres. TGA was employed to verify the content of the prepared fibres and to confirm the effectiveness of the hydrothermal treatment step at removing PEO from the fibres prior to carbonization. It was found that, while the hydrothermal treatment was indeed effective at removing PEO located on or near the surface of the fibres, some PEO remained in the fibres, even after the washing step was completed and that the relative amount of PEO remaining correlated with the proportion of PEO in the precursor solution. The TGA results confirmed the expectation that the washing step would only be able to remove the PEO that was located at the surface of the fibres.

Because high surface area and porosity in electrodes may be crucial for their success in energy storage devices, surface area and porosity were examined using nitrogen adsorption porosimetry. The BET method revealed that P-ECNFs(97/3) had a very high surface area of $1258\,m^2\,g^{-1}$ which represents a 5-fold improvement over comparable but non-porous carbon nanofibres based on PAN [53] and a 54% increase in surface area compared to the non porous ECNFs(99/1), which

have a specific surface area of $816\,m^2\,g^{-1}$. This dramatic increase in surface area demonstrates the effectiveness of the proposed hydrothermal treatment step during fabrication at increasing the surface area of the fibres and makes the surface area of the prepared fibres competitive with other high surface area carbon materials commonly used in electrode fabrication. Additionally, the density functional theory (DFT) model was used to measure pore size distribution in all fibres and revealed high mesoporosity in the porous fibres compared with the non porous fibres, especially in P-ECNFs(97/3) which contained high pore volume, particularly for pores in the range of 40-80 nm.

Conductivity of the prepared fibres was measured using a two point probe method with results indicating high conductivity for the porous fibres. P-ECNFs(99/1) had the highest conductivity ($19.69\,S\,cm^{-1}$), almost a 3-fold improvement on the non-porous ECNFs(99/1). This high conductivity means that porous carbon nanofibres prepared from lignin can achieve a conductivity that is four times higher than for conventional PAN based nanofibres. Both XRD and Raman spectroscopy where conducted on the fibres in order to elucidate the molecular and crystal structures of the fibres. XRD analysis revealed strong peaks around 22 and 44, which were found to correspond to graphitic structures. As expected, the height of these peaks correlated well with the conductivity of the fibres, indicating that graphitic structures within the fibres are contributing to the high conductivity of the fibres. Similarly, Raman spectroscopy results revealed that conductivity of fibres may be affected by the degree of graphitic order within the fibres and that PEO contained within the fibres during carbonization may disrupt the formation of well ordered graphitic structures.

Results of the structural and morphological characterization tests suggest promis-

ing suitability of porous lignin-based nanofibres for use in energy storage applications. Due to the free standing and binder free nature of the electrodes, their high conductivity and their high surface area and porosity, the prepared electrodes may be a promising material for use in next generation energy storage and in particular may be suitable for use in Li-S batteries and supercapacitors. Additionally, the proposed electrodes utilize low-cost, sustainable and naturally abundant precursor lignin as a carbon source and the fabrication process is both simple and highly scalable. Table 7.1 compares some of the performance parameters of the proposed electrodes with typical PAN based non-porous electrodes. In order to gage the performance of the proposed electrodes in energy storage applications, supercapacitor devices were developed in the lab and electrochemical testing was conducted on all fibre electrodes.

Parameter	**PAN**	**Lignin**
Conductivity ($S\,cm^{-1}$)	4.9 [103]	18.39
Specific Surface Area ($m^2\,g^{-1}$)	236.75 [53]	1258
Relative Cost	2 [90]	1
Sustainability	Low	High
Capacitance ($F\,g^{-1}$)	165 [124]	112

Table 7.1: Performance of porous and lignin-based nanofibrous electrodes compared to non porous PAN based electrodes.

Cyclic voltammetry testing was completed and CV traces were used to determine the specific capacitance of each of the prepared electrodes with P-ECNFs(97/3) having the highest gravimetric capacitance of $112\,F\,g^{-1}$ at a scan rate of $5\,mV\,s^{-1}$. This value represents an improvement over many other commonly used carbon materials reported in the literature. Even at high scan rates of $50\,mV\,s^{-1}$, P-ECNFs(97/3) had a high capacitance of $95\,F\,g^{-1}$ indicating that these electrodes could be suitable for energy storage devices with high rate capability and requiring

fast charge and discharge. Additionally, these fibres had very rectangular CV traces compared to other fibre electrodes which suggests strong reversible supercapacitor behaviour. The strong electrochemical performance of the fibres at high rates was attributed to better ionic accessibility and shorter diffusion distances within the electrodes. On the other hand, the fibres exhibited a relatively low volumetric capacitance which is common for carbon nanofiber based electrode materials. P-ECNFs(97/3) had the highest volumetric capacitance of $35\,\mathrm{F\,cm^{-3}}$.

Next, cycle stability was measured by way of galvanostatic charge/discharge testing. The results show that even after 3000 cycles, the prepared fibre electrodes maintained 100% of their initial capacity. After 6000 and 8000 cycles, P-ECNFs(97/3) maintained 91.1% and 83.0% capacitance respectively while ECNFs(99/1) maintained 98.7% and 97.8%. The higher cycle stability of the less porous fibres was attributed to lower rates of material loss which is a common occurrence in carbon materials and can be exacerbated by micro and mesoporosities. Lastly, EIS was performed on all fibres and indicated that P-ECNFs(97/3) had the lowest sample, electrolyte and charge transfer resistance of the four samples and that increasing porosity correlated well with a decrease in these resistances. EIS results confirmed also the desirable ion accessibility characteristics of the more porous fibres. Electrochemical testing of the prepared fibres reveal strong performance in supercapacitor applications and highlight the promising nature of lignin-based and porous carbon nanofibre electrodes as a platform for the development of other energy storage devices like Li-S batteries. Additionally, with an estimated cost about 10 times lower than that of today's commercial supercapacitors, the proposed electrodes could contribute to advancing energy storage technology in the renewable energy, the transportation and the consumer electronics industries.

7.2 Recommendations for Future Work

Additional optimization the proposed electrode materials and preparation methods will be required before porous and lignin-based carbon nanofibre electrodes can be scaled up for commercial purposes. Based on the results presented in this work, which revealed a strong relationship between porosity and surface area of the fibres and supercapacitor performance, the author suggests that further increasing surface area may allow the proposed electrode design to achieve even higher performance results. Increasing the PEO content of precursor electrospinning solutions may help to achieve this aim but difficulties relating to electrospinnability of high PEO content solutions will have to be addressed. Also, while this work has demonstrated how creating porosity in fibres can contribute to increasing surface area in the fibres, it remains to be seen whether porosity or fibre size is the dominating factor in determining surface area. An analysis of the importance of each of these factors would be useful.

In addition to increasing porosity and as a platform for further electrode development, the author suggests that conductivity of the electrodes can be further increased through the targeted addition of conductive agents and nanoparticles during the electrospinning process. Additionally, further testing should be completed to understand the behaviour of the proposed electrodes in other electrolyte systems including organic electrolytes. The behaviour of the system under these conditions would give additional information as to their potential applications in Li-S batteries and their battery systems.

One of the disadvantages of utilizing carbon nanofibers for electrodes is that the resulting materials end up being significantly less dense than some other common

carbon materials. This can result in a lower volumetric capacitance and indeed, the prepared fibres had relatively low volumetric capacitances. By improving the density of the system, improvements in volumetric capacitance could be made. Future efforts could be directed at "filling the gaps" between fibres with highly conductive and porous structures although care must be taken to maintain good ion accessibility in the fibres.

While increased electrochemical performance is always desired, the proposed electrodes perform well in this regard as-is. One of the flaws in the proposed material is the lack of flexibility in these electrodes which, could be caused by the introduced pores and defects in the surface of the fibres. An analysis should be done on the effect of these defects on the over all flexibility of the system to determine whether these defects contribute in any significant way to the low flexibility of the system. While flexibility may not be necessary for many applications, it is indeed highly sought after in applications like wearable and flexible electronics. The addition on additional nanomaterials may provide an avenue for achieving flexibility. For example, Iron nanoparticles have been shown to increase flexibility in similar carbon nanofibres and may, as an added benefit, increase the conductivity of the fibres and contribute to better electrochemical performance [112]. Increased flexibility of the fibres may also contribute to the physical resiliency of the proposed electrodes and may further contribute to the already promising cycling stability of these electrodes.

While the results in this work confirmed the suitability of the proposed electrodes for applications in supercapacitor electrodes, one of the motivations behind the development of these electrodes was the problems currently facing Lithium-Sulfur battery technology. Despite, the electrodes in this work being designed with

LiS batteries in mind, their suitability for this type of energy storage device remains to be confirmed. In particular, future work should look at the effect of porosity on the cycle life of Li-S cells to verify the effectiveness of increased porosity in carbon nanofibres at counteracting the negative effects of the shuttling effect that is commonly seen in Li-S batteries. Also, one weakness of carbon nanofibre based electrodes is the low density of the material. For Li-S battery applications, this may lead to underutilization of sulfur after addition of sulfur since large non-conductive pockets of sulfur would be able to form. Increasing the density of this material by adding more conductive and high surface area and porosity materials to fill the gaps between fibres is an idea that should be explored further.

Bibliography

[1] Fatih Birol. Key world energy statistics. Technical report, International Energy Agency, 2016.

[2] Seb Henbest. New energy outlook 2016. Technical report, Bloomberg, 2016.

[3] Tom Randall. Here's how electric cars will cause the next oil crisis, Retrieved: November 6th 2016. URL http://www.bloomberg.com/features/2016-ev-oil-crisis/.

[4] Sam Korus. Tesla's battery technology powers its moat – "faster than falling.", Retrieved: November 6th 2016. URL https://ark-invest.com/research/battery-technology.

[5] Anissa Dehamna. Energy storage for renewables integration: A burgeoning market, Retrieved: November 16th 2016. URL http://energystorage.org/news/esa-news/energy-storage-renewables-integration-burgeoning-market.

[6] Ingrid Lunden. 1b smartphone users globally by 2020. Technical report, TechCrunch, 2015.

[7] Peter Diamandis. The 'rising billion' new consumers will arrive by 2020, Retrieved: November 6th 2016. URL http://www.huffingtonpost.com/peter-diamandis/rising-billion-consumers_b_7008160.html.

[8] David Blaza. Kicking off #armwearableswk with an analysts view of the market, Retrieved: November 6th 2016. URL https://community.arm.com/groups/wearables/blog/2014/11/17/kicking-off-armwearableswk-with-an-analysts-view-of-the-market.

[9] K. H. LaCommare and J. H. Eto. Understanding the cost of power interruptions to u.s. electricity consumers. Technical report, Ernest Orlando Lawrence Berkeley National Laboratory, 2004.

[10] R. Van Noorden. The rechargeable revolution: A better battery. *Nature*, 507:26–28, 2014.

[11] The Freedonia Group. World batteries - demand and sales forecasts, market share, market size, market leaders. Technical report, 2015.

[12] K. Kordesch and W. Taucher-Mautner. History - primary batteries. In *Encyclopedia of Electrochemical Power Sources*, pages 555 – 564. Elsevier, 2009.

[13] Tkarcher, Retrieved: December 31st 2016. URL https://commons.wikimedia.org/wiki/File:Battery_with_polymer_separator.svg.

[14] P. Kurzweil. History - secondary batteries. In *Encyclopedia of*

Electrochemical Power Sources, pages 565–579. Elsevier, 2009.

[15] European Union (L 266). Directive 2006/66/ec of the european parliament and of the council of the 6th of september 2006 on batteries and accumulators and repealing directive 91/157/eec. *Official Journal of the European Union*, 2006.

[16] A. Yoshino, K. Sanechika, and T. Nakajima. Secondary battery, May 1987. US Patent 4,668,595.

[17] Sony. Keywords to understanding sony energy devices, Retrieved: October 8th 2016. URL http://www.sonyenergy-devices.co.jp/en/keyword/.

[18] A. I. Stan, M. Świerczyński, D. I. Stroe, R. Teodorescu, and S. J. Andreasen. Lithium ion battery chemistries from renewable energy storage to automotive and back-up power applications; an overview. In *2014 International Conference on Optimization of Electrical and Electronic Equipment (OPTIM)*, pages 713–720, 2014.

[19] B. J. Landi, M. J. Ganter, C. D. Cress, R. A. DiLeo, and R. P. Raffaelle. Carbon nanotubes for lithium ion batteries. *Energy Environ. Sci.*, 2: 638–654, 2009.

[20] US Energy Department. Energy department to launch new energy innovation hub focused on advanced batteries and energy storage, Retrieved: October 16th 2016. URL http://energy.gov/articles/energy-department-launch-new-energy-innovation-hub-focused-advanced-batteries-and-energy.

[21] K. M. Abraham and Z. Jiang. A polymer electrolyte based rechargeable lithium/oxygen battery. *Journal of The Electrochemical Society*, 143(1): 1–5, 1996.

[22] Jeremy Neubauer. Analysis of electric vehicle battery performance targets, Retrieved: November 16th 2016. URL http://energy.gov/sites/prod/files/2014/03/f13/es174_neubauer_2013_o.pdf.

[23] K. Kumaresan, Y. Mikhaylik, and R. E. White. A mathematical model for a lithium–sulfur cell. *Journal of The Electrochemical Society*, 155(8): A576–A582, 2008.

[24] S. Cheon, K. Ko, J. Cho, S. Kim, E. Chin, and H. Kim. Rechargeable lithium sulfur battery: I. structural change of sulfur cathode during discharge and charge. *Journal of The Electrochemical Society*, 150(6): A796–A799, 2003.

[25] J. Hassoun and B. Scrosati. A high-performance polymer tin sulfur lithium ion battery. *Angewandte Chemie International Edition*, 49(13):2371–2374, 2010.

[26] Gaoran Li, Zhoupeng Li, Bin Zhang, and Zhan Lin. Developments of electrolyte systems for lithium–sulfur batteries: A review. *Frontiers in Energy Research*, 3:5, 2015.

[27] N. Angulakshmi and A. M.Stephan. Efficient electrolytes for lithium-sulfur batteries. *Frontiers in Energy Research*, 3(17):1–8, 2015.

[28] R. Singhal, S. Chung, A. Manthiram, and V. Kalra. A free-standing carbon nanofiber interlayer for high-performance lithium-sulfur batteries. *J. Mater. Chem. A*, 3:4530–4538, 2015.

[29] S. Lee, Y. J. Lee, and Y. Sun. Nanostructured lithium sulfide materials for lithium-sulfur batteries. *Journal of Power Sources*, 323:174 – 188, 2016.

[30] A. Perujo, G. V. Grootveld, and H. Scholz. *New Generation Of Electric Vehicles*. Intech, 2012. URL http://www.intechopen.com/books/new-generation-of-electric-vehicles/present-and-future-role-of-battery-electrical-vehicles-in-private-and-public-urban-transport.

[31] CantecSystems. A brief history of supercapacitors. Technical report, Batteries and Energy Storage Technology, 2007.

[32] R.P.Deshpande. *Ultracapacitors*. McGraw-Hill Education, 2014.

[33] J. G. Zhu. Supercapacitors. Technical report, University of Technology, Sydney, 2016.

[34] B. E. Conway. Transition from "supercapacitor" to "battery" behavior in electrochemical energy storage. *Journal of The Electrochemical Society*, 138(6):1539–1548, 1991.

[35] Jordan Hanania, Braden Heffernan, James Jenden, Ryan Leeson, and Jason Donev. Supercapacitor, Retrieved: October 5th 2016. URL http://energyeducation.ca/encyclopedia/Supercapacitor.

[36] Amrita Jain and S.K. Tripathi. Fabrication and characterization of energy storing supercapacitor devices using coconut shell based activated charcoal electrode. *Materials Science and Engineering: B*, 183:54 – 60, 2014.

[37] T. Chen and L. Dai. Carbon nanomaterials for high-performance supercapacitors. *Materials Today*, 16(7–8):272 – 280, 2013.

[38] V. Obreja, A. Dinescu, and A.C. Obreja. Activated carbon based electrodes in commercial supercapacitors and their performance. *International Review of Electrical Engineering*, 5(1):272–282, 2010.

[39] L. Weinstein and R. Dash. Supercapacitor carbons. *Materials Today*, 16 (10):356–357, 2013.

[40] PlasticsNews. Current resin pricing, Retrieved: January 2nd 2017. URL http://www.plasticsnews.com/resin/high-temperature-thermoplastics/current-pricing.

[41] SidRichardson. Carbon black pricing, Retrieved: January 2nd 2017. URL http: //www.sidrich.com/products-and-pricing/pricing/carbon-black-pricing/.

[42] B. Zhang, X. Qin, G. R. Li, and X. P. Gao. Enhancement of long stability of sulfur cathode by encapsulating sulfur into micropores of carbon

spheres. *Energy Environ. Sci.*, 3:1531–1537, 2010.

[43] X. Li, Y. Cao, W. Qi, L. V. Saraf, Z. Xiao, J.and Nie, J. Mietek, J. Zhang, B. Schwenzer, and J. Liu. Optimization of mesoporous carbon structures for lithium-sulfur battery applications. *J. Mater. Chem.*, 21:16603–16610, 2011.

[44] Y. Su, Y. Fu, and A. Manthiram. Self-weaving sulfur-carbon composite cathodes for high rate lithium-sulfur batteries. *Phys. Chem. Chem. Phys.*, 14:14495–14499, 2012.

[45] H. Wang, Y. Yang, Y. Liang, J. T. Robinson, Y. Li, Y. Jackson, A.and Cui, and H. Dai. Graphene-wrapped sulfur particles as a rechargeable lithium–sulfur battery cathode material with high capacity and cycling stability. *Nano Letters*, 11(7):2644–2647, 2011.

[46] A. Manthiram, Y. Fu, S. Chung, C. Zu, and Y. Su. Rechargeable lithium sulfur batteries. *Chemical Reviews*, 114:11751–11787, 2014.

[47] Y. Zhu, S. Murali, M. D. Stoller, K. J. Ganesh, W. Cai, P. J. Ferreira, A. Pirkle, R. M. Wallace, K. A. Cychosz, M. Thommes, D. Su, E. A. Stach, and R. S. Ruoff. Carbon-based supercapacitors produced by activation of graphene. *Science*, 332(6037):1537–1541, 2011.

[48] E. Frackowiak, K. Jurewicz, S. Delpeux, and F. Béguin. Nanotubular materials for supercapacitors. *Journal of Power Sources*, 97–98:822 – 825, 2001.

[49] R. R. Mitchell, B. M. Gallant, C. V. Thompson, and Y. Shao-Horn. All-carbon-nanofiber electrodes for high-energy rechargeable li-o2 batteries. *Energy Environ. Sci.*, 4:2952–2958, 2011.

[50] Q. Li, Z. Zhang, Z. Guo, Y. Lai, K. Zhang, and J. Li. Improved cyclability of lithium–sulfur battery cathode using encapsulated sulfur in hollow carbon nanofiber@nitrogen-doped porous carbon core–shell composite. *Carbon*, 78:1 – 9, 2014.

[51] M. Rao, X. Song, and E. J. Cairns. Nano-carbon/sulfur composite cathode materials with carbon nanofiber as electrical conductor for advanced secondary lithium/sulfur cells. *Journal of Power Sources*, 205:474 – 478, 2012.

[52] K. Jung, W. Deng, D. W. Smith Jr., and J. P. Ferraris. Carbon nanofiber electrodes for supercapacitors derived from new precursor polymer: Poly(acrylonitrile-co-vinylimidazole). *Electrochemistry Communications*, 23:149 – 152, 2012.

[53] B. Kim, K. S. Yang, H. Woo, and K. Oshida. Supercapacitor performance of porous carbon nanofiber composites prepared by electrospinning polymethylhydrosiloxane (pmhs)/polyacrylonitrile (pan) blend solutions. *Synthetic Metals*, 161(13–14):1211 – 1216, 2011.

[54] A. Peigney, C. Laurent, E. Flahaut, R.R. Bacsa, and A. Rousset. Specific surface area of carbon nanotubes and bundles of carbon nanotubes. *Carbon*, 39(4):507 – 514, 2001.

[55] Y.Liu, J. Zhou, L. Chen, P. Zhang, W. Fu, H. Zhao, Y. Ma, X. Pan, Z. Zhang, W. Han, and E. Xie. Highly flexible freestanding porous carbon nanofibers for electrodes materials of high-performance all-carbon supercapacitors. *ACS Applied Materials & Interfaces*, 7(42):23515–23520, 2015.

[56] T. Wang, P. Shi, J. Chen, S. Cheng, and H. Xiang. Effects of porous structure of carbon hosts on preparation and electrochemical performance of sulfur/carbon composites for lithium–sulfur batteries. *Journal of Nanoparticle Research*, 18(1):19, 2016.

[57] Q. Wang, Q. Cao, X. Wang, B. Jing, H. Kuang, and L. Zhou. Dual template method to prepare hierarchical porous carbon nanofibers for high-power supercapacitors. *Journal of Solid State Electrochemistry*, 17(10): 2731–2739, 2013.

[58] H. He, L. Shi, Y. Fang, X. Li, Q. Song, and L. Zhi. Mass production of multi-channeled porous carbon nanofibers and their application as binder-free electrodes for high-performance supercapacitors. *Small*, 10 (22):4671–4676, 2014.

[59] E. Jo, J. Yeo, D. Kim, J. S. Oh, and C. K. Hong. Preparation of well-controlled porous carbon nanofiber materials by varying the compatibility of polymer blends. *Polymer International*, 63(8):1471–1477, 2014.

[60] N.C. Abeykoon, J. S. Bonso, and J. P. Ferraris. Supercapacitor performance of carbon nanofiber electrodes derived from immiscible pan/pmma polymer blends. *RSC Advances*, 5(26):19865–19873, 2015.

[61] C. Tran and V. Kalra. Fabrication of porous carbon nanofibers with adjustable pore sizes as electrodes for supercapacitors. *Journal of Power Sources*, 235:289 – 296, 2013.

[62] G. Wang, B. Qian, Y. Wang, F. Dong, Q.and Zhan, and J. Qiu. Electrospun porous hierarchical carbon nanofibers with tailored structures for supercapacitors and capacitive deionization. *New J. Chem.*, 40:3786–3792, 2016.

[63] L. Ji, M. Rao, S. Aloni, L. Wang, E. J. Cairns, and Y. Zhang. Porous carbon nanofiber–sulfur composite electrodes for lithium/sulfur cells. *Energy Environ. Sci.*, 4:5053–5059, 2011.

[64] L. Zhou, X. Lin, T.Huang, and A. Yu. Nitrogen-doped porous carbon nanofiber webs/sulfur composites as cathode materials for lithium-sulfur batteries. *Electrochimica Acta*, 116:210 – 216, 2014.

[65] S.K. Chakarvarti and J. Vetter. Template synthesis—a membrane based technology for generation of nano-/micro materials: a review1. *Radiation Measurements*, 29(2):149 – 159, 1998.

[66] P. van de Witte, P.J. Dijkstra, J.W.A. van den Berg, and J. Feijen. Phase separation processes in polymer solutions in relation to membrane formation. *Journal of Membrane Science*, 117(1):1 – 31, 1996.

[67] W. E. Teo and S. Ramakrishna. A review on electrospinning design and nanofibre assemblies. *Nanotechnology*, 17(14):R89, 2006.

[68] Z. Huang, Y. Z. Zhang, M. Kotaki, and S. Ramakrishna. A review on polymer nanofibers by electrospinning and their applications in nanocomposites. *Composites Science and Technology*, 63(15):2223 – 2253, 2003.

[69] J. Doshi and D. H. Reneker. Electrospinning process and applications of electrospun fibers. *Journal of Electrostatics*, 35(2):151 – 160, 1995.

[70] R. Pignatello, editor. *Advances in Biomaterials Science and Biomedical Applications*. InTech, 2013.

[71] D. Li and Y. Xia. Electrospinning of nanofibers: Reinventing the wheel? *Advanced Materials*, 16(14):1151–1170, 2004.

[72] By Joanna Gatford, Retrieved: December 31st 2016. URL https://commons.wikimedia.org/wiki/File:Electrospinning_Diagram.jpg.

[73] D. H. Reneker and A. L. Yarin. Electrospinning jets and polymer nanofibers. *Polymer*, 49(10):2387 – 2425, 2008.

[74] S. Ramakrishna. *An Introduction to Electrospinning and Nanofibers*. World Scientific Pub Co Inc, 2007.

[75] D. H. Reneker and I. Chun. Nanometre diameter fibres of polymer, produced by electrospinning. *Nanotechnology*, 7(3):216, 1996.

[76] T. Jarusuwannapoom, W. Hongrojjanawiwat, S. Jitjaicham, L. Wannatong, M. Nithitanakul, C. Pattamaprom, P. Koombhongse, R. Rangkupan, and P. Supaphol. Effect of solvents on electro-spinnability of polystyrene solutions and morphological appearance of resulting electrospun polystyrene fibers. *European Polymer Journal*, 41(3):409 – 421, 2005.

[77] J.S. Lee, K. H. Choi, H. D. Ghim, S. S. Kim, D. H. Chun, H. Y. Kim, and W. S. Lyoo. Role of molecular weight of atactic poly(vinyl alcohol) (pva) in the structure and properties of pva nanofabric prepared by electrospinning. *Journal of Applied Polymer Science*, 93(4):1638–1646, 2004.

[78] S. Zhao, X. Wu, L. Wang, and Y. Huang. Electrospinning of ethyl–cyanoethyl cellulose/tetrahydrofuran solutions. *Journal of Applied Polymer Science*, 91(1):242–246, 2004.

[79] T. Wang and S. Kumar. Electrospinning of polyacrylonitrile nanofibers.

Journal of Applied Polymer Science, 102(2):1023–1029, 2006.
[80] S. Cavaliere, S. Subianto, I. Savych, D. J. Jones, and J. Roziere. Electrospinning: designed architectures for energy conversion and storage devices. *Energy Environ. Sci.*, 4:4761–4785, 2011.
[81] H. Zhu, X. Wang, F. Yang, and X. Yang. Promising carbons for supercapacitors derived from fungi. *Advanced Materials*, 23(24): 2745–2748, 2011.
[82] E. Raymundo-Piñero, F. Leroux, and F. Béguin. A high-performance carbon for supercapacitors obtained by carbonization of a seaweed biopolymer. *Advanced Materials*, 18(14):1877–1882, 2006.
[83] L. Wei, M. Sevilla, A. B. Fuertes, R. Mokaya, and G. Yushin. Hydrothermal carbonization of abundant renewable natural organic chemicals for high-performance supercapacitor electrodes. *Advanced Energy Materials*, 1(3):356–361, 2011.
[84] SWANCA. Bio-plastic from lignin, Retrieved: November 6th 2016. URL http: //swanca.ca/main/index.php/what-we-do/item/10-bio-plastic-from-lignin.
[85] The International Lignin Institute. About lignin, Retrieved: July 25th 2016. URL http://www.ili-lignin.com/aboutlignin.php.
[86] H. Mainka, O. Täger, E. Körner, L. Hilfert, S. Busse, F.T. Edelmann, and A. S. Herrmann. Lignin: an alternative precursor for sustainable and cost-effective automotive carbon fiber. *Journal of Materials Research and Technology*, 4(3):283 – 296, 2015.
[87] LignoWorks. What is lignin?, Retrieved: July 17th 2016. URL http://www.icfar.ca/lignoworks/content/what-lignin.html.
[88] G. Milczarek and O. Inganäs. Renewable cathode materials from biopolymer/conjugated polymer interpenetrating networks. *Science*, 335 (6075):1468–1471, 2012.
[89] S. Chatterjee, T. Saito, and A. Rios, O.and Johs. *Lignin Based Carbon Materials for Energy Storage Applications*. ACS Publications, 2014.
[90] H. Mainka, L. Hilfert, S. Busse, F. Edelmann, E. Haak, and A.S. Herrmann. Characterization of the major reactions during conversion of lignin to carbon fiber. *Journal of Materials Research and Technology*, 4(4):377 – 391, 2015.
[91] E. B. Jones S. Chatterjee, A. C. Clingenpeel, A. M. McKenna, O. Rios, N. W. McNutt, D. J. Keffer, and A. Johs. Conversion of lignin precursors to carbon fibers with nanoscale graphitic domains. *ACS Sustainable Chemistry & Engineering*, 2(8):2002–2010, 2014.
[92] I. Dallmeyer, L.T. Lin, Y. Li, F. Ko, and J. F. Kadla. Preparation and characterization of interconnected, kraft lignin-based carbon fibrous

materials by electrospinning. *Macromolecular Materials and Engineering*, 299(5):540–551, 2014.

[93] L. Lin, Yi. Li, and F. Ko. Fabrication and properties of lignin based carbon nanofiber. *Journal of Fiber Bioengineering and Informatics*, 6(4):335–347, 2013.

[94] M.i Kijima, T. Hirukawa, F. Hanawa, and T. Hata. Thermal conversion of alkaline lignin and its structured derivatives to porous carbonized materials. *Bioresource Technology*, 102(10):6279 – 6285, 2011.

[95] K. Babel and K. Jurewicz. Koh activated lignin based nanostructured carbon exhibiting high hydrogen electrosorption. *Carbon*, 46(14):1948 – 1956, 2008.

[96] L. Zhang, A. Aboagye, A. Kelkar, C. Lai, and H. Fong. A review: carbon nanofibers from electrospun polyacrylonitrile and their applications. *Journal of Materials Science*, 49(2):463–480, 2014.

[97] M. Wu, Q. Wang, K. Li, Y. Wu, and H. Liu. Optimization of stabilization conditions for electrospun polyacrylonitrile nanofibers. *Polymer Degradation and Stability*, 97(8):1511 – 1519, 2012.

[98] J.C. Chen and I.R. Harrison. Modification of polyacrylonitrile (pan) carbon fiber precursor via post-spinning plasticization and stretching in dimethyl formamide (dmf). *Carbon*, 40(1):25 – 45, 2002. ISSN 0008-6223. doi:http://dx.doi.org/10.1016/S0008-6223(01)00050-1. URL http://www.sciencedirect.com/science/article/pii/S0008622301000501.

[99] G. Fagerlund. Determination of specific surface by the bet method. *Matériaux et Construction*, 6(3):239–245, 1973.

[100] H. P. Klug and L. E. Alexander. *X-ray diffraction procedures*, volume 2. Wiley New York, 1954.

[101] A. Goudarzi, L. Lin, and F. K. Ko. X-ray diffraction analysis of kraft lignins and lignin-derived carbon nanofibers. *Journal of Nanotechnology in Engineering and Medicine*, 5(2):021006–021006, 09 2014.

[102] C. Lai, Z. Zhou, L. Zhang, X. Wang, Q. Zhou, Y. Zhao, Y. Wang, X. Wu, Z. Zhu, and H. Fong. Free-standing and mechanically flexible mats consisting of electrospun carbon nanofibers made from a natural product of alkali lignin as binder-free electrodes for high-performance supercapacitors. *Journal of Power Sources*, 247:134 – 141, 2014.

[103] Y. Wang, S. Serrano, and J. J. Santiago-Aviles. Conductivity measurement of electrospun pan-based carbon nanofiber. *Journal of Materials Science Letters*, 21(13):1055–1057, 2002.

[104] C. Huang, C. Hsu, P. Kuo, C. Hsieh, and H. Teng. Mesoporous carbon spheres grafted with carbon nanofibers for high-rate electric double layer capacitors. *Carbon*, 49(3):895 – 903, 2011.

[105] J. Schwan, S. Ulrich, V. Batori, H. Ehrhardt, and S. R. P. Silva. Raman spectroscopy on amorphous carbon films. *Journal of Applied Physics*, 80 (1):440–447, 1996.

[106] Meryl D. Stoller and Rodney S. Ruoff. Best practice methods for determining an electrode material's performance for ultracapacitors. *Energy Environ. Sci.*, 3:1294–1301, 2010.

[107] W. Xing, C. C. Huang, S. P. Zhuo, X. Yuan, G. Q. Wang, D. Hulicova-Jurcakova, Z. F. Yan, and G. Q. Lu. Hierarchical porous carbons with high performance for supercapacitor electrodes. *Carbon*, 47 (7):1715–1722, 6 2009.

[108] C. Kim and K.S. Yang. Electrochemical properties of carbon nanofiber web as an electrode for supercapacitor prepared by electrospinning. *Applied physics letters*, 83(6):1216–1218, 2003.

[109] Y. Zhai, Y. Dou, D. Zhao, P. F. Fulvio, R. T. Mayes, and S. Dai. Carbon materials for chemical capacitive energy storage. *Advanced Materials*, 23 (42):4828–4850, 2011.

[110] S. Zhu, M. Chen, J. Sun, J. Liu, T. Wu, H. Su, S. Qu, Y. Xie, S. Wang, X. Su, and G. Diao. Novel highly conductive ferroferric oxide/porous carbon nanofiber composites prepared by electrospinning as anode materials for high performance li-ion batteries. *RSC Adv.*, 6:58529–58540, 2016.

[111] M. Ago, K. Okajima, J. E. Jakes, S. Park, and O. J. Rojas. Lignin-based electrospun nanofibers reinforced with cellulose nanocrystals. *Biomacromolecules*, 13(3):918–926, 2012.

[112] Y. Li. *Structures, properties and applications of multifunctional lignin nanofibres*. PhD thesis, University of British Columbia, 2015.

[113] J. Dallmeyer. *Preparation and characterization of lignin nanofibre-based materials obtained by electrostatic spinning*. PhD thesis, University of British Columbia, 2013.

[114] R. Ruiz-Rosas. The production of submicron diameter carbon fibers by the electrospinning of lignin. *Carbon (New York)*, 48(3):696–705, 03.

[115] L. L. Zhang and X. S. Zhao. Carbon-based materials as supercapacitor electrodes. *Chem. Soc. Rev.*, 38:2520–2531, 2009.

[116] X. Ji, K. T. Lee, and L. F. Nazar. A highly ordered nanostructured carbon-sulphur cathode for lithium-sulphur batteries. *Nat Mater*, 8(6): 500–506, 06 2009.

[117] C. Liang, N. J. Dudney, and J. Y. Howe. Hierarchically structured sulfur/carbon nanocomposite material for high-energy lithium battery. *Chemistry of Materials*, 21(19):4724–4730, 10 2009.

[118] M. Teng, J. Qiao, F. Li, and P. K. Bera. Electrospun mesoporous carbon

nanofibers produced from phenolic resin and their use in the adsorption of large dye molecules. *Carbon*, 50(8):2877–2886, 7 2012.

[119] Z. Liu, D. Fu, F. Liu, G. Han, C. Liu, Y. Chang, Y. Xiao, M. Li, and S. Li. Mesoporous carbon nanofibers with large cage-like pores activated by tin dioxide and their use in supercapacitor and catalyst support. *Carbon*, 70: 295–307, 4 2014.

[120] H. Hou, L. Wang, F. Gao, G. Wei, B. Tang, W. Yang, and T. Wu. General strategy for fabricating thoroughly mesoporous nanofibers. *Journal of the American Chemical Society*, 136(48):16716–16719, 12 2014.

[121] D. Saha, Y. Li, Z. Bi, J. Chen, J. K. Keum, D. K. Hensley, H. A. Grappe, H. M. Meyer, S. Dai, M. P. Paranthaman, and A. K. Naskar. Studies on supercapacitor electrode material from activated lignin-derived mesoporous carbon. *Langmuir*, 30(3):900–910, 2014.

[122] Q. Wang, J. Yan, and Z. Fan. Carbon materials for high volumetric performance supercapacitors: design, progress, challenges and opportunities. *Energy Environ. Sci.*, 9:729–762, 2016.

[123] F.S. Baker. Low cost carbon fiber from renewable resources. Technical report, Oak Ridge National Laboratory, 2010.

[124] T. Wang. *Electrospun Carbon Nanofibers for Electrochemical Capacitor Electrodes*. PhD thesis, Georgia Institute of Technology, May 2007.

Appendix A

Additional Cyclic Voltammograms

A.1 Cyclic Voltammograms of ECNFs(99/1) at Various Scan Rates.

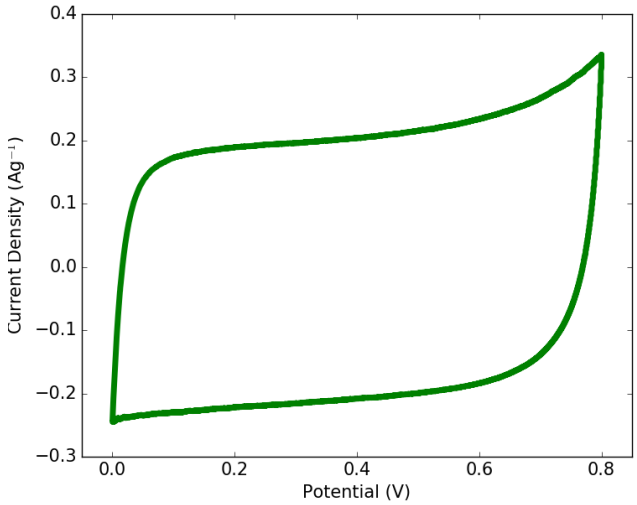

Figure A.1: CV trace of ECNFs(99/1) at a scan rate of 5 mV s^{-1}.

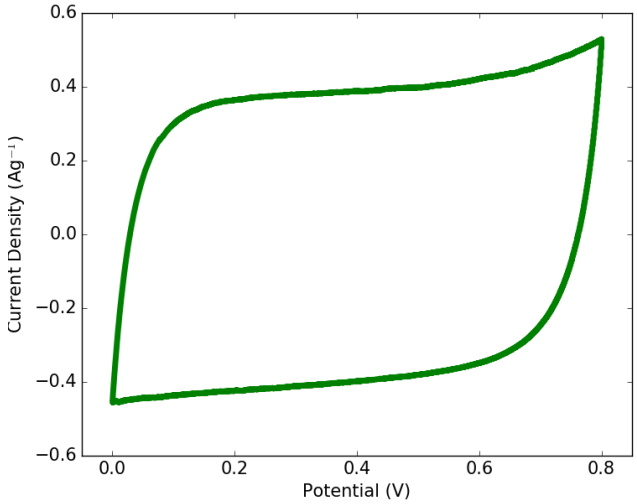

Figure A.2: CV trace of ECNFs(99/1) at a scan rate of 10 mV s^{-1}.

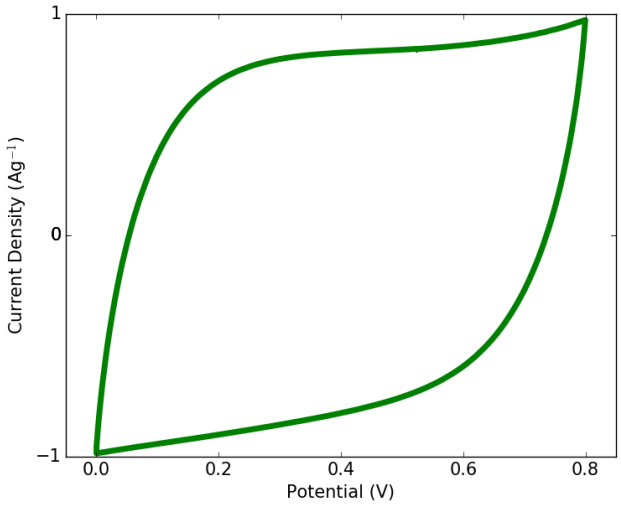

Figure A.3: CV trace of ECNFs(99/1) at a scan rate of 30 mV s^{-1}.

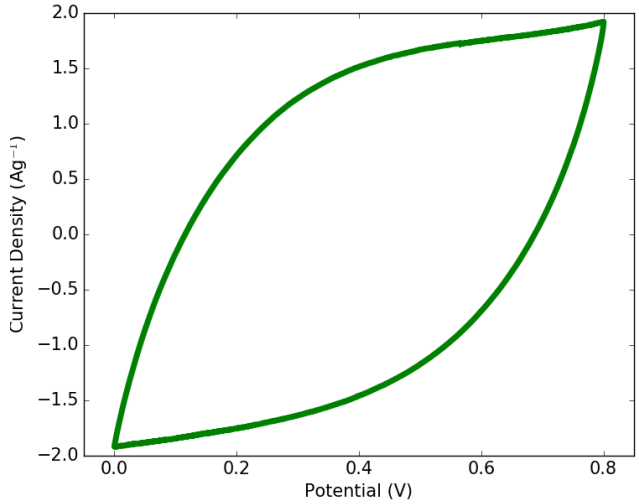

Figure A.4: CV trace of ECNFs(99/1) at a scan rate of 50 mV s^{-1}.

A.2 Cyclic Voltammograms of P-ECNFs(99/1) at Various Scan Rates.

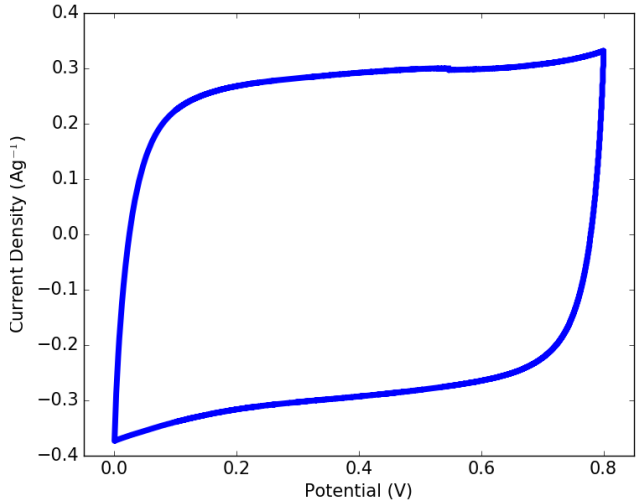

Figure A.5: CV trace of P-ECNFs(99/1) at a scan rate of 5 mV s^{-1}.

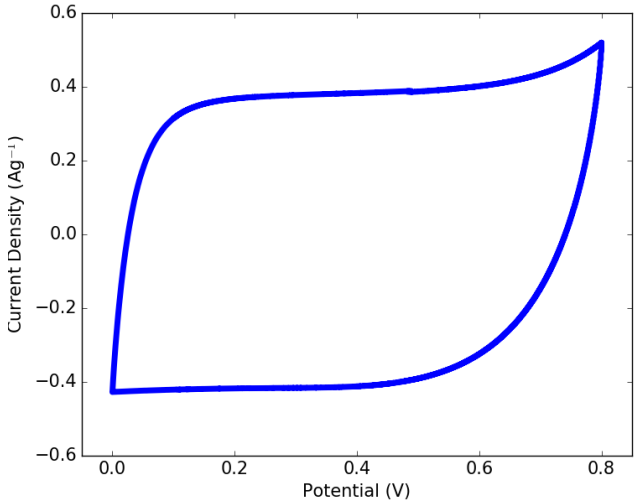

Figure A.6: CV trace of P-ECNFs(99/1) at a scan rate of 10 mV s^{-1}.

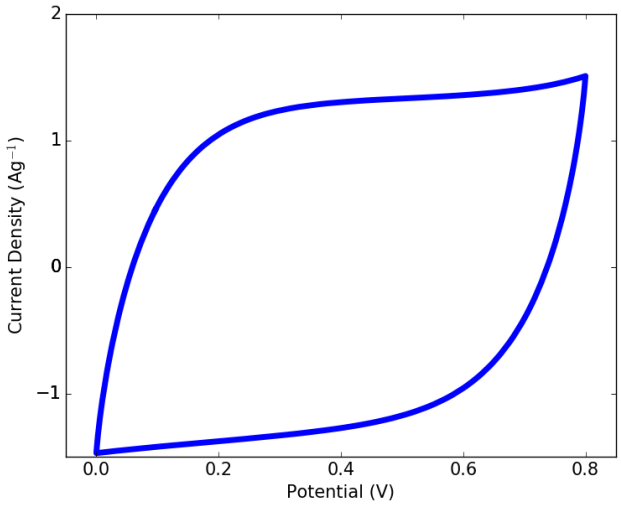

Figure A.7: CV trace of P-ECNFs(99/1) at a scan rate of 30 mV s^{-1}.

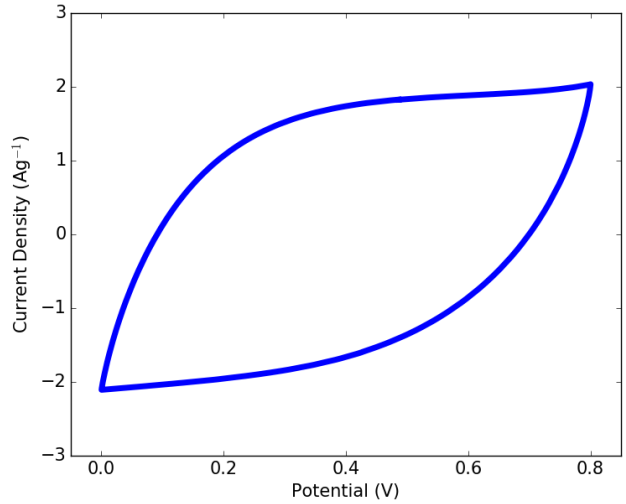

Figure A.8: CV trace of P-ECNFs(99/1) at a scan rate of 50 mV s^{-1}.

A.3 Cyclic Voltammograms of P-ECNFs(98/2) at Various Scan Rates.

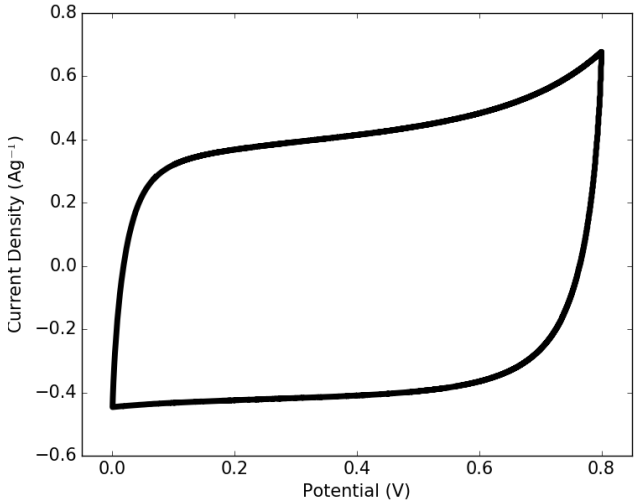

Figure A.9: CV trace of P-ECNFs(98/2) at a scan rate of 5 mV s^{-1}.

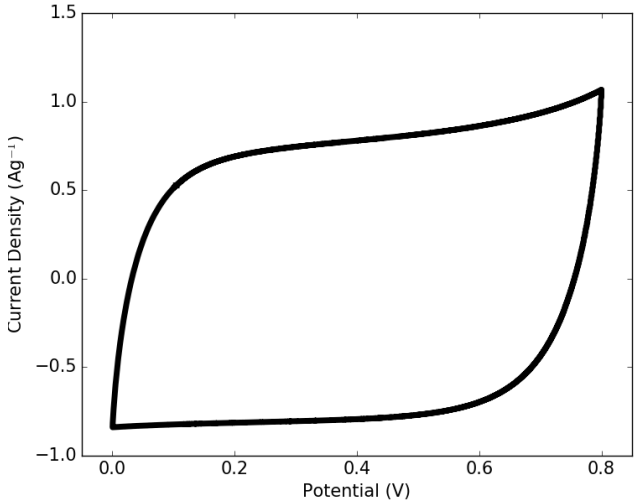

Figure A.10: CV trace of P-ECNFs(98/2) at a scan rate of $10\,\mathrm{mV\,s^{-1}}$.

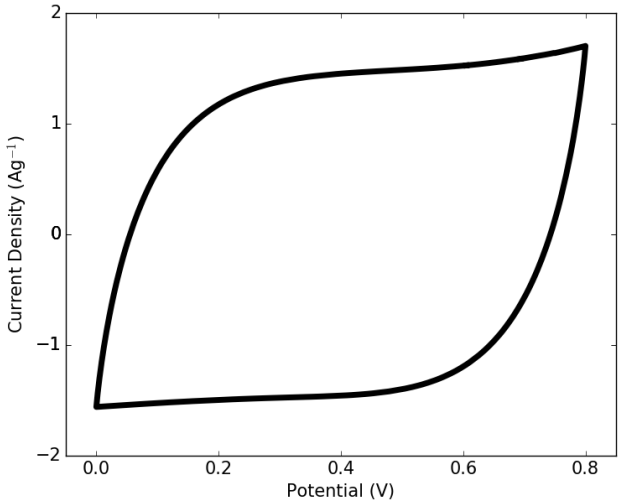

Figure A.11: CV trace of P-ECNFs(98/2) at a scan rate of $30\,\mathrm{mV\,s^{-1}}$.

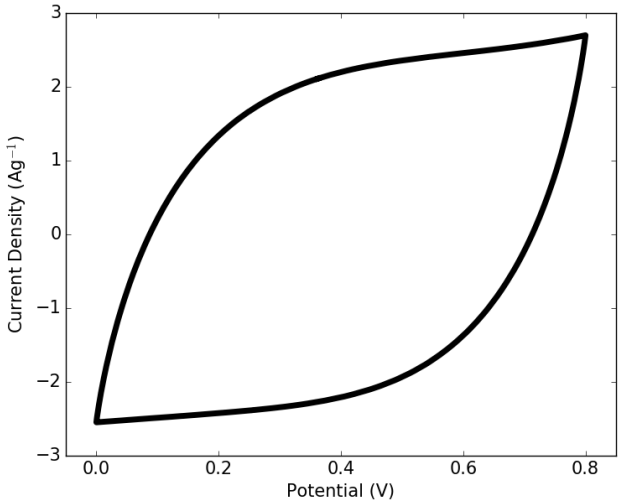

Figure A.12: CV trace of P-ECNFs(98/2) at a scan rate of 50 mV s^{-1}.

A.4 Cyclic Voltammograms of P-ECNFs(97/3) at Various Scan Rates.

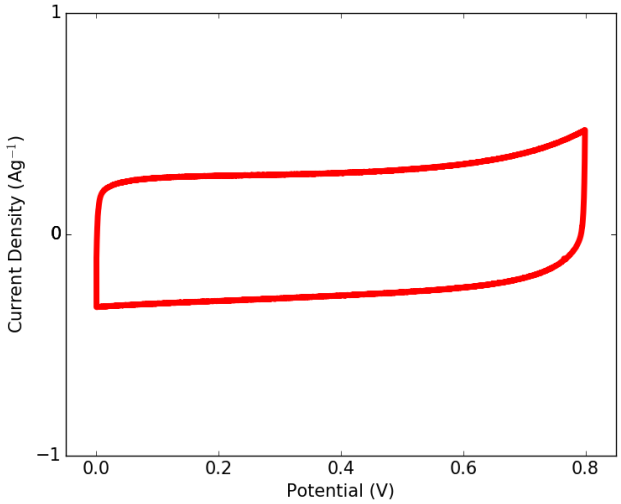

Figure A.13: CV trace of P-ECNFs(97/3) at a scan rate of 5 mV s^{-1}.

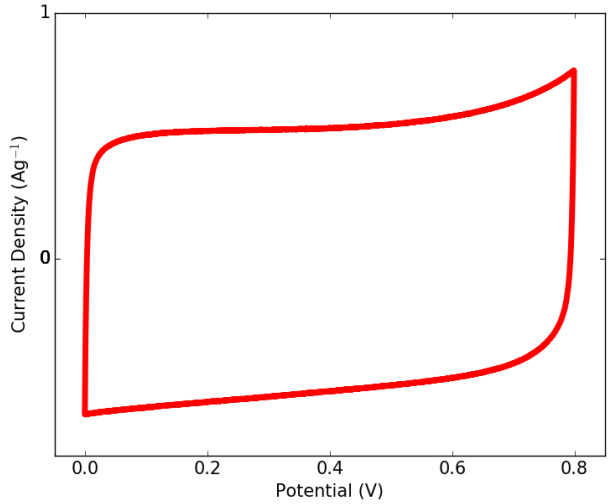

Figure A.14: CV trace of P-ECNFs(97/3) at a scan rate of 10 mV s^{-1}.

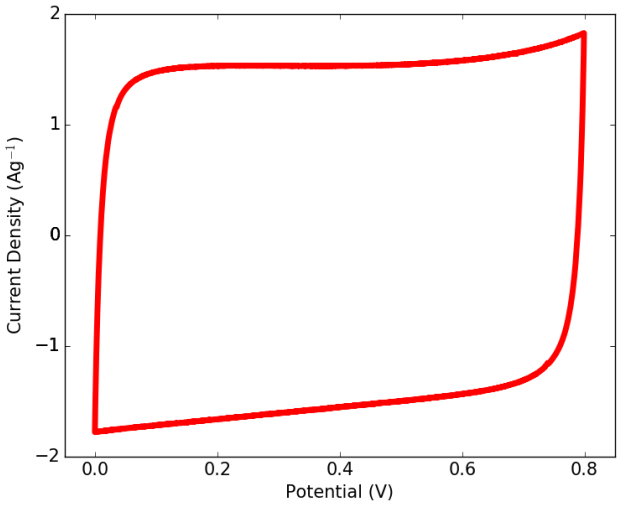

Figure A.15: CV trace of P-ECNFs(97/3) at a scan rate of 30 mV s^{-1}.

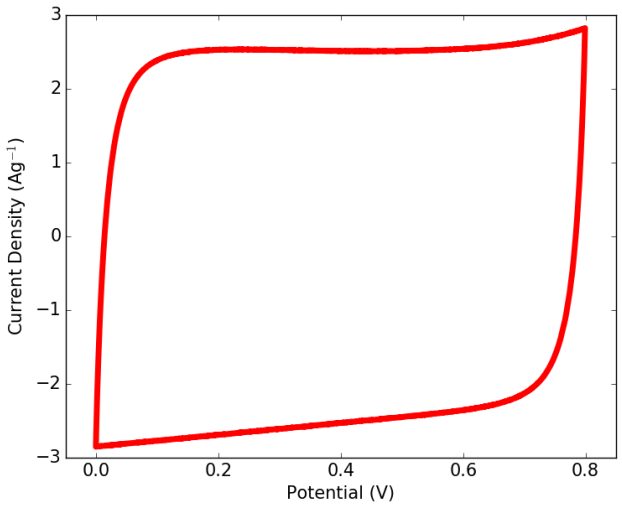

Figure A.16: CV trace of P-ECNFs(97/3) at a scan rate of 50 mV s^{-1}.

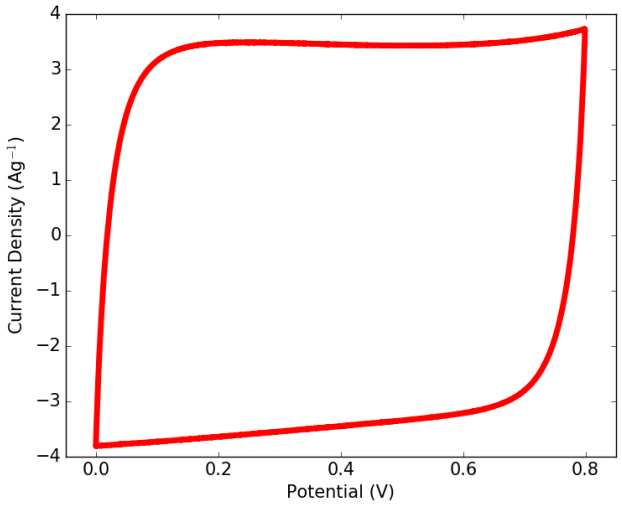

Figure A.17: CV trace of P-ECNFs(97/3) at a scan rate of 70 mV s^{-1}.

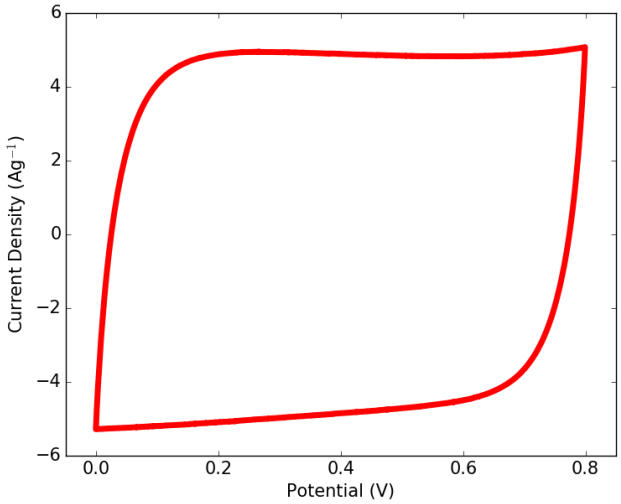

Figure A.18: CV trace of P-ECNFs(97/3) at a scan rate of 100 mV s^{-1}.

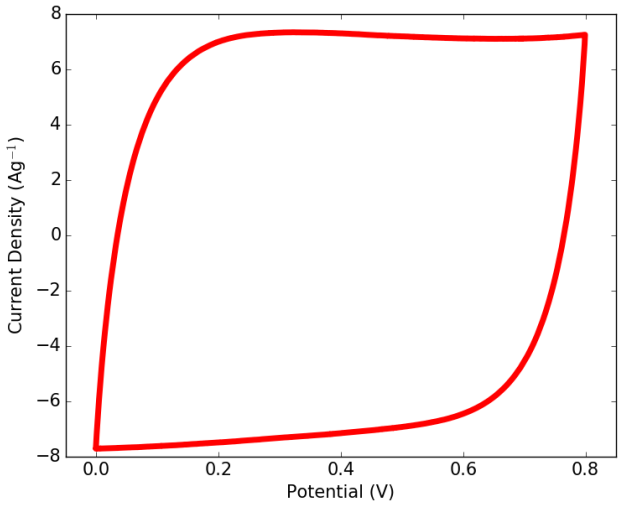

Figure A.19: CV trace of P-ECNFs(97/3) at a scan rate of 150 mV s^{-1}.

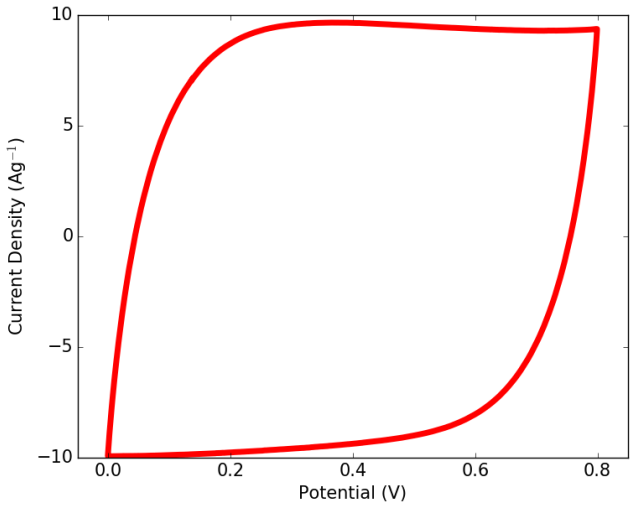

Figure A.20: CV trace of P-ECNFs(97/3) at a scan rate of 200 mV s^{-1}.

Appendix B

Additional Galvanostatic Charge/Discharge Traces

B.1 Galvanostatic Charge/Discharge Traces for ECNFs(99/1) at Various Current Densities.

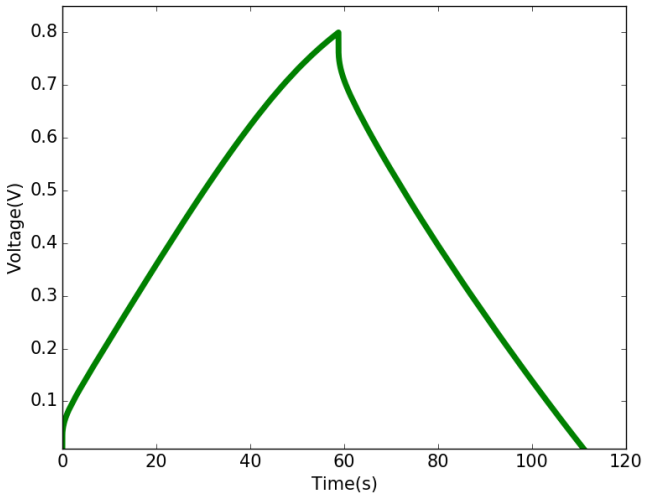

Figure B.1: Galvanostatic charge/discharge trace for ECNFs(99/1) at a current density of 400 mA g^{-1}.

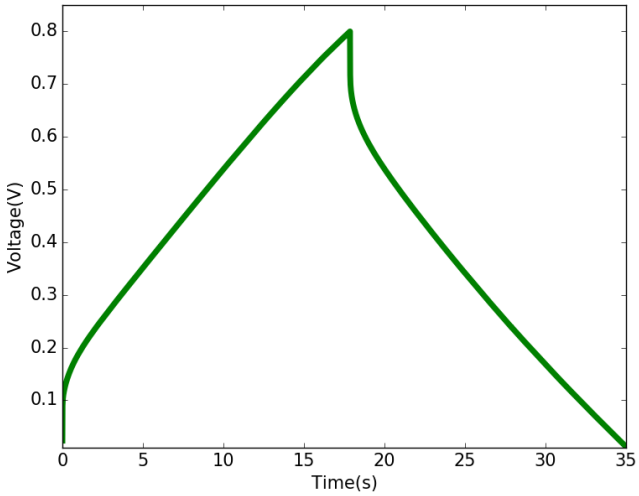

Figure B.2: Galvanostatic charge/discharge trace for ECNFs(99/1) at a current density of 1000 mA g^{-1}.

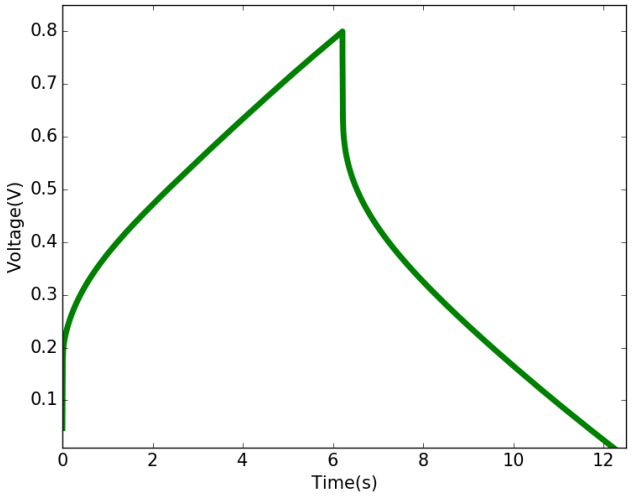

Figure B.3: Galvanostatic charge/discharge trace for ECNFs(99/1) at a current density of 2000 mA g^{-1}.

B.2 Galvanostatic Charge/Discharge Traces for P-ECNFs(99/1) at Various Current Densities.

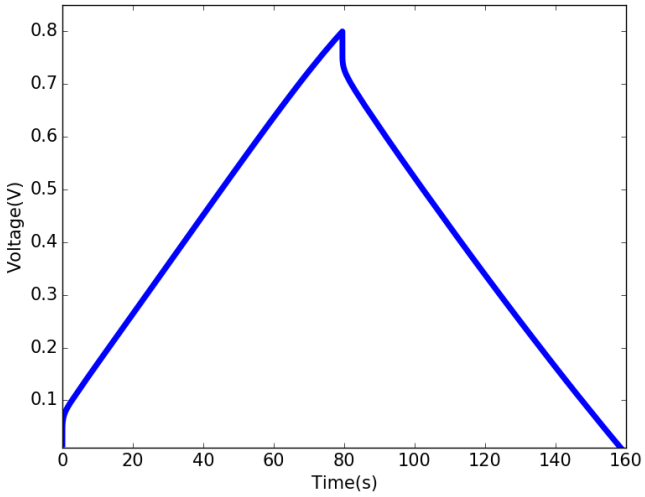

Figure B.4: Galvanostatic charge/discharge trace for P-ECNFs(99/1) at a current density of 400 mA g^{-1}.

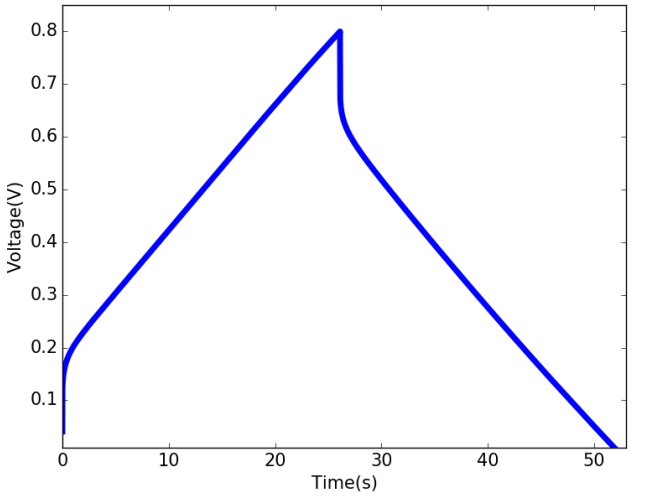

Figure B.5: Galvanostatic charge/discharge trace for P-ECNFs(99/1) at a current density of 1000 mA g^{-1}.

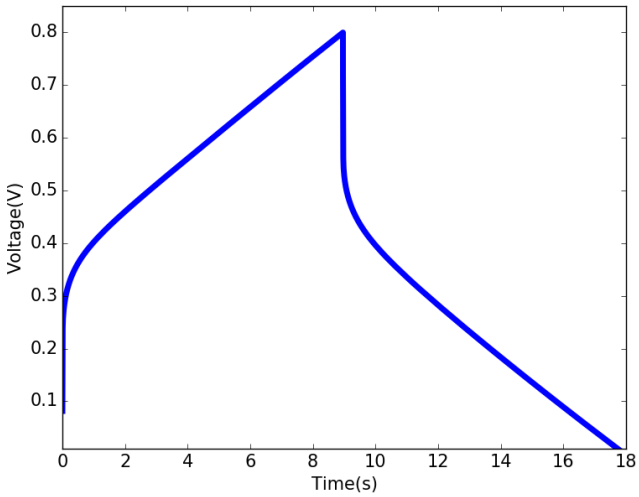

Figure B.6: Galvanostatic charge/discharge trace for P-ECNFs(99/1) at a current density of 2000 mA g^{-1}.

B.3 Galvanostatic Charge/Discharge Traces for P-ECNFs(98/2) at Various Current Densities.

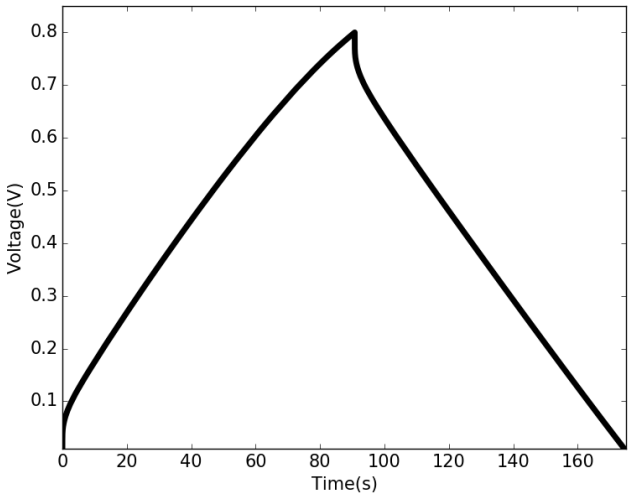

Figure B.7: Galvanostatic charge/discharge trace for P-ECNFs(98/2) at a current density of 400 mA g^{-1}.

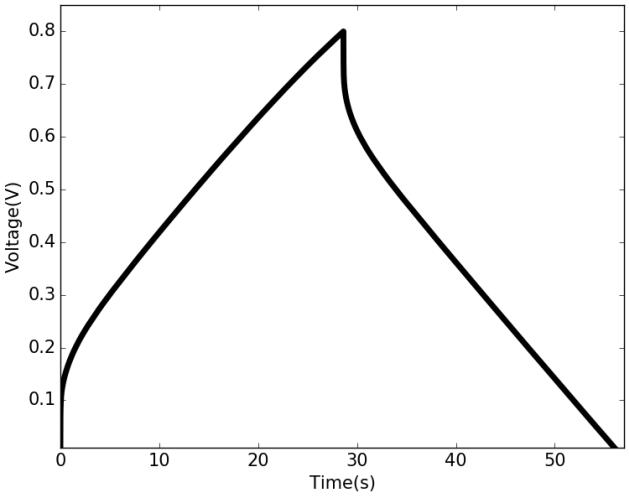

Figure B.8: Galvanostatic charge/discharge trace for P-ECNFs(98/2) at a current density of 1000 mA g^{-1}.

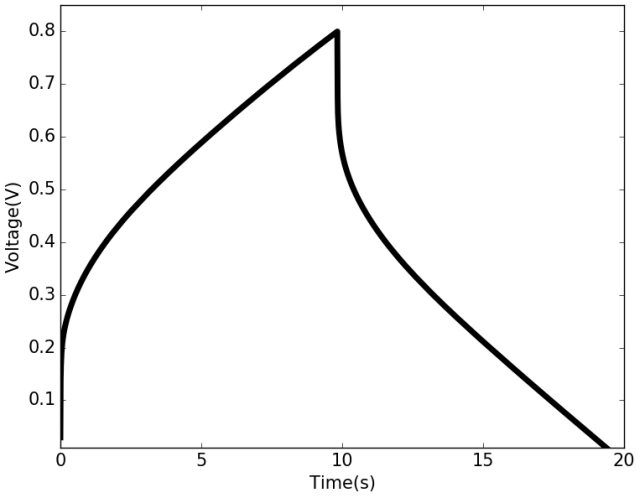

Figure B.9: Galvanostatic charge/discharge trace for P-ECNFs(98/2) at a current density of 2000 mA g^{-1}.

Appendix C

Additional SEM Images

C.1 SEM Images of P-ECNFs(99/1).

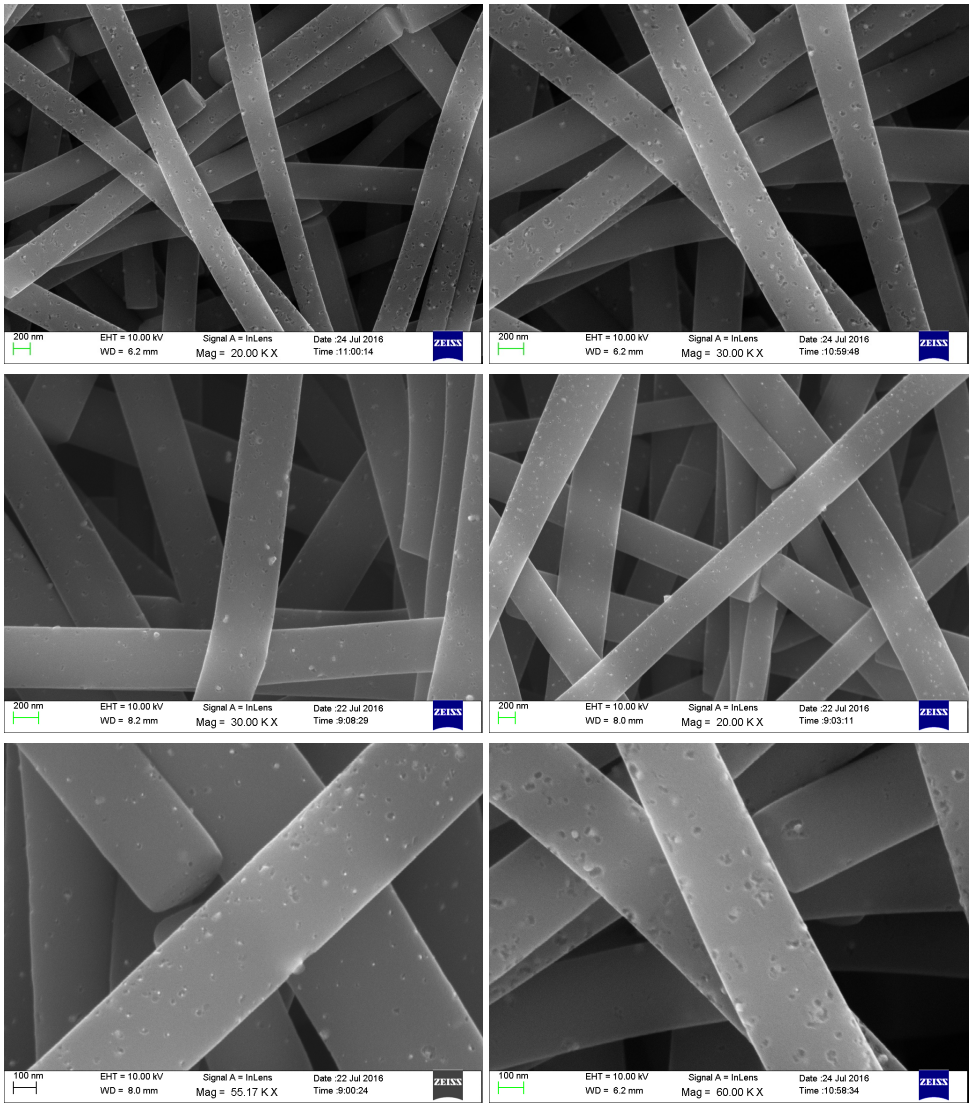

Figure C.1: SEM images of P-ECNFs(99/1) at various magnifications.

C.2 SEM Images of P-ECNFs(98/2).

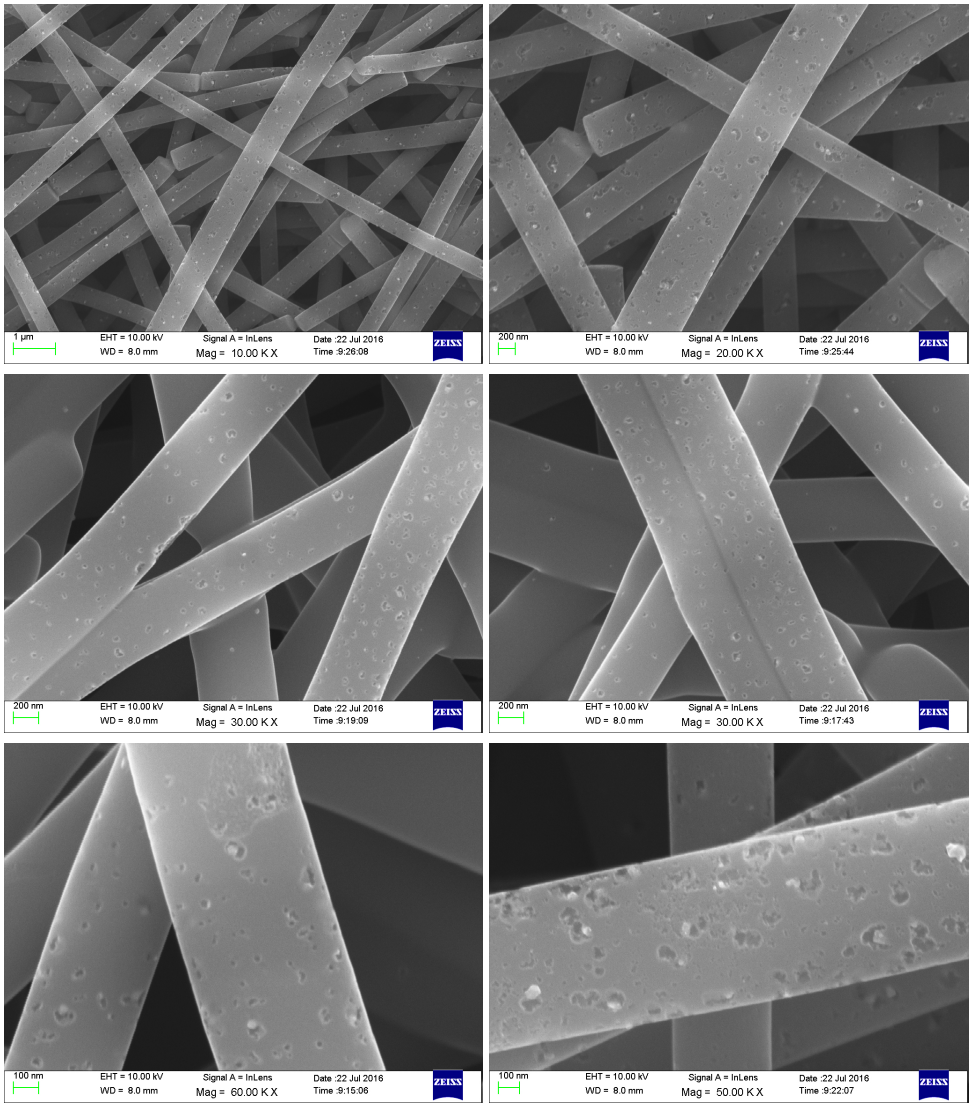

Figure C.2: SEM images of P-ECNFs(98/2) at various magnifications.

C.3 SEM Images of P-ECNFs(97/3).

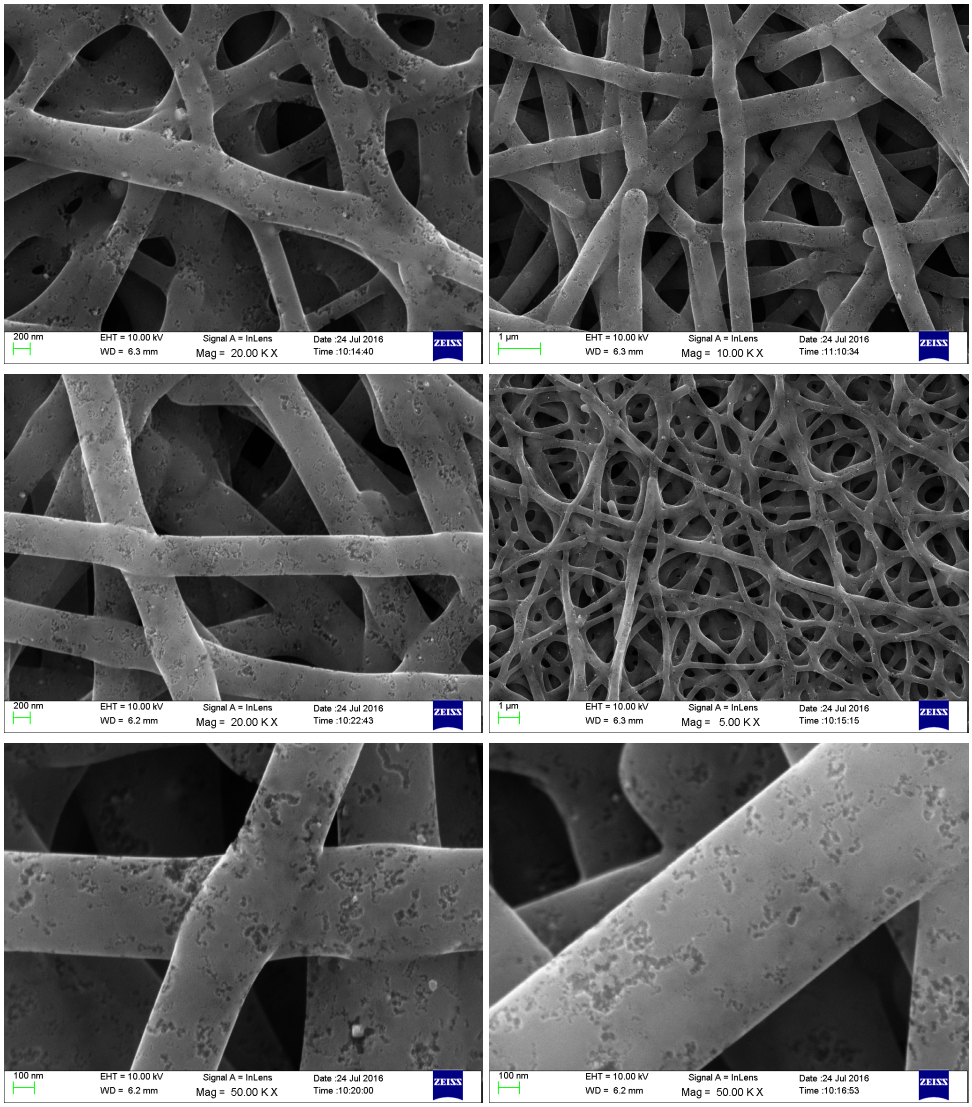

Figure C.3: SEM images of P-ECNFs(97/3) at various magnifications.